Construction and initialization of a temperature dependent magnetorelaxometry measurement system for the quantitative detection of magnetic nanoparticles in biological samples

vorgelegt von
Dipl.-Ing. Christian Knopke
aus Meerane

von der Fakultät V - Verkehrs- und Maschinensysteme
der Technischen Universität Berlin
zur Erlangung des akademischen Grades

Doktor der Ingenieurwissenschaften
- Dr.-Ing. -

genehmigte Dissertation

Promotionsausschuss:

Vorsitzender: Prof. Dr. phil. Dietrich Manzey
Gutachter: Prof. Dr.-Ing. Marc Kraft
Gutachter: Jun.-Prof. Dr.-Ing. Daniel Baumgarten

Tag der wissenschaftlichen Aussprache: 21. Dezember 2016

Berlin, 2017
D 83

Eidesstattliche Erklärung

Der Autor versichert, dass er über die urheberrechtlichen Nutzungsrechte an allen Teilen des Werkes verfügt und Rechte Dritter, insbesondere Urheber- und Persönlichkeitsrechte Dritter, mit der Veröffentlichung nicht verletzt werden.

Hiermit versichert der Autor, dass der Autor die vorliegende Arbeit selbstständig verfasst und keine anderen als die angegebenen Quellen und Hilfsmittel benutzt wurden. Alle Ausführungen, die anderen veröffentlichten oder nicht veröffentlichten Schriften wörtlich oder sinngemäß entnommen wurden, wurden kenntlich gemacht.

Die Arbeit hat in gleicher oder ähnlicher Fassung noch keiner anderen Prüfungsbehörde vorgelegen.

Ort, Datum Unterschrift

Abstract

The unique physical properties of magnetic nanoparticles (MNPs) have attracted increasing interest from researchers around the world. In particular, biomedical applications of MNPs are currently a growing research topic in medical science. However, all biomedical applications of MNPs crucially depend on reliable quantification methods that determine the concentration of MNPs in biological tissues. While well-established photometric iron quantification methods exist, they generally do not differentiate between iron originating from MNPs and other natural iron deposits in the body. In contrast, magnetorelaxometry (MRX), an analysis method based on the detection of the specific magnetic signals originating from MNPs, is capable of determining the particle content in biological tissues. However, MRX quantification is limited to MNPs with a magnetic core diameter of approximately 15 nm to 25 nm. The relaxation times for MNPs with smaller core diameters are too short to be determined at room temperature.

In the course of this thesis, MRX measurements were performed at various temperatures well below room temperature to investigate MNPs with core diameters <15 nm. This analysis of the relaxation amplitude as a function of temperature is referred to as *temperature dependent magnetorelaxometry* (TMRX). In addition to quantification of MNPs, TMRX analyses can be performed to investigate changes in the relaxation signal of the particles, which can be caused by *in vivo* concentration effects, dipole–dipole interactions between the particles, and interactions of the MNPs with the surrounding media.

This thesis was aimed to establish TMRX as an *in vitro* quantification method for MNPs in biological tissue samples. To do so, an existing measurement device (MPMS-XL, Quantum Design) was employed to perform TMRX analyses. With this device, the influence of the core size and size distribution of particles on their TMRX signals was investigated, and a quantification method for particles with diameters <15 nm was developed. In addition, TMRX analyses were performed to investigate dipole–dipole interactions between the particles. However, TMRX analyses with this device were very time consuming and a single relaxation measurement took up to 40 min, which in turn limited the sampling rate of the measured TMRX spectra. Therefore, only particularly long relaxations could be detected in this so-called *long time regime* of the Magnetic Property Measurement System (MPMS).

To perform TMRX analyses in the *short time regime* of only a few seconds, a custom instrument was designed. For this purpose, an existing, magnetically shielded MRX system was extended using a helium flow cryostat as a temperature-controlled sample holder and magnetizing unit. The highly sensitive magnetic sensors of this system required only non-magnetic and non-metallic materials for its construction. In addition, a magnetizing coil had to be designed and characterized for magnetizing the tissue samples. Therefore, the construction and initialization of this temperature controlled sample holder with a magnetizing unit was one of the key aspects of this thesis.

To conclude, the *in vitro* quantification of MNPs in biological tissues was established using TMRX analyses in the long and short time regime. In addition, dipole–dipole interaction was investigated using TMRX analyses, which led to the development of a novel empirical model describing the interaction energy in MNP samples. Therefore, the performed analyses exhibited the strong potential of TMRX as an investigation method to quantify and characterize MNP in biological tissues.

Zusammenfassung

Die einzigartigen physikalischen Eigenschaften magnetischer Nanopartikel (MNP) haben in den vergangenen Jahren das Interesse von Wissenschaftlern aus aller Welt geweckt. Insbesondere die biomedizinischen Anwendungsmöglichkeiten der MNP sind aktuell ein wachsendes Forschungsfeld. Allerdings hängen die biomedizinischen Anwendungen der MNP entscheidend von verlässlichen Quantifizierungsmethoden ab, welche die MNP-Konzentration in biologischen Geweben bestimmen können. Die etablierten photometrischen Eisenquantifizierungsmethoden können nicht zwischen Eisen, welches von Nanopartikeln stammt, und körpereigenem Eisen unterscheiden. Im Gegensatz zu diesen Methoden kann die Magnetrelaxometrie (MRX) die Menge an MNP in biologischen Geweben bestimmen, basierend auf dem spezifischen magnetischen Signal der MNP. Dennoch ist die MRX-Quantifizierung nur für MNP mit Kerndurchmesssern von 15 nm bis 25 nm möglich, da die Relaxationszeiten kleinerer MNP zu kurz sind, um bei Raumtemperatur detektiert zu werden.
Im Zuge dieser Arbeit wurden MRX-Messungen bei verschiedenen Temperaturen unterhalb der Raumtemperatur durchgeführt, um MNP mit Kerndurchmessern von <15 nm zu untersuchen. Diese Untersuchung der Relaxationsamplitude als Funktion der Temperatur wird auch als temperaturabhängige Magnetrelaxometrie (TMRX) bezeichnet. Zusätzlich zur Quantifizierung der MNP kann die TMRX auch genutzt werden, um Änderungen im Relaxationssignal der Partikel zu untersuchen. Diese Änderungen können dabei von *in vivo* Konzentrationseffekten, der Dipol–Dipol-Wechselwirkung zwischen den MNP und von Wechselwirkungen der MNP mit dem umgebenden Medien stammen.
Das Ziel dieser Arbeit war es, TMRX als *in vitro* Qantifizierungsmethode für MNP in biologischen Gewebeproben zu etablieren. Um dieses Ziel zu erreichen, wurde zunächst ein existierendes Messgerät (MPMS-XL, Quantum Design) für TMRX-Messungen verwendet. Mit diesem Messgerät konnte der Einfluss der Kerngröße und Größenverteilung der Nanopartikel auf das TMRX Signal untersucht, sowie eine Quantifizierungsmethode für MNP <15 nm entwickelt werden. Zusätzlich wurde das TMRX-Messverfahren genutzt, um die Dipol–Dipol-Wechselwirkung zwischen Partikeln zu untersuchen. Die TMRX-Messungen mit diesem Messgerät sind sehr zeitaufwendig, da schon eine einzelne Relaxationsmessung bis zu 40 min braucht. Die lange Messzeit senkt zusätzlich die Auflösung der TMRX-Spektren. Mit dem Magnetic Property Measurement System (MPMS) können daher nur besonders lange Relaxationen gemessen werden im sogenannten langen Zeitregime.
Um TMRX Messungen im kurzen Zeitregime mit einer Messzeit von wenigen Sekunden durchzuführen, wurde daher ein eigenes Messinstrument konstruiert. Zu diesem Zweck wurde ein bereits vorhandenes, magnetisch-geschirmtes MRX-System mit Hilfe eines Helium-Durchfluss-Kryostanten um einen temperierbaren Probenhalter und eine Magnetisierungseinheit erweitert. Die hoch-sensiblen magnetischen Sensoren des Systems erlaubten dabei nur unmagnetische und nichtmetalische Werkstoffe als Konstruktionsmaterial. Zusätzlich wurde eine Magnetisierungsspule für die Charakterisierung und Magnetisierung der Gewebeproben entworfen. Die Konstruktion und Inbetriebnahme des temperierbaren Probenhalters mit Magnetisierungseinheit stellt daher ein Schwerpunkt dieser Dissertation dar.
Zusammenfassend lässt sich sagen, dass die *in vitro* Quantifizierung von MNP in biologischem Gewebe mittels TMRX im kurzen und langen Zeitregime erfolgreich etabliert wurde. Zusätzlich wurde die Dipol–Dipol-Wechselwirkung mit Hilfe der TMRX untersucht und ein neues empirisches Model zur Beschreibung der Wechselwirkungsenergie in MNP-Proben entwickelt. Die durchgeführten Untersuchungen zeigen daher das starke Potential der TMRX als Untersuchungsmethode zur Quantifizierung und Charakterisierung von MNP in biologischem Gewebe.

Danksagung

Diese Arbeit ist im Rahmen meiner wissenschaftlichen Tätigkeit an der Physikalisch–Technischen Bundesanstalt (PTB) in Kooperation mit der SocraTec R&D GmbH entstanden. Ich bedanke mich daher bei Arbeitsgruppenleiter Lutz Trahms dafür, dass er diese Gelegenheit an der PTB ermöglicht hat und bei dem gesamten Team von SocraTec, dass sich für mich eingesetzten hat. Mein höchster Dank gilt Frank Wiekhorst für seine konsequente Unterstützung, Geduld und wissenschaftliche Betreuung während der gesamten Promotionsphase.

Für die Unterstützung beim Entwerfen und Konstruieren des Kryostaten möchte ich mich bei Dirk Gutkelch und Götz Klaukin bedanken und die hervorragende Arbeit der gesamten Institutswerkstatt der PTB loben. Bei Jens Voigt, Rainer Körber und Allard Schnabel möchte ich mich dafür bedanken, dass sie mir mit ihrem einmaligen Erfahrungschatz über die Inbetriebnahme von Helium-Kryostaten besonders in den kritischen Phasen der Doktorarbeit mit Rat und Tat beistanden.

Ohne die professionelle Unterstützung von Maik Liebl und Nora Höfner beim Betreiben der MRX-Messtechnik wäre die Arbeit in dieser Form nicht möglich gewesen. Für ihre Hilfe möchte ich mich besonders bedanken. Für ihre selbstlose Hilfsbereitschaft bedanke ich mich bei Patricia Radon. Das erfolgreiche Betreiben der Sensortechnik ist ihrer professionellen Unterstützung zu verdanken. Bei Dietmar Eberbeck möchte ich mich für die vielen Gespräche über die Wechselwirkung der Nanopartikel bedanken, die entscheidend zur Entwicklung des neun Wechselwirkungsmodells beigetragen haben. Ebenso bedanke ich mich bei Norbert Löwa und Uwe Steinhoff für ihre Anregungen und ihre Unterstützung bei meinem wissenschaftlichen Werdegang. Natürlich möchte ich mich auch bei Olaf Kosch bedanken, welcher mich 2007 im Rahmen meiner studentischen Tätigkeit mit der PTB und SocraTec in Kontakt brachte und mir die Welt der Wissenschaft eröffnete.

Besonderen Dank auch an den gesamten Fachbereich 8.2 für die stets freundschaftliche Arbeitsatmosphäre und stete Hilfsbereitschaft, die wesentlich zum Gelingen dieser Arbeit beigetragen haben.

Contents

I Background

1 Introduction 23

1.1 Magnetic Nanoparticles in Medical Science 24

1.2 Aim of the Thesis 25

1.3 Way of Proceeding 25

1.4 Clinical Applications of Magnetic Nanoparticles 27

1.4.1 Drug Targeting 27

1.4.2 Hyperthermia 28

2 Theoretical Background 31

2.1 Magnetism in Nanoparticles 32

2.1.1 Superparamagnetic Single-Domain Particles 32

2.1.2 Néel and Brownian Relaxation of Magnetic Nanoparticles 33

2.1.3 Particle Distribution 35

2.1.4 Dipole–Dipole Interactions 36

3 Measuring Principles 39

3.1 Magnetorelaxometry (MRX) 40

3.1.1 Basic Principles 40

3.1.2 Magnetorelaxometry Measurement Setup 41

3.2 Temperature Dependent Magnetorelaxometry (TMRX) 43

3.2.1 Basic Principles 43

3.2.2 Creation of the TMRX Spectrum 44

3.2.3 Influence of the Particle Core Size on the TMRX Spectrum 44

3.2.4 Influence of the Particle Core Size Distribution on the TMRX Spectrum 45

3.2.5 TMRX using a Magnetic Property Measurement System 45

3.2.6 TMRX using the 6-Channel SQUID System 47

II Results

4 TMRX Analyses in the Long Time Regime 51

4.1 Data Analysis for the Magnetic Property Measurement System 52

4.1.1 Uncertainty of the Measurement Results 52

4.1.2 Fitting the Exponential Decay of the Measured Relaxation Signal 54

4.1.3 Analysis of the Switch-Off Time of the Superconducting Magnet 55

4.1.4 Communication with a Magnetic Property Measurement System 56

4.2 Influence of Magnetic Nanoparticle Amount on the TMRX Spectrum 58

4.2.1 Analysis of a Magnetic Nanoparticle Dilution Series 59

4.2.2 Quantification of the Iron Content via *Peak Comparison* 60

4.2.3 Analysis of Magnetic Nanoparticles in Cell Samples 62

4.3 Influence of the Magnetizing Field Strength on the TMRX Spectrum 65

4.3.1 Magnetizing Field Strength dependent Changes in the Relaxation Signal 66

4.4 Influence of Particle Aggregation on the TMRX Spectrum 68

4.4.1 Influence of Dipole–Dipole Interactions on the TMRX Spectrum 69

4.4.2 Quantification of Aggregated and Unaggregated Particles 70

4.5 Multicore Particle Analysis via TMRX of Underlying Fractions 72

4.5.1 TMRX Analysis of Multicore and Precursor Particles 73

4.5.2 TMRX Analysis of Separated Particles 74

5 Numerical Simulation of TMRX Spectra 77

5.1 Influence of Dipole–Dipole Interactions on the TMRX Spectrum 78

5.2 Simulation of TMRX Spectra of Non–Interacting Particles 80

5.3 Simulation of TMRX Spectra Including Dipole–Dipole Interactions 84

6 Development of a TMRX System for the Short Time Regime 89

6.1 Custom TMRX Measurement System 90

6.1.1 Description of the Temperature Controlled Sample Holder 90

6.1.2 Description of the 6-Channel TMRX Measurement Setup 93

6.2 Characterization of the GRP Cryostat with Magnetizing Coil 94

6.2.1 Characterization of the Magnetizing Coil 94

6.2.2 Magnetic Characterization of the System 96

6.2.3 Determination of the Sample Position 98

6.2.4 Temperature Calibration at the Sample Position within the Cryostat 100

6.3 Quantification of Magnetic Nanoparticles using TMRX in the Short Time Regime 103

6.3.1 TMRX Analysis of the Resovist Dilution Series 104

6.3.2 Magnetic Nanoparticle Quantification Using the 6-Channel SQUID System 107

6.4 Quantification of Magnetic Nanoparticles in Biological Tissues using TMRX in the Short Time Regime 109

7 Conclusion 113

7.1 Summary and Conclusion 114

III Appendices

8 Magnetic Property Measurement System (MPMS) 119
8.1 Description of the Magnetic Property Measurement System 120

9 Construction 125
9.1 6-Channel SQUID System for TMRX 126
9.2 6-Channel SQUID System: Additional Graphics and Pictures 127
9.3 Technical Drawings of the GRP Cryostat 129
9.3.1 MPMS measurements from Chapter 6.4 134
9.3.2 Measurement and Fit Data from Chapter 5.3 135

List of Figures

1.1 Illustration of a magnetic nanoparticle with a **a** Superparamagnetic core, **b** Dextran coating, **c** Polyethylene glycol (PEG) layer, and **d** Antibody. 24

1.2 Picture of the TMRX measurement setup. The GRP Cryostat, which was designed and constructed in the course of this thesis, is inserted into the 6-channel SQUID system. The cryostat is cooled by liquid helium via the controllable helium transfer tube. The read out of the temperature sensor and control of the helium flow is established via the temperature control system. 26

1.3 **a)** Application of magnetic nanoparticles in a tumor supplying artery. The particles are magnetically guided into the malign tissue using an external high gradient DC magnet. **b)** Once the particles have reached the tumor, an external AC coil exposes the particles to an alternating magnetic field. Because of physical loss processes, the particles heat the surrounding tissue. 29

2.1 Illustration of the magnetic moments in a single domain MNP solution. Each particle consists only of one magnetic domain, which can be described through its magnetic moment and orientation. (A) Without an external magnetic field, the magnetic moments randomly orient into an equilibrium state. (B) With an external magnetic field, the single particles change their orientation in the direction of the external field. 32

2.2 Magnetization patterns of **a** ferromagnetic and **b** superparamagnetic materials. 33

2.3 Influence of the particle distance (D) on the Néel relaxation time (τ). With decreasing distance, the MNP relaxation time increases exponentially. The relaxation time of a $20\,\mathrm{nm}$ particle at $290\,\mathrm{K}$ is displayed. 37

3.1 Procedure for MRX analyses: Prior to the magnetizing phase, the particles are randomly oriented and no net magnetic moment is detectable. When the external magnetic field is applied, the magnetic moments of the particles align in the direction of the field when it is applied, and then after a short delay time following switch-off of the field, the relaxation is measured. During this measurement phase, the single magnetic moments of the MNP sample realign into a random equilibrium. The magnetic moments colored in red are aligned in the direction of the external magnetic field while the opposing moments are colored in blue. 40

3.2 Typical MRX setup: The magnetization coil creates a homogeneous magnetic field in the sample space during the magnetization phase (blue arrows). After switching off the coil, the SQUID detects the decaying net magnetic moment of the MNP sample. The magnetic field of the sample is illustrated in red. The superconducting, low–temperature SQUID sensors require liquid helium as coolant in order to operate inside the insulating Dewar vessel. 42

3.3 Measurement ranges for the MPMS and MRX 6-channel SQUID systems for particles of different sizes at $5\,\mathrm{K}$, $100\,\mathrm{K}$, and $300\,\mathrm{K}$. The Néel relaxation time (τ) was determined for monodisperse particles with an effective anisotropy of $1 \cdot 10^4\,\mathrm{J/m^3}$ that are not affected by dipole-dipole interaction (Equation 2.4) 43

3.4 Left: A typical TMRX plot where the amplitude change (ΔM) is displayed as a function of temperature. The maximum relaxation amplitude was observed at $30\,\mathrm{K}$, indicating that the investigated MNPs had a magnetic core size of $7\,\mathrm{nm}$ to $10\,\mathrm{nm}$. Right: Single relaxation curves at selected temperatures. The amplitude change is more or less pronounced depending on the temperature. 44

3.5 TMRX signals of two similar MNP samples differing only in their magnetic core diameters. Sample **A** (blue), with a core diameter of $6\,\mathrm{nm}$, had a maximum relaxation amplitude at $15\,\mathrm{K}$, whereas sample **B** (orange), with a core diameter of $7\,\mathrm{nm}$, exhibited its maximum relaxation amplitude at $25\,\mathrm{K}$. The different peak temperatures are indicated by the arrow. Because of the similar size distributions of the two particle samples, the shapes of the two curves resembled each other, even though the peak temperatures for the two particle systems were different. 46

4.1 In RSO mode the sample is periodically moved through a second order gradiometer. The SQUID response depends on the sample position within the gradiometer (Picture from Manual [1]). The samples magnetic moment and fit quality are determined through comparison of the SQUID response with a previously defined response curve of a reference sample. 52

4.2 Relative magnetic moments of different RSO measurements and their corresponding fit qualities. A lower fit quality resulted in a decreased accuracy for a given magnetic moment. A confidence interval of 95% was obtained. 53

4.3 Left: Exponential least squares fit (red line) of relaxation measurements, each consisting of 100 single RSO scans. The RSO measurements in the first five minutes experienced more variation because they only consisted of single RSO scans while the latter scans were repeated three times. Right: Residual of the fitted exponential function. The upper maximum deviation from the fit was approximately $\pm 3 \cdot 10^{-8}\,\mathrm{Am^2}$ 53

4.4 TMRX graph with error bars determined from the residuals of the fitted relaxation curves. The error bars are more or less pronounced depending on the signal strength at each temperature. The fit quality varied from a good average of 0.8 at room temperature to a low quality of 0.2 below $100\,\mathrm{K}$. 54

4.5 Switch–off and switch–on times of the MPMS superconducting magnet for set fields ranging from $0{,}1\,\mathrm{mT}$ to $5\,\mathrm{T}$. 55

4.6 Dilution series of the CD021110 magnetic nanoparticle solution in PCR tubes. 58

4.7 Relaxation curves for the CD021110 solution at different temperatures (10 of 17 curves are displayed). In the first 7 minutes, each data point was determined from a single RSO scan while the subsequent points obtained by averaging 3 RSO scans. 59

4.8 TMRX spectra of the different CD021110 dilution samples. The amplitude change (Δm) of each relaxation curve is displayed at the measured temperature. The maximum amplitude for each sample was observed at approximately $20\,\mathrm{K}$. The detection limit for this dilution series was determined with approximately $5 \cdot 10^{-8}\,\mathrm{Am}^2$. Due to the logarithmic display negative data points are not shown. At temperatures above $200\,\mathrm{K}$ no relaxation was observed within the measurement time window. 60

4.9 Total Iron Contents in the CD021110 dilution samples versus their relaxation amplitudes (Δm) at their peak temperatures. 61

4.10 Relaxation amplitude (Δm) as a function of temperature for CD021110 and Feraheme®. Even small differences in the particle characteristics resulted in noticeable changes in the relaxation amplitude curves. 62

4.11 MRX analysis of the control sample. No relaxation was observed. The background signal was $0{,}3\,\mu\mathrm{Am}^2$ for the first $7\,\mathrm{min}$ of detection and, then decreased to approximately $0{,}1\,\mu\mathrm{Am}^2$ because of the change in the number of averaged RSO measurements. 63

4.12 Temperature dependent magnetorelaxometry spectra for HeLa tumor cell lines and the initial CD021110-MNP solution as a reference. The TMRX spectra indicate that the MNP signals mainly differed in their relaxation signal strengths. The shapes of the curves remained the same for the incubated and non–incubated MNP samples. 63

4.13 TMRX signals for the Resovist precursor DDM 128 at different magnetization field strengths. The TMRX signal for DDM 128 exhibited two distinct peaks at $15\,\mathrm{K}$ and $150\,\mathrm{K}$ that were attributed to the bimodal distribution of the particle core size. Changes in the field strength had varying impacts on the particles of different sizes. The larger particles were less affected by higher field strengths because they were already saturated. 66

4.14 Left: Magnetization curves for small (blue line) and large (red line) superpara–magnetic particles. The larger MNPs exhibited a steeper slope than the smaller particles. Right: Magnetization and relaxation processes during an MRX procedure. The larger particles required a lower magnetization field strength to reach their saturation magnetization. Therefore, the larger particles were less magnetized than their smaller counterparts when exposed to the same magnetic field H_{mag}. This leading to a smaller amplitude change during the relaxation process. 67

4.15 Left: $30\mu\mathrm{L}$ of the original particle solution in distilled water. Right: Visible aggregation and sedimentation $30\,\mathrm{min}$ after addition of a sodium chloride solution ($c_{NaCl} = 1\,\mathrm{mol/L}$). 68

4.16 Changes in the TMRX signal through enforced aggregation. Both the stable and aggregated MNP samples exhibited relaxation signals at nearly every investigated temperature, with peak temperatures at $130\,\mathrm{K}$ and $210\,\mathrm{K}$, respectively. 69

4.17 TMRX signals of original (left) and aggregated (right) particles at different concentrations. The overall amplitude declined with increasing dilution. The peak temperatures at $130\,\mathrm{K}$ for the original and $210\,\mathrm{K}$ for the aggregated MNP samples remained unchanged for the different dilution steps. 70

4.18 Nominal total iron content versus relaxation amplitude at the maximum temperature for aggregated and unaggregated particles. While the samples had different peak temperatures, the ratio of the amplitude to the iron content was the same for both. 71

4.19 (Left) Transmission Electron Microscopy (TEM) image of the DMSA–coated precursor and (right) Gum Arabica multicore particles. (Picture from [67]) 72

4.20 TMRX Spectra of precursor and GA-coated MNPs. The precursor particles (gray squares) exhibited the largest relaxation amplitude at 60 K and a secondary shoulder at 120 K. The GA–covered multicore particles (red squares) only exhibited one maximum at 130 K. 73

4.21 The eluate (blue diamonds) exhibited a peak amplitude at 110 K whereas the discharge (orange circles) displayed a maximum at 70 K to 80 K. The amplitude strength per mg of iron for both fractions was slightly higher than that of the original precursor. 74

4.22 TMRX results for the aggregated precursor (stars) compared to the signals shown in Figure 4.20 and 4.21. The peak temperature for the aggregate was 175 K, and its amplitude per gram iron was only 30 % of that of the precursor. 75

5.1 TMRX spectra of the investigated MNP dilution series normalized to the iron content. The spectra were well described by a log-normal distribution of temperatures, from which the median temperature T_{med} was extracted. 79

5.2 Median temperature obtained from the log-normal fit of the TMRX spectra for the Endorem dilution series. The medium temperature was plotted as a function of the corresponding concentration. 79

5.3 Discretized core diameters (d_i) with corresponding probability densities (P_i) when $\tilde{d}$ =10 nm and $\sigma_d = 0,3$. In order to illustrate the discretization of $\bar{d}$, a particular large discretization step size was chosen. Highlighted respectively in green, red, and orange are the discrete values for the 8 nm, 8,5 nm, and 9 nm sized particles in the simulated distribution. In Figures 5.4 and Figure 5.5, their influence on the magnetization process and relaxation signal at a specific temperature are displayed. 80

5.4 Simulation of the magnetization process at 10 K based on the 10 nm particle distribution displayed in Figure 5.3. The time dependency of the magnetizing phase was calculated using Equation 5.6. The net magnetization of the sample was calculated by summing up the magnetizations of the discretized particle sizes according to their probability densities. In the MPMS magnetization process, the magnetization time (t_{mag}) was set to 480 s and the external field to 1 mT. Although the particle distribution exhibited a median at 10 nm, the particles that were active at 10 K were in the 8 nm (green) to 9 nm (orange) range. Most prominent was the influence of the 8,5 nm particles (red) on the magnetization curve. 81

5.5 Relaxation process for the 10 nm particle distribution shown in Figure 5.3 simulated using the discretized Néel formula (Equation 5.8). The relaxation signal is the summation of the individual decaying moments of the discretized particles. At 10 K, particle cores with a diameter of 8,5 nm(red) relaxed mainly in the first few minutes. Smaller particles (e.g., 8 nm, green, see Figure 5.4) relaxed in the microsecond range and are therefore not seen here. Only larger particles with diameters near 9 nm relaxed over the entire measurement time of 45 min. A dead time of 90 s, which is typical for MPMS analyses, is indicated with a red dashed line. The amplitude change (Δm) is the difference between the magnetic moment at the end of the dead time and the remaining magnetic moment at the end of the measurement phase. 82

5.6 Simulated TMRX spectra of four different simulated samples displayed as a function of temperature. The spectrum for a monodisperse sample consisting only of $10\,\mathrm{nm}$ particles is illustrated in blue while the spectrum for a simulated MNP sample with a core size distribution of $\tilde{d} = 10\,\mathrm{nm}$ and $\sigma = 0,3$ is presented in red. Distributions with $\sigma = 0,2$ (orange) and $\sigma = 0,1$ (brown) are also shown. 83

5.7 TMRX simulations of a log-normal distributed particle system with a mean diameter of $8\,\mathrm{nm}$ and a size distribution with $\sigma = 0,25$. Different interaction energy terms (Ed) for the approaches A, B, C, and D were implemented. With a decreasing inter–particle distance (D), the maximum temperatures and shapes of the TMRX spectra changed. The arrows indicate how the increasing interaction energy changes the value of T_{max} in the TMRX spectra. 85

5.8 TMRX results for dilution step C2 (red squares). Simulation of approaches A, C, and D for a log-normal distributed particle system with a mean diameter of $8\,\mathrm{nm}$ and a size distribution of $\sigma = 0,25$. The interaction energy for each approach caused a shift of T_{max} from $15\,\mathrm{K}$ to $28\,\mathrm{K}$. In approach A, the spectrum was shifted as a whole and not stretched like in approaches C and D. 86

5.9 Relationship between the experimentally determined nominal iron contents of the Endorem dilution series and the iron contents quantified using the approaches A, C, and D and the peak comparison method. 87

6.1 Experimental Setup: The data acquisition system (DAQ) reports the relaxation signal (**a**) obtained using the SQUID system and controls the magnetization coil (**b**). The temperature controller reports the data for the temperature sensor (**c**) in the glass reinforced plastic (GRP) cryostat and controls the needle valve (**d**) in the helium transfer tube. The measured temperature is then transmitted to the DAQ System (**a**). 90

6.2 One layer of (left) aluminum-coated fabric and (right) slit Mylar film. The aluminum-coated fabric is used as insulation in the Dewar. 91

6.3 Arrangement of the temperature diodes around the sample space. During MRX analyses, the permanently installed temperature diode can only measure the system temperature $4\,\mathrm{cm}$ from the sample. In order to calibrate the system, a second (calibration) sensor is installed in a sample dummy. 92

6.4 Transversal field at the center of the magnetizing coil at $356\,\mathrm{mA}$ for different longitudinal offsets. The longitudinal center of the $6{,}9\,\mathrm{cm}$ long coil is marked as zero on the X-axis. The direction toward the helium transfer tube is negatively notated. The curve reveals that the coil produces a small transversal field that is strongest at its longitudinal boundaries. The maxima are therefore at $-4{,}25\,\mathrm{cm}$ and $4{,}0\,\mathrm{cm}$. The transversal field strength at $356\,\mathrm{mA}$ ranges from $30\,\mu\mathrm{T}$ to $40\,\mu\mathrm{T}$ at these maxima. 94

6.5 Longitudinal field in the center of the magnetizing coil at $356\,\mathrm{mA}$ for different axial offsets. The center of the $6{,}9\,\mathrm{cm}$ long coil is marked as zero on the X-axis. The direction toward the helium transfer tube is negatively notated. The curve reveals a maximum plateau ranging from $-2\,\mathrm{cm}$ to $2\,\mathrm{cm}$ with a field strength of approximately $1\,\mathrm{mT}$. 95

6.6 Switch-off procedure for the magnetizing coil measured with a Digital Storage Oscilloscope (Agilent Technologies, DSO-X 2004A). After the switch-off impulse is initiated at $t = 0\,\mathrm{s}$, the voltage in the coil drastically decreases. After $20\,\mu\mathrm{s}$, the overshooting oscillation ceases as well. 96

6.7 MRX relaxation amplitude changes for the silica diode at different longitudinal positions in the 6-channel SQUID system are displayed for one SQUID sensor. The temperature sensor generates a dipole moment similar to that of an MNP sample because of its magnetic elements. The MRX analysis of the sensor was performed at different longitudinal positions from $-40\,\mathrm{mm}$ to $40\,\mathrm{mm}$ relative to the center of the magnetizing coil. A typical MRX sequence ($B_{mag} = 1\,\mathrm{mT}$, $t_{mag} = 1\,\mathrm{s}$, $t_{meas} = 1\,\mathrm{s}$) was performed at each position, and the sensor was operating during the MRX analysis. Therefore, the wires connected to the sensor conducted a $10\,\mu\mathrm{A}$ current. 98

6.8 Illustration of the sample position relative to magnetizing coil and SQUID. The sample is not positioned directly under the SQUID because the sensor can only detect transversal magnetic fields. Instead, it is placed with a longitudinal offset of approximately $4\,\mathrm{cm}$ in order to optimize the transversal magnetic field relative to the SQUID. The magnetizing coil and the permanent temperature sensor are placed directly beneath the SQUID. Through this arrangement, the sensor is less affected by the magnetic dipole fields because they are mainly longitudinal at the center position. 99

6.9 Arrangement of the temperature diodes around the sample space. The helium flow is illustrated in blue. The permanent sensor (red) can only measure the sample temperature indirectly. The calibration sensor (green) is installed in a sample dummy. During calibration measurements, both sensor signals are stored in a look-up table. 100

6.10 Typical temperature cool down sequence of the GRP cryostat for the calibration of the temperature at the sample position. The temperature of the diode which is four centimeter away from the sample space is displayed in black, while the sample temperature is displayed in red. In this sequence the system temperature falls from $290\,\mathrm{K}$ to $5\,\mathrm{K}$ in less than 20 minutes. During that time an offset between the sensor and the sample is visible. 101

6.11 (Left): Relaxation measurement at $275\,\mathrm{K}$ for the most concentrated Resovist samples obtained using MPMS. The relaxation process in the long time regime took $40\,\mathrm{min}$. (Right): Relaxation measurement performed using the GRP Cryostat in the 6-channel SQUID system. The measurement time in the short time regime only required $1\,\mathrm{s}$. In both plots, a relationship between the amplitude change and the MNP concentration was observed. However, the decay of the relaxation after switching off the external field was significantly more pronounced in the short time regime. 104

6.12 (Left) TMRX results for the Resovist dilution series performed using MPMS. (Right) TMRX results obtained using the GRP cryostat in the 6-channel SQUID system. The investigated temperature ranged from $5\,\mathrm{K}$ to room temperature for both systems. Both spectra were bimodal, with one peak at $25\,\mathrm{K}$ and a second peak at $200\,\mathrm{K}$ to $300\,\mathrm{K}$. Notably, while the second peak was between $200\,\mathrm{K}$ and $250\,\mathrm{K}$ in the spectrum obtained via MPMS (left), it appeared near room temperature in the spectrum obtained using the 6-channel SQUID system (right). 105

6.13 Peak temperatures for Resovist samples of different concentrations observed in the MPMS long time regime and 6-channel SQUID system short time regime. Each TMRX spectrum exhibited two distinct peak temperatures. The constant offset between the measured peak temperatures was attributed to the different time regimes. 106

6.14 Nominal iron content in the different Resovist samples versus the iron content determined using three different methods. The concentration of iron in the samples varied by several orders of magnitude. The axis in the figure are therefore displayed logarithmically. The methods included phenanthroline staining [78], quantification via MPS [51], and quantification via TMRX peak comparison. While all three methods were generally capable of determining the iron content, they differed in their overall accuracy. 107

6.15 TMRX spectra of five different mice liver samples and a freeze–dried reference sample. The measurements were performed using the 6-channel SQUID system with a GRP Cryostat. The amplitude changes at each temperature for temperatures ranging from 5 K to 290 K are displayed. All of the mice liver samples with administered MNPs exhibited temperature depending relaxation signals. The highly concentrated samples and the reference sample exhibited a signal peak at 150 K to 170 K. The liver from the control mouse (black line) was not exposed to nanoparticles and did not exhibit a significant TMRX signal. 110

6.16 Quantification results for an MPS analysis (orange) compared to those obtained via TMRX (blue) and MRX (gray) at room temperature. The peak comparison method described in chapter 4.2 was used for the TMRX analysis. The iron contents determined using MPS and TMRX matched, although their confidence intervals did not always overlap. The deviation is attributed to the different sample volumes (see Table 6.4). Quantification via MRX at room temperature overestimated the MNP amount. 111

8.1 Quantum Design Magnetic Property Measurement System (MPMS) 120

8.2 Above: A dilution series of freeze–dried nanoparticle solution in poly carbonate capsules. Below: A sample straw with an installed PC capsule. 121

8.3 Sample rod and Sample straw setup (Picture from Manual [1]) 121

8.4 Example of a typical MultiVu sequence: A measurement file was defined, different temperatures were set, and other sequences were called. 122

9.1 6-channel SQUID system: A magnetically shielded Dewar vessel containing six SQUID sensors. On the front of the cylindrical Dewar the 27 mm wide opening of the warm bore can be seen. In the course of the dissertation a helium flow cryostat was designed to fit in the warm bore and to cool a biological sample for TMRX analyses. 126

9.2 Illustration of the 6-channel SQUID system: The outer vacuum vessel surrounds the inner helium vessel. The warm bore is magnetically shielded by a niobium tube. The six SQUID sensors are operated with flux-locked-loop (FLL) electronics. 126

9.3 Experimental Setup: The data acquisition system (DAQ) reads out the relaxation signals (**a**) measured with the 6-channel SQUID system and controls the magnetizing coil(**b**). The temperature controller reads out the temperature sensor and controls the heating coil (**c**) in the glass reinforced plastics (GRP) Cryostat. In order to reach a certain temperature in the cryostat the temperature controller may open or close the needle valve(**d**) in the helium transfer tube. The measured temperature, the voltage of the heating coil, and the opening percentage of the needle valve are continuously transmitted to the DAQ System (**a**). 127

9.4 Oxford Instruments low loss transfer tube (LLT): The helium coolant is taken up over the Dewar leg, which fits into our helium transport vessels. The GRP Cryostat is attached at the tip of the flexible section. At the tip, the helium cryostat inlet cools the GRP Cryostat and retrieves the warm helium gas. The returning helium is released over an outlet at the knee of the transfer tube. The stepper motor off the automated needle valve and its corresponding serial interface also located at the knee. 127

9.5 Close-up picture of the sample holder with an installed sample during the cooling process. 128

9.6 The virtual interface (VI) for the Mercury ITC gives the user an easy method for sending commands and receiving data. The VI constantly measures the temperature of the permanent sensor with the option to save the data to an ASCII text file. The commands that can be sent to the ITC include manual opening of the helium needle valve to a defined percentage. In addition, an ASCII text file can be loaded in order to perform temperature sweeps. The VI allows to initiation of both cool–down and warm–up sweep procedures. 128

9.7 General assembly drawing of the cryostat 129

9.8 Rear end cover 129

9.9 Front end flange 130

9.10 Vacuum valve housing 130

9.11 Vacuum valve plug 131

9.12 Outer vaccum tube 131

9.13 Inner vaccum tube 132

9.14 Sample rod 132

9.15 Sample holding 133

9.16 TMRX analyses of MNP samples presented in Chapter 6.4. The analyses were performed in the long time regime of the MPMS at $B_{mag} = 1\,\mathrm{mT}$. The resulting TMRX spectra were not usable for quantification. 134

9.17 Relaxation data for the MNP samples (m82, $T = 290\,\mathrm{K}$) presented in Chapter 6.4. The analyses were performed in the long time regime of the MPMS at $B_{mag} = 1\,\mathrm{mT}$. Except for the reference sample, the signal to noise ratios in the relaxation curves were too low for interpretation. 134

List of Tables

4.1 Iron amount in CD021110 dilution series. 60

4.2 Iron amount in CD021110–exposed tumor cells. 64

9.1 Given parameters of the Endorem dilution series. 135

9.2 Fit parameters obtained by simulation without interaction energy. Iron amount estimated via peak comparison. 135

9.3 Fit parameters obtained by simulation with approach A. Iron amount estimated comparison of the amplitude factor. 135

9.4 Fit parameters obtained by simulation with approach C. Iron amount estimated comparison of the amplitude factor. 136

9.5 Fit parameters obtained by simulation with approach D. Iron amount estimated comparison of the amplitude factor. 136

I

Background

1 **Introduction** 23

1.1 Magnetic Nanoparticles in Medical Science

1.2 Aim of the Thesis

1.3 Way of Proceeding

1.4 Clinical Applications of Magnetic Nanoparticles

2 **Theoretical Background** 31

2.1 Magnetism in Nanoparticles

3 **Measuring Principles** 39

3.1 Magnetorelaxometry (MRX)

3.2 Temperature Dependent Magnetorelaxometry (TMRX)

1. Introduction

1.1 Magnetic Nanoparticles in Medical Science

The term *nanotechnology* is used to describe materials with structural features having at least one dimension in the nanometer range ($1 \cdot 10^{-9}$ m - $1 \cdot 10^{-7}$ m). The unique physical properties of these nanometer scale materials have attracted an increasing interest from researchers around the world. A very promising class of nanotechnology is known as nanoparticles, i.e., ultrafine particles, often stabilized in a liquid suspension. The use of nanoparticles in biomedical applications is currently a growing research topic in medicine: their small size and unique properties enable these particles to be used in a whole new range of applications. For instance, nanoparticles may cross the blood-brain barrier [45] or even overcome the placental barrier [93] while carrying a medically active ingredient. The characteristics of these particles are significantly determined by their core materials and coatings. In most cases, the coating consists of a polymer or monomer to which proteins can be attached for functionalization of the nanoparticle. The core consists of metallic (e.g., gold) or non-metallic (e.g., silicon) materials (Figure 1.1) and affects the toxicity, visualization capabilities, and magnetic behavior of the nanoparticle. The core material of magnetic nanoparticles often consists of magnetic elements such as iron, nickel or cobalt and their oxides.

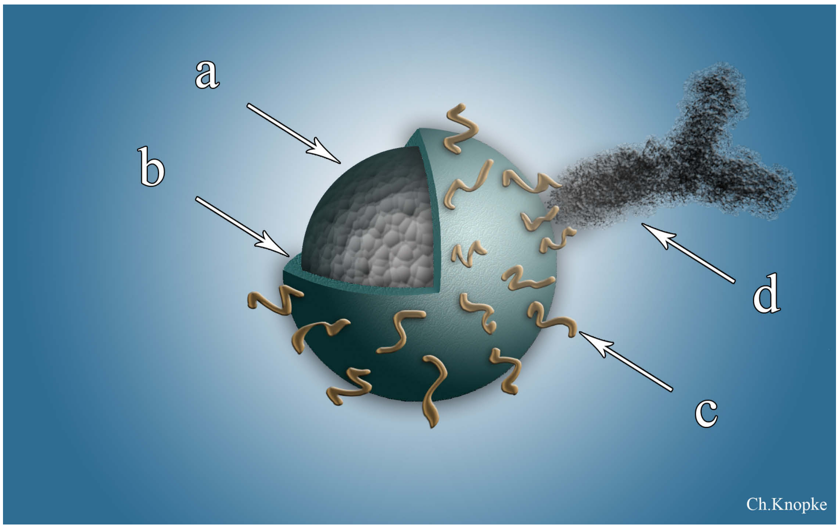

Figure 1.1: Illustration of a magnetic nanoparticle with a **a** Superparamagnetic core, **b** Dextran coating, **c** Polyethylene glycol (PEG) layer, and **d** Antibody.

Their magnetic properties make these particles particularly interesting for biomedical applications because they can be remotely moved, heated, and/or detected using an external magnetic field [68]. In the present study, only magnetic nanoparticles with iron oxide cores were investigated. A prominent biomedical application of magnetic nanoparticles (MNPs) is the treatment of cancer via the induction of heat into the malignant tissue, i.e., hyperthermia [40]. Other applications include the use of MNPs as contrast enhancement agents in existing imaging methods such as magnetic resonance imaging (MRI) [81] and magnetic particle imaging (MPI), a novel particle-based imaging method [28]. In magnetic drug targeting for cancer therapy, a chemotherapeutic substance is bound to the MNPs [100] and the particles are remotely delivered to the tumor region using an external magnetic gradient. Notably, the coating on the MNPs can be formulated with specific ligands that bind to cancer cells [79].

In all the applications mentioned above, the ability to quantify the amount of MNPs in the biological system is crucial. Achieving the appropriate concentration and distribution of the MNPs within the tissue is a decisive factor for the success of these biomedical applications. Well-established photometric techniques used for the quantification of the iron content in cells include Perls' Prussian blue staining method [70], phenanthroline staining [78], and atomic absorption spectroscopy (AAS). However, these methods generally do not differentiate between iron originating from MNPs and other natural iron deposits in the body.

In contrast magnetic measurements are capable of determining the iron oxide nanoparticle content in biological samples [96]. Superconducting quantum interference device (SQUID) magnetometry [92] and magnetic particle spectroscopy [51] are magnetic methods for *in vitro* quantification of the MNP contents in tissues. Magnetorelaxometry (MRX) has also been applied as quantification method [97]. In MRX, the magnetic *relaxation* of the MNPs is measured. This relaxation is a delayed magnetic response to an external magnetization impulse. Through the temporal separation of the magnetization impulse and the measurement process, only the MNP signal is detected because biological iron deposits do not contribute to the relaxation signal. In addition, the MRX analysis of MNPs can be conducted *in vitro* or *in vivo* [97]. Because the relaxation time depends on the sizes of the magnetic particle's core, the obtained signals can also be used to characterize the MNPs. Furthermore, if the rotation of the particles is blocked because of binding to biological tissue, alteration of the relaxation process occurs and can be detected [46]. However, when MNPs are applied *in vivo*, their signals may also change because of concentration effects, dipole–dipole interactions, and interactions with the surrounding media.

Notably, the particle size detectable using MRX ranges from 25 nm to approximately 15 nm [97]. The relaxation times for MNPs with smaller core diameters are too short to be detected at room temperature. One way to investigate MNPs with smaller magnetic cores is to slow down their relaxation processes by lowering the sample temperature. This analytical technique is referred to as *temperature dependent magnetorelaxometry* (TMRX) and can be performed *in vitro*. The display of the relaxation spectrum as function of temperature provides a detailed view of the magnetic behavior of the MNPs, their concentration, and how the relaxation is altered by the biological environment. TMRX analyses have been performed earlier mainly to investigate the distribution of energy barriers within MNPs [75].

1.2 Aim of the Thesis

The aim of this thesis is to establish TMRX as a quantification method for magnetic nanoparticles in biological tissue samples and for the detection of alterations in the magnetic behavior of MNPs within biological tissues.

In order to establish TMRX analyses several milestones need to be fulfilled in the course of this dissertation. These include the implementation of a consistent data analysis method, the development of the MNP quantification procedure and the measurement of exemplary MNP samples in order to investigate the signal alterations of MNPs in biological tissues. Another main emphasis of this work is the reduction of the TMRX measurement time. To accomplish this milestone the TMRX procedure of an existing measurement system will be revised. If necessary a custom TMRX measurement system should be build in order to reduce the measurement time to a minimum.

1.3 Way of Proceeding

In a first step, an existing measurement device (MPMS-XL, Quantum Design) was employed to perform TMRX analyses, which is described in Chapter 4. With the MPMS, the influence of the core size and size distribution of particles on their TMRX signals was investigated, and a quantification method for particles with diameters <15 nm developed (Section 4.2). In addition, alterations of the TMRX spectra because of changes in the MNP concentration were investigated (Section 4.4). The MPMS is attractive because it provides precise control of the sample temperature and has a convenient measurement procedure. However, TMRX analyses with this device are very time consuming; a single relaxation measurement takes up to 40 min. This long measurement time also limits the sampling rate of the TMRX spectra measured with the MPMS. In the course of this study, therefore, an alternative magnetization procedure was implemented using the MPMS and investigated to determine if faster TMRX analyses were feasible (Section 4.1.4).

Furthermore, a numerical simulation of the TMRX process is introduced in Chapter 5. The simulation results were used to describe the influence of the core diameters and size distributions of particles on their TMRX spectra (Section 5.2). Moreover, an interaction energy term was introduced to describe alterations of the MNP signal because of dipole–dipole interactions (Section 5.3). The numerical simulation results were then used to develop phenomenological models to assist the quantification of MNPs via TMRX.

A custom instrument with a reduced overall TMRX measurement time and switch-off time was also developed, as can be seen in Chapter 6. For this purpose, an existing magnetically shielded SQUID system (see Section 9.1 in the Appendix) capable of MRX was extended using a helium flow cryostat as a temperature-controlled sample holder and magnetizing unit. In order to perform fast relaxation measurements, the switch-off process of the magnetizing unit was also optimized. Along with to the manufacturing, which was performed by the Institute's workshop, the temperature control software for the cryostat was programmed and a reliable cool down procedure was developed. The final measurement setup with the glass reinforced plastic cryostat (GRP cryostat) is displayed in Figure 1.2.

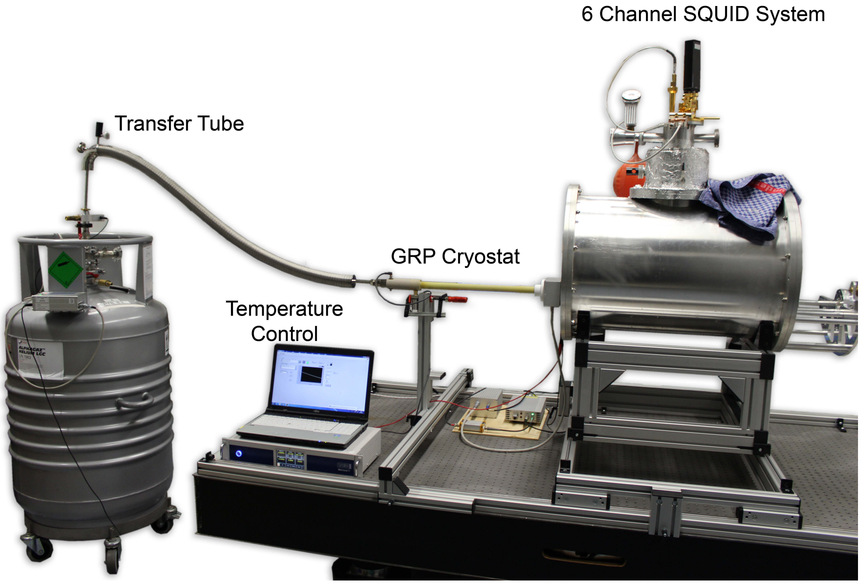

Figure 1.2: Picture of the TMRX measurement setup. The GRP Cryostat, which was designed and constructed in the course of this thesis, is inserted into the 6-channel SQUID system. The cryostat is cooled by liquid helium via the controllable helium transfer tube. The read out of the temperature sensor and control of the helium flow is established via the temperature control system.

TMRX analyses with this new 6-channel system are faster with a higher sampling rate than those performed with the MPMS. Through the optimized switch-off process of the coil and its non-magnetic design, the new measurement system is capable of performing MRX analyses within seconds. Therefore, the TMRX spectra obtained with the new system belong to a different, faster time regime than the spectra obtained using MPMS (Section 6.3). Quantitative TMRX analyses of MNPs in biological samples that could not be performed in the long time regime using the MPMS were successfully conducted using the 6-channel SQUID system (Section 6.4). In addition, potential alterations of the TMRX spectra because of interaction with the biological tissue were evaluated.

1.4 Clinical Applications of Magnetic Nanoparticles

1.4.1 Drug Targeting

Since the earliest days, drugs have been a cornerstone of traditional medicine. Their formulation and administration are both important factors in determining the success any treatment. From orally administered pills to parenterally injected liquids and inhaled aerosols, a broad variety of dosage forms have been invented to provide a full spectrum of treatment options. However, regardless of their route of administration, the distribution of drugs within the body was not controllable until the recent development of antibody-drug conjugates.

Depending on the location of administration the drugs either diffuse into neighboring tissues or are absorbed by the bloodstream for systemic dispersion. Systemic delivery often makes it necessary to administer a higher overall dose in order to attain and maintain a certain local drug concentration. As a result, healthy cells are also exposed to a potential harmful drug and filtering organs such as the liver and spleen can be overly stressed. Chemotherapy treatments for cancer provide prominent examples of the devastating effects of nonspecific drug distribution. It is also noteworthy that some areas of the body are difficult to reach with traditional injection methods because local tissue barriers (e.g. the blood–brain barrier and blood–retina barrier) need to be damaged in order for the therapeutics to pass through [102]. As a consequence, potential treatable diseases such as retinal degeneration are practically untreatable with traditional methods. These two problems, i.e., uncontrolled drug dispersion and inaccessibility of certain areas within the body, clearly support the need for and potential of an in vivo drug manipulation mechanism.

With the first magnetic nanoparticle solutions patented in 1965 by NASA engineer Steve Papell [87], a new tool was available for controlling fluids through the forces of magnetism. Papell's *Ferrorfluid* was a kerosene-based dispersion containing micro- and nanometer scale iron oxides originally designed as a magnetically controllable liquid rocket fuel. In the late 1970s, Widder [94] [95] and Senyi [82] adapted Papell's invention so that a magnetic fluid could transport therapeutics to specific target sites within the body. In this first medical application of a ferrofluid as a drug carrier, the researchers used magnetic microspheres to encase the drug. Later, research teams bound the therapeutic molecules directly to the coatings on the iron oxide nanoparticles [54].

When a high gradient magnetic field is applied to free magnetic nanoparticles, they experience a dragging force toward the center of the magnetic field. If the surface of the particles is additionally combined with a therapeutic molecule, the particles can be used for so-called drug targeting, i.e., the magnetic guiding of therapeutics to the intended target site within the organism. While nanoparticle fluids can be prepared using a variety of liquid media, only aqueous suspensions are relevant for medical applications. The drug-carrying nanoparticle solution is injected into the vascular system and then, exposed to high gradient magnetic fields that guide the particles to the intended target site. When the particles reach their target, they are held in position long enough to release the therapeutic agents into the surrounding tissue. The release can be supported through changes in the surrounding pH, enzymatic activity or temperature [3]. Finally, the external magnet is switched off so that the particles can move freely and be filtered out by the macrophage system.

For successful and safe clinical application, different requirements for the particle coating and magnetic core, the external magnetization mechanism, and the entire process must be fulfilled [65]. The particle core often consists of the iron oxides maghemite, or magnetite which offer good magnetic characteristics while being well tolerated and generally biocompatible. However, there is potential for optimization of the core shape and diameter because these parameters influence the cellular uptake of nanoparticles [14] and their magnetic properties. The choice of coating for the particles is significant because it determines their hydrodynamic diameters and surface structure, and both of these parameters influence the cellular uptake, clustering potential, and hydrodynamic flow velocity of the particles. Thus, the particle core and coating must be specifically designed for the particular task because the physical environment and operating conditions may vary. In addition, the particles must be sufficiently small to move freely through the capillaries but at the same time sufficiently large to be affected by the magnetic field and overcome the opposing hydrodynamic forces of the bloodstream. Furthermore, the applied particle concentration must not be too dense in order to avoid agglomeration and thromboses. Finally, the MNPs must be completely biodegradable and biocompatible in order to avoid long-term accumulation within the tissues.

Because the magnetic forces decrease cubically with distance, strong, high-gradient permanent magnets are required to create a sufficient dragging force to move the particles that are farthest from the surface of the body. In fact, it has been shown that drug targeting for chemotherapy works best for superficial tumors [30]. To overcome the depth limitations, however, it is possible to temporarily implant small magnets close to the tumor region [103].

Different mechanisms for the release of the active agent at the target site are beeing investigated. External triggers, such as, ultrasound [74], light [104], heat [105], electricity [26], and magnetic AC fields [10] allow the technician to determine the point at which the active therapeutic agents should be released. These mechanisms tent to offer greater reliability than physiologically triggered release mechanisms because the physiology may vary from patient to patient.

Currently, the most promising biomedical applications for magnetic drug targeting include chemotherapeutic treatment of brain [72], liver [98], and breast [53] cancers. However, other prominent applications for magnetic drug targeting also exist in the fields of cardio- and endovascular diseases, e.g., stenosis and thrombosis. Here, nanoparticles assist the delivery of therapeutic drugs to endothelial cells, which are located along the inner walls of the blood vessels [76] [77]. In addition, magnetic nanoparticles also have the capability to deliver therapeutic genes to specific targets in vivo [19]. In so-called magnetofection the MNPs enhance traditional gene therapy by allowing gene delivery to otherwise non-permissive cells. Magnetic nanoparticles for magnetofection may drastically reduce the incubation time and lower the gene dose required to achieve a high transfection rate [80].

At present, there are only a few applications of magnetic drug targeting of which clinical trials have been successfully completed, the most prominent ones of them being the Phase I studies of Lübbe's group [54], Phase I & II trials of Wilson et al. [98], and the preclinical studies with animal models performed by Alexiou et al. [4]. These trials demonstrated the virtues of cell-specific targeting while also revealing several problems that must be resolved before drug targeting reaches clinical marketability. A challenge that researchers must consider is the scaling problem of animal models. While control of nanoparticles may be practical in a small organism such as a mouse, it may be more difficult in a human because the distance between the particles and the magnet is likely greater. Simply doubling the distance between the magnet and the particles reduces the magnetic field strength at the particles by approximately a factor of eight. Although stronger magnets could be built, they would quickly exceed economic and safety requirements. A closely related issue is the ongoing need for optimization of the properties of the magnetic cores of the nanoparticles. While it is possible to achieve better magnetic behavior with materials other than pure iron oxide [13], the biocompatibility of these materials, including their potential to negatively impact organs such as the spleen and liver, must be evaluated. The design of coating materials is likewise important because certain coatings may lead to particle agglomerations and thromboses [73]. In summary, the current challenges in magnetic drug targeting are to create effective and biocompatible particles that are suitable for use with a safe and economical application method.

1.4.2 Hyperthermia

Another promising field for magnetic nanoparticles is hyperthermia, i.e., heat treatment of cancer cells. In hyperthermia, malign cells are exposed to high temperatures over a defined period of time. The applied heat damages proteins within the cells and triggers apoptosis [56], i.e., controlled cell death. This heat treatment is particularly interesting for cancer therapy; studies indicate that the heat does only minor damage to normal cells but kills the cancer cells [91]. This behavior can be explained through the poorly developed nervous and unresponsive vascular systems of the malign tissue, which leads to inferior temperature regulation for the fast growing cancer cells. However, hyperthermia is nearly always used to enhance other forms of therapy such as radiation and chemotherapy [101]. Hyperthermia treatments are classified as *local*, *regional* or *whole body* depending on the area they tend to affect. In local applications, two therapy modalities are differentiated: actual hyperthermia is heat treatment of tissue with temperatures only slightly above the body temperature (42 °C–45 °C). For this therapy, application times of 30 min to several hours are required to kill the malign cells. Alternatively, a more radical approach is the application of high temperatures (>50 °C) for a short period of time. However, so-called *thermoablation* suffers from side effects because of the sudden death of the tumor cells, which leads to the generation of a large quantity of necrotic material and results in an inflammatory response [62]. Different methods and devices for hyperthermia and thermoablation treatments have been developed that are mainly distinguished by the manner in which the thermal energy is created: capacitive coupling, microwave radiation, ultrasound, laser photoagulation, and radiofrequency phased arrays. When magnetic nanoparticles are used for hyperthermia, they are first injected or magnetically guided into the tumor region and then exposed to an external AC magnetic field. The different particle types are classified based on their specific absorption rate (SAR). This value is an expression of their ability to transduce the energy of the AC field into thermal energy and can be described by a combination of different physical loss processes [21]. These processes include the so-called hysteresis loss, the loss because of Néel and Brownian relaxation, and frictional losses. The hysteresis loss is caused by displacement of magnetic domain walls within the multidomain particles but can deviate from the hysteresis loop of the magnetization curve for the particles. The second loss process, so-called Néel relaxation, describes the internal reorientation of the magnetic moments within the particles. In addition to the internal friction of the Néel relaxation, there is also mechanical friction because of rotation of the particles themselves, which is referred to as Brownian relaxation. Thus, a current focus of several research groups is improvement of the specific absorption rate of magnetic nanoparticles used in combination with AC field generators, which must be in compliance with medical regulations and meet both therapeutic and economic requirements.

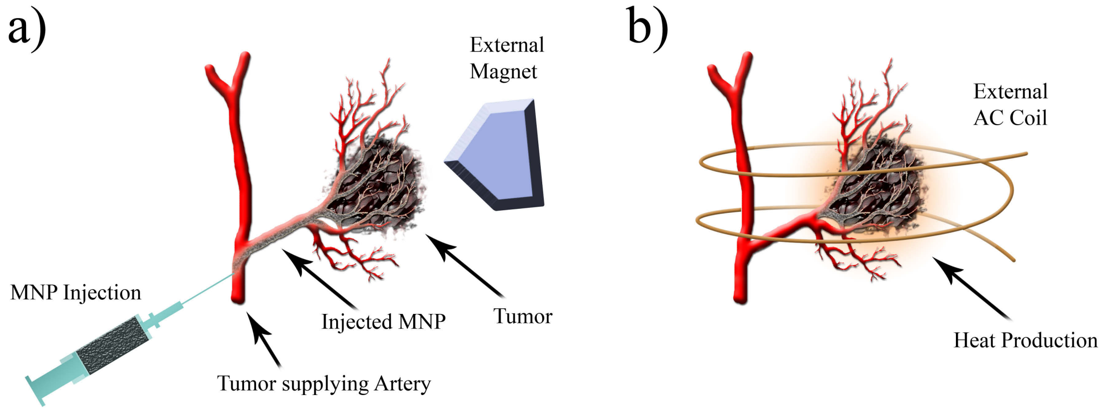

Figure 1.3: **a)** Application of magnetic nanoparticles in a tumor supplying artery. The particles are magnetically guided into the malign tissue using an external high gradient DC magnet. **b)** Once the particles have reached the tumor, an external AC coil exposes the particles to an alternating magnetic field. Because of physical loss processes, the particles heat the surrounding tissue.

Surgeon Richard K. Gilchrist was the first to apply magnetic nanoparticles for the treatment of cancer cells [27]. While Gilchrist injected the particles directly into the malign tissue, researchers have since then demonstrated that magnetic particles can be delivered through the body to the targeted site of action using an external magnet [60]. Research has thus focused on the optimization of treatment methods [34] [55] and the design of the magnetic particles [40]. The first clinical trials with magnetic nanoparticles for hyperthermia were conduced by the research group of Andreas Jordan at Charité, Berlin [89]. In a feasibility study, a small group of patients suffering from malign brain tumor glioblastoma multiforme was treated with aminosilane-coated iron oxide nanoparticles [59].

These first clinical studies demonstrated that hyperthermia treatment with magnetic nanoparticles is a viable therapy that may complement other established therapies. However, this first hands-on experience emphasized many unsolved challenges of the method.

One major problem is the application of the nanoparticles in the tumor and their homogeneous distribution within the tissue. Without uniform distribution of the MNPs within the tissue, consistent heat production cannot be guaranteed. The application method must also ensure selective delivery of the magnetic nanoparticles only to the tumor site. The method used by Gilchrist, i.e., direct injection, has the disadvantage that multiple injections are necessary to achieve a homogenous distribution. While this method offers good control over the local quantity of particles in the tissue, it also increases the risk of spreading the tumorous cells through the puncture wounds. A more promising approach is the coating of MNPs with cancer-specific antibody proteins [18]. Through this specific docking mechanism, the thermal damage of healthy cells is reduced, and even undetected small tumors can be treated. However, the local distribution of the particles is difficult to control, and thus, it is not always possible to guarantee that the quantity of particles bound to the tumor tissue is sufficient to successfully damage the malign cells.

This problem leads to another unsolved challenge in magnetic nanoparticle hyperthermia: the need for a quantitative *in vivo* detection method for magnetic nanoparticles. To date, different imaging methods such as magnetic resonance and x-ray imaging have been investigated for determination of MNP concentrations in tumor tissues. However, while these methods are capable of detecting a certain number of particles, they are not reliably quantitative. Alternatively, the use of the magnetic relaxation signal of the particles to generate a spatially resolved quantitative image appears to be promising [50] [5].

To conclude, hyperthermia using magnetic nanoparticles has high potential to assist established cancer treatments in the near future. Nevertheless, a number of serious problems in different interdisciplinary fields must first be overcome.

2. Theoretical Background

2.1 Magnetism in Nanoparticles

Introduction

Magnetic nanoparticles for clinical applications consist of magnetic iron oxide cores covered by nonmagnetic coatings. The nonmagnetic coatings prevent single particles from aggregating by stabilizing them in solution and serve as carriers for drug and imaging molecules. The size and structure of the coating influence the viscosity of the MNP solution and also its bio-compatibility. In contrast, the magnetic behaviors of nanoparticles are mainly defined by their magnetic cores. Although, numerous types of iron oxides particles exist, only maghemite and magnetite are relevant for biomedical applications [48]. The magnetism of these materials is generally defined by their magnetic domain structures. However, the MNPs investigated in the present study were assumed to be the so-called single-domain particles, i.e., particles that can be described using a single magnetic moment.

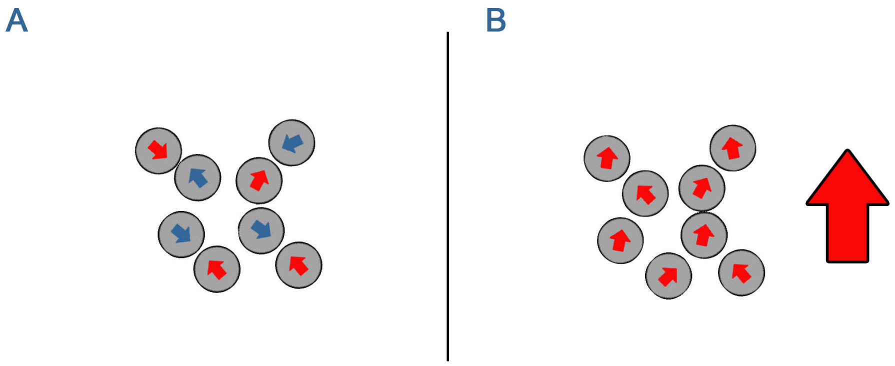

Figure 2.1: Illustration of the magnetic moments in a single domain MNP solution. Each particle consists only of one magnetic domain, which can be described through its magnetic moment and orientation. (A) Without an external magnetic field, the magnetic moments randomly orient into an equilibrium state. (B) With an external magnetic field, the single particles change their orientation in the direction of the external field.

2.1.1 Superparamagnetic Single-Domain Particles

Because the particles are always separated by their nonmagnetic coatings, their single domains are randomly oriented when no external field is applied (Figure 2.1 A). When an external field is applied, the magnetic moments of the particles readily align in the direction of the external field (Figure 2.1 B).

The magnetic moments inside the particles are organized as single domains only for particles with diameters below a critical core diameter [12]. The dimension of this critical diameter depends on the material. In the literature, the values for iron oxides range from 60 nm [66] to 80 nm [36]. The magnetic moment of such a single domain particle depends on the magnetization of the material (M_p) and the particle volume (V_p):

$$m = M_p V_p. \tag{2.1}$$

In contrast to bulk materials, for which the magnetic domains interact strongly with one another, the single domain in a nanoparticle can change its orientation more freely. Similar to the bulk material, the magnetic domains in a group of nanoparticles will oppose and try to cancel one another out in the absence of an external field. However, freely moving single-domain particles can oppose each other more effectively and are less affected by interaction effects resulting from the increased inter-particle distance. The remaining net magnetization will therefore be zero [6]. If a

ferrimagnetic material exhibits no remanent magnetization, it is *superparamagnetic*.
Thermal fluctuations generally affect the magnetic behavior of a material because they can be strong enough to change the orientation of a magnetic domain. The temperature can be seen as an opposing force to the ordering trends of the magnetic domains. Temperature strongly influences both the in-field magnetization process and the loss of the magnetic moment in the absence of an external magnetic field. The magnetization process can be described by the Langevin equation [47], which relates the magnetic energy ($\mu_0 H$) and the thermal energy ($\mathrm{k_B} T$).

$$M(H,T) = M_p \left(\coth\left(\frac{m\mu_0 H}{\mathrm{k_B} T}\right) - \frac{\mathrm{k_B} T}{m\mu_0 H} \right) \tag{2.2}$$

The magnetization (M_p) and the magnetic moment (m) depend on the core material and the particle design. Note that M_p is closely related to the saturation magnetization of the bulk material (M_S) but is typically much smaller than the latter because of surface effects [61]. The physical constant $\mathrm{k_B}$ denotes Boltzmann's constant and μ_0 represents the permeability in free space. Equation 2.2 successfully predict the magnetization patterns observed for typical M(H)-curves of superparamagnetic nanoparticles. In contrast to ferrimagnetic bulk materials, there is no hysteresis in superparamagnetic materials (Figure 2.2 b). In the absence of an external field, the magnetic moments within the superparamagnetic particles reorient themselves into an equilibrium state without net magnetization. This exponential decay of the magnetization amplitude (A) does not occur immediately but after a characteristic time (τ):

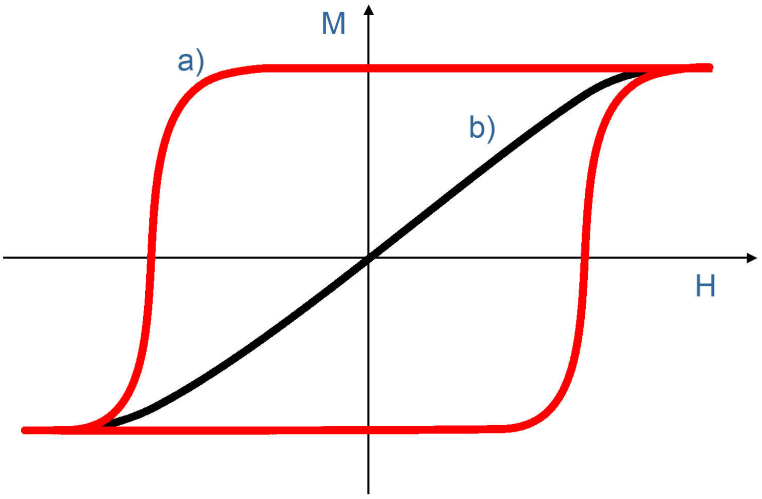

Figure 2.2: Magnetization patterns of **a** ferromagnetic and **b** superparamagnetic materials.

$$M = A \cdot \exp(-\frac{t}{\tau}). \tag{2.3}$$

For a more detailed description of the magnetic behavior of MNPs, the relaxation process can be separated into two different processes: Néel relaxation and Brownian relaxation.

2.1.2 Néel and Brownian Relaxation of Magnetic Nanoparticles

The first observation of superparamagnetic relaxation was documented by the French geophysicist Emile Thellier in 1941 [88]. He measured the magnetization of ancient rocks and pottery, thus performing pioneering work in the new field of paleomagnetism. While investigating the temperature dependence of a sample's magnetism, he observed an unexpected decay of the magnetism over time, a phenomenon today known as relaxation. The origin of this magnetic effect can be explained by considering the collective magnetic moments within the material. If the single magnetic moments are all facing in the same direction, a net magnetization can be measured. However, no magnetization is detectable if the magnetic moments are randomly oriented. On an atomic scale, thermal vibration causes random changes in the orientations of the single magnetic moments [11], thus provoking the decline of the net magnetization. The strength and frequency of these changes therefore defines the time during which the entire system dephases into random orientations. In 1949, Louis Néel published the first theoretical model of this particular magnetic behavior of superparamagnetic particles [64]. He showed that magnetic relaxation can be expressed as an exponential decay with a characteristic decay time, the Néel relaxation time (τ_N):

$$\tau_\mathrm{N} = \tau_0 \exp\left(\frac{KV_c}{\mathrm{k_B}T}\right). \tag{2.4}$$

The Néel relaxation time of a particle is strongly influenced by its anisotropy (K) and core volume (V_c). The anisotropy describes the directionality of the particle, which is determined by its shape (shape anisotropy) and crystalline structure (crystal anisotropy). Because of this directionality, magnetization process for a particle depends on the direction from which the external magnetic field originates. The direction that requires the least energy is referred to as the easy axis, and if the material has only one easy axis, then it has uniaxial anisotropy. The so-called attempt time (τ_0) in equation 2.4 is a time span characteristic of the material, with typical values ranging from 10^{-9} s to 10^{-11} s. The reciprocal of the attempt time is referred to as the attempt frequency. William Fuller Brown, Jr. developed a model for calculating the relaxation time of a ferromagnetic particle using the Langevin equation [11]:

$$\tau_0 = \frac{1+(\eta\gamma_0 M_s)^2}{\eta\gamma_0^2}\frac{\sqrt{\pi}}{4K}\left(\frac{\mathrm{k_B}T}{KV}\right)^{1/2}. \tag{2.5}$$

Although τ_0 can have different values because it is temperature dependent, it is often assumed to be a constant. This approximation is in most cases reasonable because the temperature dependent changes in the relaxation time, as defined in Equation 2.4, overshadow the relatively small alterations in τ_0. During 1994–95, the theory for magnetic nanoparticle relaxation with uniaxial anisotropy was developed further by Coffey et al. [16], and the influence of a constant magnetic field transverse to the easy axis of the particles was simulated [15].

Néel relaxation plays an important role in the magnetic behavior of superparamagnetic nanoparticles and an understanding of this phenomenon is crucial for their use in different clinical applications, including hyperthermia and magnetic particle imaging. However, the Néel relaxation in nanoparticles is often overshadowed by *Brownian* relaxation. In 1929, Peter Debye described the random changes in the orientation of a free floating particle because of collisions with other particles. In this type of relaxation, a single particle can change its orientation by turning its whole body. Naturally, the Brownian relaxation time (τ_B) is significantly influenced by η, the viscosity of the fluid surrounding the particle:

$$\tau_\mathrm{B} = \frac{3\eta V_h}{\mathrm{k_B}T}. \tag{2.6}$$

In general, the hydrodynamic volume (V_h) includes of the iron oxide core volume (V_c) together with a non-magnetic coating with thickness δ. However, if the particles aggregate and form clusters, their hydrodynamic volume can reach much larger values. In combination with the Boltzmann constant (k_B) the temperature (T) in Equation 2.6 has an accelerating or retarding effect on the relaxation process. Both, the Brownian relaxation time (Equation 2.6) and the Néel relaxation time (2.4), are highly sensitive to the particle size and system temperature. However, while τ_B only grows linearly with particle size, τ_N increases exponentially. Since the two relaxation types may occur simultaneously, the effective relaxation is a combination of both processes:

$$\tau_\mathrm{eff} = \frac{\tau_\mathrm{N}\tau_\mathrm{B}}{\tau_\mathrm{N}+\tau_\mathrm{B}}. \tag{2.7}$$

The overall relaxation time of magnetic nanoparticles may vary by several orders of magnitude depending not only on the particle properties (e.g., anisotropy) but also on the system parameters (e.g., temperature and magnetization time). In addition, the measuring time plays an important role in relaxation measurements. In order to observe a relaxation signal at a defined temperature, the timescale of the applied measurement technique must be carefully adjusted for each given sample such that both the relaxation and measuring times are of the same order. If the relaxation is fast compared to the measuring time, no relaxation will be observed and only the sample's magnetization at zero field is detected. If the relaxation is too slow for the measurement timescale, only a value similar to that of the in-field magnetization of the sample is obtained. The relaxation can be perceived only if the relaxation time and measuring time are of the same order. In typical investigations, the measuring time is often held constant while the temperature is varied. The temperature at which the superparamagnetic relaxation time is equal to the measuring time is referred to as the *blocking temperature* (TB).

2.1.3 Particle Distribution

Magnetic nanoparticle samples typically do not consist of particles with uniform core sizes, but a distribution of variably sized particles. In 1976, Granqvist et al. [29] reported that the particles they investigated exhibited a log-normal distribution. Although the origin of the log-normal distribution in MNP systems is still disputed, it is a general consensus that most particle suspensions have log-normal core size distributions. This distribution is described by Equation 2.8:

$$P_d(d, \mu_d, \sigma_d) = \frac{1}{\sqrt{2\pi}\sigma_d d} \exp\left(-\frac{\ln^2(d/\mu_d)}{2\sigma_d^2}\right). \tag{2.8}$$

Assuming a spherical particle core, the diameter (d) can also be expressed as the core volume (V). The volume for a single particle may also be expressed as a function of its magnetic moment (m) and saturation magnetization (M_S) as given in Equation 2.9:

$$m = M_s V. \tag{2.9}$$

Inserting equation 2.9 into 2.8 leads to the log-normal distribution of the magnetic moments within an MNP sample:

$$P_m(m, \mu_m, \sigma_m) = \frac{1}{\sqrt{2\pi}\sigma_m/3m} \exp\left(-\frac{\ln^2(m\mu_m)}{2(\sigma_m/3)^2}\right). \tag{2.10}$$

2.1.4 Dipole–Dipole Interactions

A great number of models describing the dynamics of nanoparticles have been developed for non-interacting nanoparticles. However, experimental data often differs from the predicted results, indicating that interactions between the particles may play an important role. This deviation from the experimental data often appears as a difference in the relaxation time (τ).

There are different types of interactions known to influence MNP and define their characteristic behaviors and relaxation times, ranging from more physical interactions such as thermal vibrations, streaming turbulence around the particles, and even binding of particles to one another or to larger structures to elemental interactions on a molecular level that define the magnetism of the substance. On the molecular level, the exchange interaction between electrons plays a major role in connecting the electron spins to a macroscopic magnetic moment providing an explanation for the existence of magnetic domains [36]. However, the exchange interaction is too short-ranged to influence single domain particles that are separated by a nanometer-thick coating. Compared to the exchange interaction energy, long–range dipole–dipole interactions are weak; despite this fact, they play an important role for ferro- and ferrimagnetic nanoparticles with sufficiently small inter–particle distances, such as in high-concentration solutions or samples in which the particles are unevenly distributed because of sedimentation or aggregation. In such samples, dipole–dipole interactions can lead to the formation of a collective state of the magnetic moments. In this collective state, the MNP sample often displays a longer relaxation time. This behavior is also referred to as *spin glasses*. In addition the close proximity of the magnetic cores can lead to the formation of chain–like superstructures and alignment of the magnetic moments.

In order to investigate the influence of dipole–dipole interactions for ferrimagnetic nanoparticles, Zang et al. [106] performed AC-susceptibility analyses of frozen suspensions of magnetite particles in kerosene. When trying to describe the measurements using Néel relaxation (Equation 2.4), they experienced problems fitting the measured values for τ to the different concentration steps. In the Néel relaxation equation, the parameters for anisotropy and particle volume should not change with concentration, and thus the only variable parameter is the attempt time (τ_0). However, the fitted values for τ_0 fell in an atypical range for magnetite. In this instance, the Néel relaxation equation apparently lacked a parameter that expressed the influence of the MNP concentration. The temperature dependence of the samples appeared to be better phenomenologically described using the empirical Vogel–Fulcher law, which includes the critical temperature (T_0):

$$\tau = \tau_0 \exp\left[\frac{\Delta E}{k_B(T-T_0)}\right]. \tag{2.11}$$

Subsequent studies of nanoparticle interactions [32] have shown that, in most cases, the critical temperature (T_0) in the Vogel–Fulcher law can be related to the dipole interaction energy:

$$T_0 \approx \frac{E_{dipole}}{k_B}. \tag{2.12}$$

The interaction energy (E_{dipole}) may in turn be described as a function of the magnetic dipole–dipole interactions between two ideal magnetic dipoles ($\vec{m}_i$ and $\vec{m}_j$) [37]:

$$E_{dipole} = \frac{\mu_0}{4\pi}\left[\frac{\vec{m}_i \cdot \vec{m}_j}{r_{ij}^3} - \frac{3(\vec{m}_i \cdot \vec{r}_{ij})(\vec{m}_j \cdot \vec{r}_{ij})}{r_{ij}^5}\right], \tag{2.13}$$

where $\vec{r}_{ij}$ is the distance vector between the centers of the two magnetic dipoles. However, in an ensemble of nanoparticles with an average magnetic moment and an average distance (D), the dipole interaction energy is often simplified to [69]:

$$E_{\text{dipole}} \approx \frac{\mu_0}{4\pi}\frac{m^2}{D^3}. \tag{2.14}$$

If D in an MNP solution decreases, for instance when the particles aggregate, the relaxation time of

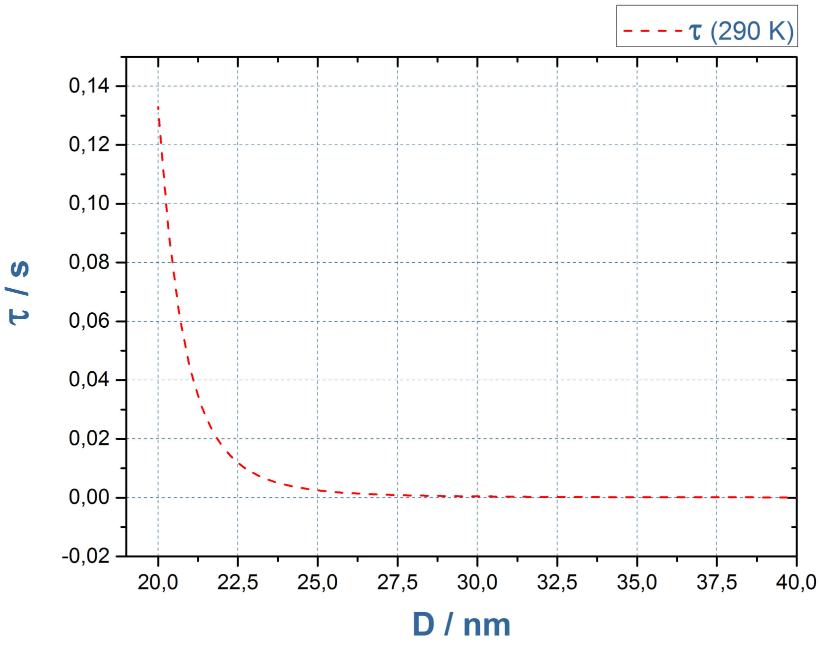

Figure 2.3: Influence of the particle distance (D) on the Néel relaxation time (τ). With decreasing distance, the MNP relaxation time increases exponentially. The relaxation time of a 20 nm particle at 290 K is displayed.

the sample increases (see Equation 2.3). Through this variable parameter D and the Vogel–Fulcher law (Equation 2.11), the deviation of the experimentally determined relaxation signals and the values calculated using the Néel relaxation equation can be explained. Most studies of the dipole–dipole interactions of MNPs have been performed on immobilized samples with a narrow size distribution. The broad distribution of their blocking temperatures would cover possible interaction effects and make them difficult to detect. This specific problem is discussed in Chapter 5.3, where a method is introduced for including the size distribution into dipole interaction equations.

These dipole–dipole interactions must be taken into account for ferro- and ferrimagnetic nanoparticles. For anitferromagnetic particles, however, dipole interactions are negligible. The majority of studies on dipole–dipole interactions have shown an increase in the relaxation times and blocking temperatures of such samples. However, Mössbauer studies of maghemite nanoparticles have revealed that weak particle interactions result in a decrease in the relaxation time [71] [63], which has been explained by a lowering of the average value of the energy barriers separating the minima of the magnetic energies [38] [32] [7] [8].

3. Measuring Principles

3.1 Magnetorelaxometry (MRX)

3.1.1 Basic Principles

One way to characterize the magnetic performance of small magnetic nanoparticles is to investigate their ability to react to a rapidly changing magnetic field. A typical technique involves the application of an alternating external magnetic field at a defined frequency. In contrast to direct current (DC) analyses, which measure the equilibrium value of the magnetization in a sample, alternating current susceptometry (ACS) provides information about the magnetization dynamics of the MNPs [17], i.e., how rapidly the magnetization can change.

Another method for investigating the dynamic performance of MNPs is magnetorelaxometry (MRX). A typical MRX analysis consists of two phases: a magnetizing phase, in which the sample is exposed to a defined external magnetic field B for a time t_{mag}, followed by a measurement phase during which the external field is turned off and the declining net magnetic moment of the sample is measured (Figure 3.1). Unlike in ACS, no external field is applied during the actual measurement.

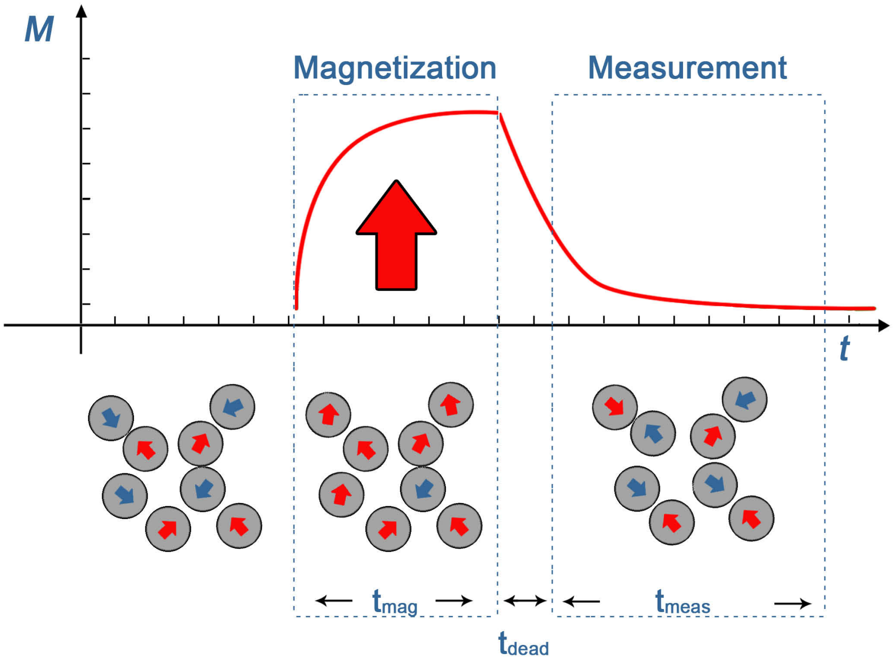

Figure 3.1: Procedure for MRX analyses: Prior to the magnetizing phase, the particles are randomly oriented and no net magnetic moment is detectable. When the external magnetic field is applied, the magnetic moments of the particles align in the direction of the field when it is applied, and then after a short delay time following switch-off of the field, the relaxation is measured. During this measurement phase, the single magnetic moments of the MNP sample realign into a random equilibrium. The magnetic moments colored in red are aligned in the direction of the external magnetic field while the opposing moments are colored in blue.

The detected signal can therefore be assigned to the decaying net magnetic moment of the sample. At the beginning of a measurement, it is assumed that the sample has no remanent magnetization and the single magnetic moments of the MNPs are randomly oriented. During the magnetization phase, the single magnetic moments in the sample align in the direction of the external DC field and create a macroscopic magnetic moment. When the external field is turned off, they seek to reach their equilibrium state once again. In this equilibrium, the magnetic moments are randomly oriented and oppose each other so that there is no remaining macroscopic moment. This decay of the magnetic moment is called relaxation. Relaxation because of the physical rotation of entire particles is referred to as Brownian relaxation, whereas relaxation because of reorientation of the magnetic moments of MNPs is considered to be Néel relaxation. The relaxation of a sample's net magnetic moment is detected over a specified measurement time (t_{meas}) using SQUIDs, i.e., sensitive magnetic field sensors. The control electronics of the SQUID require a certain delay time between the magnetization and measurement phases. This delay time (t_{dead}) is typically in the range of microseconds but can extend to several seconds depending on the behavior of the measurement system.

The relaxation time of a particle sample is determined by both its particle characteristics and the predominant relaxation type. Whether the relaxation mechanism for MNPs is dominated by Brownian or Néel relaxation depends on their particle sizes and mobilities. Brownian relaxation only occurs when the particles are freely moving in a solution; immobilized particles may only relax via Néel relaxation. Although both relaxation types may occur in a sample simultaneously, according to Equation 2.7, the resulting relaxation time will be dictated by the faster relaxation. For nano scale particles, Brownian relaxation is several orders of magnitude faster than Néel relaxation and therefore clearly distinguishable. In addition, the magnetic core sizes, anisotropies and hydrodynamic diameters of MNPs determine how fast they undergo magnetic relaxation. In this dissertation, only immobilized particles were investigated. Therefore, Brownian relaxation was neglected. The Néel relaxation of the investigated samples, however, provided information about the magnetic core sizes, anisotropies, and aggregation states of the MNPs.

3.1.2 Magnetorelaxometry Measurement Setup

In a typical MRX setup for conducting analyses at room temperature, a small MNP sample (a few µL) is placed in the center of the magnetization coil (Figure 3.2). The magnetization units typically consist of Helmholtz coils [58] that create a homogeneous magnetic field in the sample space. Depending on the coils, the applied field strength can reach several millitesla. The sample magnetization is typically of the order of seconds. A longer magnetization time is necessary only for relaxation measurements using magnetic property measurement systems and similar devices, which have long switch-off times (see also 4.1.3). The length of the measurement phase depends on the relaxation behavior being investigated.

Larger particles typically display a longer relaxation than MNPs with smaller diameters. In these larger particles, Brownian relaxation is often the predominant relaxation type, whereas smaller MNPs relax mainly via Néel relaxation. If MNPs that display Brownian relaxation are immobilized, their relaxation times increase by several orders of magnitude. In general, the measurement time is of the same order as the magnetization time.

The relaxation signal of a particle sample is typically measured using sensitive magnetometers such as SQUIDs, fluxgates [57], and optical magnetometers [41]. To reduce magnetic far field distortions, these sensors are often arranged in a gradiometer setting. SQUID–based MRX systems are often preferred because highly sensitive SQUIDs excel with respect to their measurement accuracy, and they can detect magnetic fields in the picotesla range. They do, however, require special magnetically shielded environments such as the BMSR-2 [9] because the magnetic background signal is in the microtesla range. In addition, superconducting SQUIDs come with high operational costs because they require excessive cooling. While low–temperature SQUID systems require liquid helium as the coolant, high–temperature SQUIDs may be operated using liquid nitrogen, which is cheaper. Furthermore, the thermal insulation needed between the SQUID sensor and the nanoparticle sample also reduces the overall detection limit of the system because the magnetic signal of the sample decays cubically with distance. In all MRX systems, it is therefore desirable to place the sample as close as possible to the magnetic sensor. Finally, because of their high sensitivity to magnetic field changes, SQUID sensors must be switched off during the magnetization phase because they may otherwise be driven to saturation and overload. Switching off of the magnetization coil results in the need for a short dead time because the coil's magnetic field does not instantaneously cease. Depending on the switch–off process of the coil and the possible flux creep in the Dewar the necessary dead time of the SQUID can range from 10 µs to minutes (see also Chapter 4.1.3). A shorter delay time is generally desirable because the detection limit of a system increases exponentially as the delay time decreases.

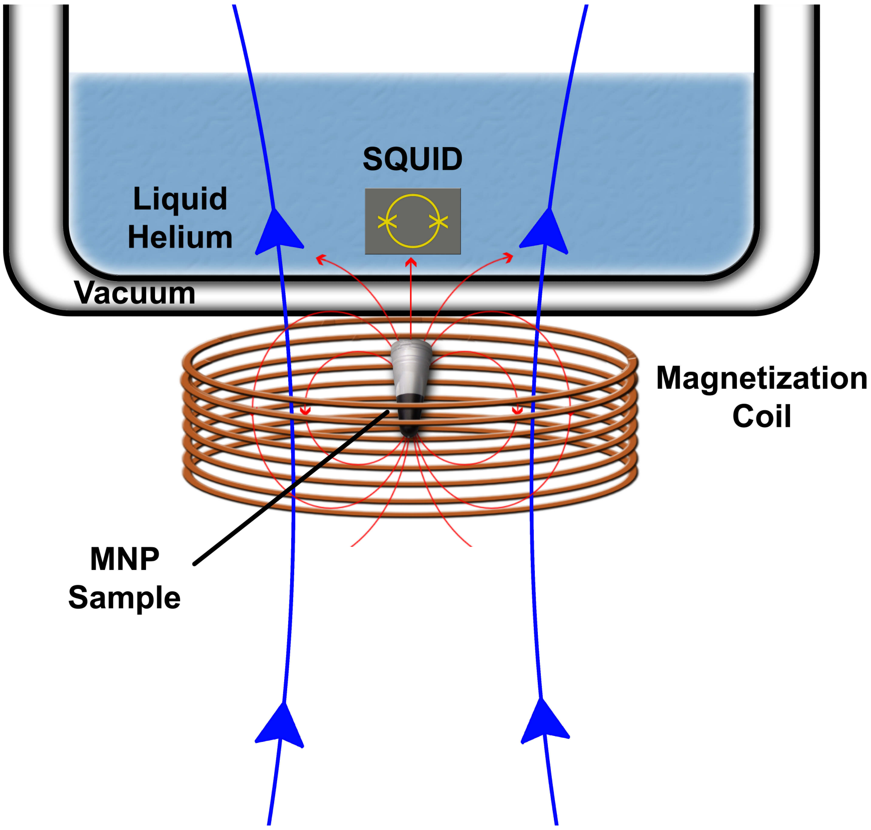

Figure 3.2: Typical MRX setup: The magnetization coil creates a homogeneous magnetic field in the sample space during the magnetization phase (blue arrows). After switching off the coil, the SQUID detects the decaying net magnetic moment of the MNP sample. The magnetic field of the sample is illustrated in red. The superconducting, low–temperature SQUID sensors require liquid helium as coolant in order to operate inside the insulating Dewar vessel.

3.2 Temperature Dependent Magnetorelaxometry (TMRX)

3.2.1 Basic Principles

Measurement of the magnetic relaxation signal allows investigation of the dynamic magnetic behavior of MNPs. This relaxation behavior strongly depends on the particle core size, analysis temperature, and measurement time window. At room temperature, only particle core sizes of approximately 15 nm – 25 nm [97] are detectable with typical MRX systems.[1] In addition, in order to detect a certain particle type, its relaxation time constant (τ) must be of the same order as the measurement time. Within a fixed time window, particles above a critical diameter will relax too slowly to contribute significantly to the amplitude change during the measurement phase. In addition, the net magnetic moment for small particles below a certain diameter will have already decayed prior to initiation of the measurement phase. According to the equation for Néel relaxation (Equation 2.4), reducing the temperature of an MNP sample should lead to a longer relaxation time and therefore a slower relaxation process.

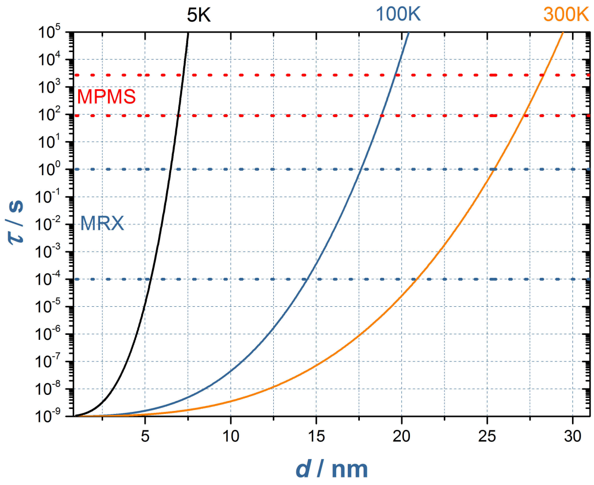

Figure 3.3: Measurement ranges for the MPMS and MRX 6-channel SQUID systems for particles of different sizes at 5 K, 100 K, and 300 K. The Néel relaxation time (τ) was determined for monodisperse particles with an effective anisotropy of $1 \cdot 10^{4}$ J/m^{3} that are not affected by dipole-dipole interaction (Equation 2.4)

During the measurement phase, after the single magnetic moments have been aligned by the external magnetic field, thermal vibrations of the single magnetic domains have a certain probability for changing the orientation of the net magnetic moment. This probability increases with increasing temperature. In order to investigate particles with core sizes < 15 nm, it is worthwhile to slow down their relaxation processes by lowering the analysis temperature. Previously, Romanus and Berkov et al. showed that temperature dependent magnetorelaxometry is a valuable, complementary method for the analysis of magnetic nanoparticles. However, they focused on the energy barrier distribution [75] of the MNPs and not on the biomedical applications. The MPMS offers great capabilities for performing different magnetic measurements at temperatures as low as 5 K. However, because of the design of the instrument, the time between switching off the magnet and measuring the first data point is rather long at 1,5 min (see also 4.1.3). This long dead time requires extended magnetization and measurement phases in order to detect particles. The MPMS is therefore only capable of measuring long relaxations in a measurement time window of 40 min, which restricts the spectrum of detectable particles to those whith core diameters ranging from 26 nm to 28 nm at room temperature. The measurement range of the MPMS is indicated in Figure 3.3 by dashed red lines. Néel relaxation times at 300 K for particles of different sizes as determined according to the interaction-free Néel relaxation equation (Equation 2.4) are indicated by the orange line in the figure. At a sample temperature of 100 K (blue line), the Néel relaxation of MNPs with 17 nm to 19 nm magnetic cores is observable while at 5 K, only very small MNPs with core diameters of approximately 7 nm relax within the time window of the MPMS (black line).

---

[1] The measuring range of 15 nm to 25 nm applies to particles with moderate dipole-dipole interaction. MNPs with core diameters of less than 15 nm can also be measured at room temperature if they are influenced by strong dipole-dipole interaction.

3.2.2 Creation of the TMRX Spectrum

By measuring the relaxation times at different temperatures using the MPMS, it is possible to screen the relaxation spectrum of a sample. In a typical TMRX plot, the amplitude change of the sample's relaxation is plotted as a function of temperature (Figure 3.4 left). This information can be used to determine the core size of the MNPs and the sample concentration (4.2). In addition, the temperature dependent relaxation signal is a sensitive indicator of dipole–dipole interactions between the particles (4.4).

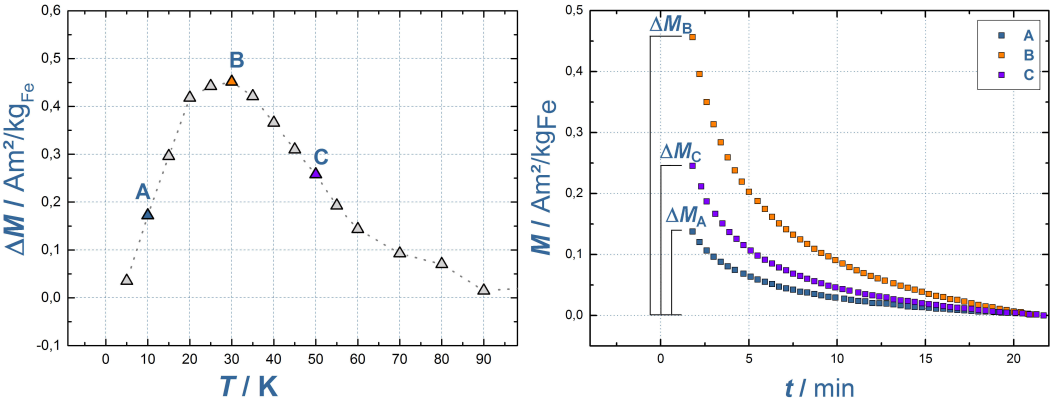

Figure 3.4: Left: A typical TMRX plot where the amplitude change (ΔM) is displayed as a function of temperature. The maximum relaxation amplitude was observed at 30 K, indicating that the investigated MNPs had a magnetic core size of 7 nm to 10 nm. Right: Single relaxation curves at selected temperatures. The amplitude change is more or less pronounced depending on the temperature.

3.2.3 Influence of the Particle Core Size on the TMRX Spectrum

The relaxation behavior of an MNP is described by its relaxation time (τ). Néel showed that this relaxation time depends on the system temperature (T) and the magnetic moment of the particle (m):

$$\tau_{\mathrm{N}} = \tau_0 \exp\left(\frac{Km}{M_s \mathrm{k_B} T}\right). \tag{3.1}$$

Parameters such as the attempt time (τ_0), the anisotropy (K), and the magnetization saturation (M_s) are constants that are directly related to the properties of the magnetic nanoparticle. In contrast, Boltzmann's constant ($\mathrm{k_B}$) is a natural constant. The system temperature (T) in Equation 3.1 has a strong influence on the relaxation time; a change in this temperature not only changes the value of the entire fraction but also has exponential influence on τ. The numerator is mainly determined by the magnetic moment (m) of the particle and is in turn connected to the magnetized volume through the relationship $m = M_s V$. The relaxation time is thus influenced by the relationship between the particle's core size and temperature. By defining a constant measurement time (t_{meas}), a fixed time window is created wherein the relaxation amplitude change (ΔB) can be measured. The amplitude change that occurs during t_{meas} is displayed for different measurement temperatures. If τ is too small, no relaxation will be detected in the time window because the particles will have already relaxed during the switch-off time. Similarly, no relaxation will be detected in the time window if the relaxation time is too long. A particle of a certain size will only reach its highest ΔB for a fixed timeframe at a defined temperature. When ΔB is plotted as a function of T, a peak at a certain temperature is observed that is directly related to the MNP core size (Equation 3.5) if interactions can be neglected.

Thus, TMRX spectra may be used to determine the characteristics of MNPs. This analytical method was introduced by Berkov and Romanus et al. [75], who coined the term *TMRX*. They explained the different relaxation amplitudes in terms of *energy barriers*. They also demonstrated that the magnetic particle core size distribution can be determined if the anisotropy of the sample is known. Alternatively, if the magnetic particle core size distribution is known from other analyses, TMRX can be used to determine the anisotropy distribution. The impact of dipole–dipole interactions on the relationship between the peak temperature and particle size is discussed in Chapter 4.4.

3.2.4 Influence of the Particle Core Size Distribution on the TMRX Spectrum

If a particle sample contains only one specific particle size or has a sufficiently narrow size distribution, it is considered to be monodisperse. Depending on the particle size, there will be a range of temperatures at which the relaxation can be detected within a constant time window. As explained in Chapter 3.2.3, the temperature dependency of the relaxation will lead to a defined peak temperature at which the relaxation amplitude change is the most pronounced. Even for a monodisperse sample, the TMRX spectrum will be a peak shaped function. If the particle sample also contains MNPs with other core diameters, the resulting signal will be a combination of the individual relaxations. If the second particle type is much larger or smaller in diameter, the TMRX spectrum will exhibit a second peak. However, if the two particle types have similar particle diameters, the TMRX spectrum will *broaden*, i.e., the temperature range at which the relaxation is measured will be increased.

Most particle samples have a relatively broad log-normal distribution of different particle sizes. This distribution can be expressed using the median diameter ($\tilde{d}$) and a variance (σ) according to Equation 2.8. Therefore, the variance directly influences the temperature range of the TMRX signal, and a broader particle distribution results in a broader TMRX peak.

The peak temperature indicates the median core diameter in the MNP sample while the broadness of the TMRX spectra indicates the diversity of the core diameters in the sample. However, particle interactions may alter the peak temperature, which makes interpretation of TMRX spectra more difficult.

3.2.5 TMRX using a Magnetic Property Measurement System

Because one relaxation measurement using the MPMS takes approximately 40 min, the overall analysis time for one sample can be 10 h to 12 h. Therefore, only a limited number of relaxation measurements are typically performed for a given sample; a typical TMRX analysis using the MPMS only consists of approximately 20 single relaxation measurements. It would be advantageous to reduce the measurement time in order to increase the sampling rate and obtain more detailed TMRX spectra. The TMRX measurements performed in the present study using the MPMS are presented in Chapter 4. Additional information about the MPMS, its programming, and a typical analysis procedure can be found in Appendix 8.1.

Analysis Procedure for TMRX using a Magnetic Property Measurement System

Using an MPMS, temperature dependent relaxation measurements were conducted at 5 K– 300 K. The different temperatures and magnetic fields were set using Multi-VU sequence commands (see Appendix 8.1). For each temperature, a magnetizing field of 1 mT was applied for 8 min in order to magnetize the MNPs in the sample, followed by recording of the relaxation signals for approximately 40 min. In the recording phase, the magnetic moment of the sample was detected 100 times in a row. The switch–off time of the 1 mT field from the superconducting magnet was

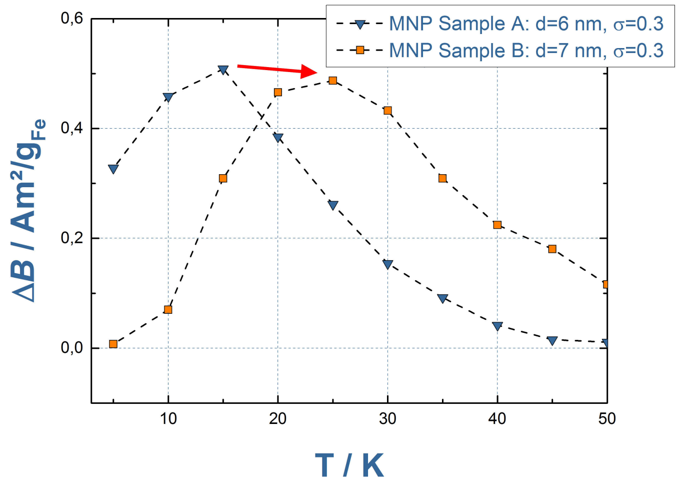

Figure 3.5: TMRX signals of two similar MNP samples differing only in their magnetic core diameters. Sample **A** (blue), with a core diameter of 6 nm, had a maximum relaxation amplitude at 15 K, whereas sample **B** (orange), with a core diameter of 7 nm, exhibited its maximum relaxation amplitude at 25 K. The different peak temperatures are indicated by the arrow. Because of the similar size distributions of the two particle samples, the shapes of the two curves resembled each other, even though the peak temperatures for the two particle systems were different.

approximately 1,5 min, during which the SQUID could not be turned on to detect the magnetic moment. To determine the magnetic moment from the measurement data, the reciprocating sample option (RSO) mode was used. During the first 5 min of the relaxation measurement phase, the MPMS only performed single RSO scans; in the latter portion of the measurement phase, three repetitions of each RSO scan were performed. The RSO scans with one repetition had a shorter measurement time and a lower accuracy than those obtained using three repetitions.

Measurements in the Reciprocating Sample Option (RSO) Mode

In the RSO mode, the sample was moved stepwise through the second-order gradiometer superconducting pick up loop. During the analysis, the SQUID voltage and sample position were measured, and the results were fitted to a model to determine the magnetic moment of the sample.

In a typical RSO measurement the sample is positioned in the sample holder at the end of the sample rod which is then placed in the sample chamber through the airlock. The sample rod is held at the top by the RSO-Motor. The motor then moves the sample sinusoidally through the pick up coils. A change of the sample's position comes along with a change of the flux in the system. The pick up coils induce a current into the superconducting circuit depending on the flux to which they are exposed. The position of the sample rod is tracked by a shaft encoder on the servo motor. To lower the signal to noise ratio, the sample is moved several times through the pick up coils and the measurements are averaged. The final RSO measurement therefore consists of the absolute SQUID voltage at each position of the sample rod within the sample chamber. The incline of this bell shaped curve is then fitted and compared to the calibration curve of a palladium standard sample. This standard sample imitates a point dipole with an accuracy up to 0,1 %. For an exact fit the unknown sample should therefore have small spacial proportions of about 3 mm in diameter and 3 mm to 5 mm in height.

3.2.6 TMRX using the 6-Channel SQUID System

The 6-channel SQUID system is an alternative device capable of MRX measurements [2]. The crucial advantage of this instrument is the reduced dead time because of its optimized, non–magnetic design. The short delay time allows measurement of the relaxation to begin within 100 µs – 1 s after switch–off of the magnetizing coil.

The faster measurement window results in the detection of different particle spectra at room temperature. The measurement time window of the system is illustrated as dashed blue lines in Figure 3.3. Compared to the MPMS, the 6-channel SQUID system detects a broader range of particle sizes at a defined temperature because of the different measurement time window. For instance, at 300 K particles with core diameters of 22 nm to 26 nm are detectable. The 6-channel SQUID system does not, however, have a sample cooling option installed and is therefore only capable of analyses at room temperature.

In Figure 3.3, the range of detectable particles would also be increased if the fast measurement time window was combined with low-temperature analysis. At 5 K, even small particles with a 5 nm core would be detectable with the 6-channel MRX system. In addition, the faster magnetization and measurement times would significantly reduce the overall measurement time. For a single sample, the overall measurement time would mainly be determined by the cooling time. Furthermore, because one relaxation measurement could be performed every three seconds, the sampling rate for TMRX analysis could be significantly increased. With a higher sampling rate, more detailed information about the particle distribution could be obtained. In particular, small sub–maxima next to the main temperature peak that are hidden at lower sampling rates may become visible. Because the magnetic relaxation moment of the sample decays exponentially with time, the delay after switching off the magnetization coil also has a significant effect on the relaxation signal strength. The shorter dead time of the 6-channel SQUID system would therefore increase the relaxation signal strength, which could in turn be used to reduce the necessary magnetization time. Thus, the detection limit of the system could be increased because of the gain in the relaxation amplitude.

The above mentioned advantages make the expansion of the 6-channel SQUID system for TMRX desirable. In order to do so, a helium flow cryostat must be designed as a sample cooling unit. The design and implementation of the cryostat is discussed in Chapter 6.

II

Results

4 **TMRX Analyses in the Long Time Regime** 51
4.1 Data Analysis for the Magnetic Property Measurement System
4.2 Influence of Magnetic Nanoparticle Amount on the TMRX Spectrum
4.3 Influence of the Magnetizing Field Strength on the TMRX Spectrum
4.4 Influence of Particle Aggregation on the TMRX Spectrum
4.5 Multicore Particle Analysis via TMRX of Underlying Fractions

5 **Numerical Simulation of TMRX Spectra** 77
5.1 Influence of Dipole–Dipole Interactions on the TMRX Spectrum
5.2 Simulation of TMRX Spectra of Non–Interacting Particles
5.3 Simulation of TMRX Spectra Including Dipole–Dipole Interactions

6 **Development of a TMRX System for the Short Time Regime** 89
6.1 Custom TMRX Measurement System
6.2 Characterization of the GRP Cryostat with Magnetizing Coil
6.3 Quantification of Magnetic Nanoparticles using TMRX in the Short Time Regime
6.4 Quantification of Magnetic Nanoparticles in Biological Tissues using TMRX in the Short Time Regime

7 **Conclusion** 113
7.1 Summary and Conclusion

4. TMRX Analyses in the Long Time Regime

4.1 Data Analysis for the Magnetic Property Measurement System

Abstract 4.1 The process for analyzing the TMRX data obtained with the MPMS is briefly introduced. A typical TMRX spectrum comprises a series of MRX measurements. Therefore, in the first step, these single relaxation measurements must be processed. The uncertainty in the measurements is then determined and a curve–fitting process is used. As the TMRX measurements with the MPMS take up to 12 h, an alternative magnetizing procedure is implemented and investigated to determine if faster TMRX analyses are feasible. In order to implement the alternative magnetizing procedure different methods for controlling and accelerating the MPMS analyses are also discussed (Section 4.1.4). ■

4.1.1 Uncertainty of the Measurement Results

The MPMS output file for an RSO measurement (see also Chapter 8.1) is an ASCII table that contains, among other things, information about the measurement time, field, temperature, and the measured magnetic moment. An important value for each RSO measurement is the fit quality. This value shows how well the measured SQUID response (see Figure 4.1) fits a previously defined response curve that represents the signal of an ideal point–like source. The quality of the fit is given as a value between 1 and 0, with 1 representing a very good match and 0 representing a failed fit. A lower fit quality results in a higher uncertainty for the sample's determined magnetic moment.

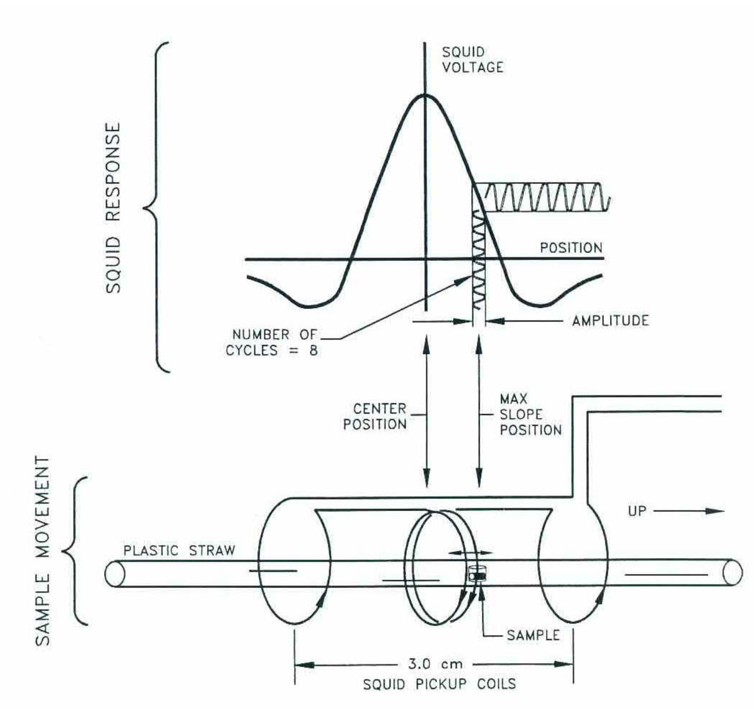

Figure 4.1: In RSO mode the sample is periodically moved through a second order gradiometer. The SQUID response depends on the sample position within the gradiometer (Picture from Manual [1]). The samples magnetic moment and fit quality are determined through comparison of the SQUID response with a previously defined response curve of a reference sample.

As described in Section 3.2.5, a relaxation measurement obtained using an MPMS consists of 100 single RSO measurements, each of which provides a value for the net magnetic moment of the sample. In this work the accuracy of these RSO measurements was investigated. To determine the influence of a low fit quality on the accuracy, the magnetic moment of an MNP sample was analyzed using different magnetic fields. When the field was sufficiently strong ($B > 10$ mT), a fit quality greater than 0.9 was obtained. At lower applied fields the fit quality decreased and the uncertainty of the determined magnetic moment increased. The relative magnetic moments and their corresponding fit quality are displayed in Figure 4.2.

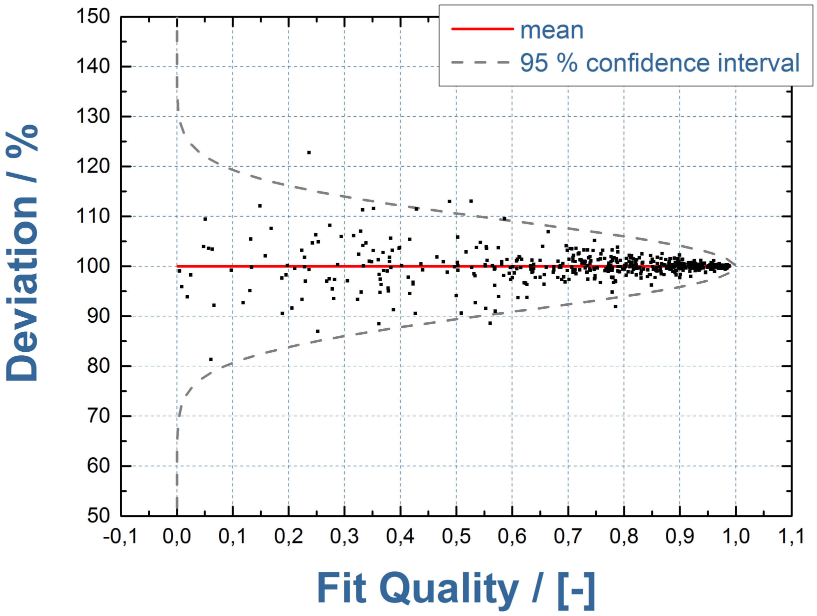

Figure 4.2: Relative magnetic moments of different RSO measurements and their corresponding fit qualities. A lower fit quality resulted in a decreased accuracy for a given magnetic moment. A confidence interval of 95% was obtained.

Using these results, a phenomenological function (f_{err}) for the confidence interval was generated in the course of this dissertation. A determined magnetic moment with a certain fit quality g_{fit} is covered by this interval in 95% of cases:

$$f_{err} = 1 - \frac{\sqrt{-ln(g_{fit} * \sqrt{2*\pi*0.4^2})2*0.4^2}}{6.6}. \tag{4.1}$$

This confidence interval was then used to determine the uncertainty of each RSO measurement in a magnetic relaxation scan (Figure 4.3, left frame).

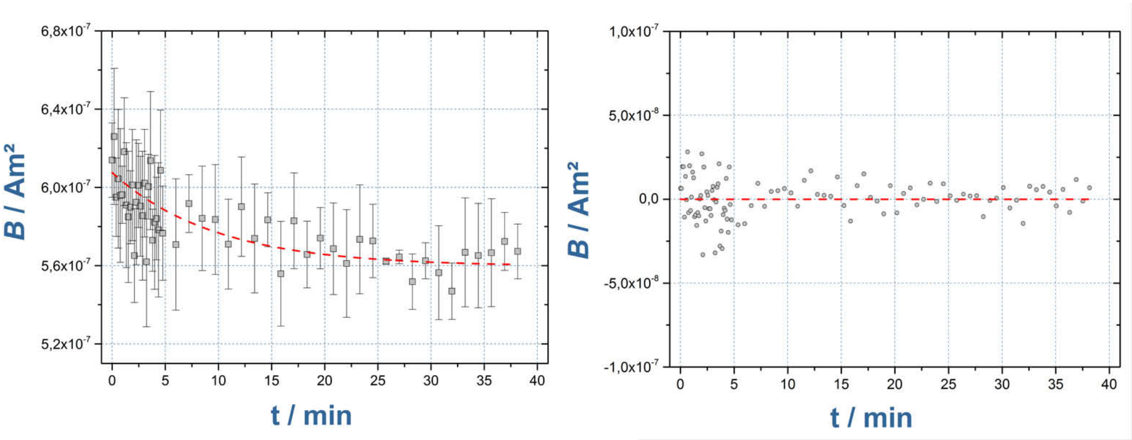

Figure 4.3: Left: Exponential least squares fit (red line) of relaxation measurements, each consisting of 100 single RSO scans. The RSO measurements in the first five minutes experienced more variation because they only consisted of single RSO scans while the latter scans were repeated three times. Right: Residual of the fitted exponential function. The upper maximum deviation from the fit was approximately $\pm 3 \cdot 10^{-8}$ Am^2

4.1.2 Fitting the Exponential Decay of the Measured Relaxation Signal

The relaxation measurements obtained using the MPMS comprised up to 100 single RSO measurements. For TMRX analyses, the amplitude change for each single relaxation curve had to be determined for a constant time window. For TMRX analyses using the MPMS, a time window of 40 min was used in this work. It was essential that this time window remained constant for all the relaxation measurements in order to be able to compare the different amplitudes. However, because of deviations in the switch–off time, the start time for the first RSO measurement varied slightly. It was therefore useful to compare the different relaxations over the time period from $t_{begin} = 1{,}5$ min to $t_{end} = 40$ min. In order to determine the net magnetic moment at $t_{begin} = 1{,}5$ min an exponential decay function was fitted to the relaxation data.

As described earlier in Section 3.2.5, during the first 5 min, the MPMS only performed single RSO scans and later switched to RSO scans with three repetitions. The first RSO scans therefore tended to have higher measurement uncertainties than the RSO scans with three repetitions. Therefore, the measurement quality was also taken into account in the form of a weighted least squares fit using weight matrix **W**, as shown in Equation 4.2. The obtained RSO data was inserted in vector **X** while the exponential fitting function was $\mathbf{Y} = A\exp(-t/\tau_\alpha)$, with A and τ_α as free fitting parameters:

$$\mathbf{P}_{Fit} = (\mathbf{X}^T\mathbf{W}\mathbf{X})^{-1}\mathbf{X}^T\mathbf{W}\mathbf{Y}. \tag{4.2}$$

Because of the weighting factors, data points with low fit qualities influenced the relaxation fit less than the data points with high accuracies. In addition, an option to remove outliers based on their measurement quality was included. When performing the data analysis a threshold for the fit quality could be chosen so that RSO measurements below that value (e.g. fit quality < 0.2) would be excluded. In Figure 4.3 (left frame), a fitted relaxation curve and the corresponding RSO data points with individual error bars are shown.

Finally, the fitted relaxation curve was subtracted from the original data points in order to determine the residual. The maxima of the residual (Figure 4.3, right frame) were then used to determine the upper and lower limits of the error bars for the amplitude changes. In a typical TMRX graph, the amplitude changes with their associated error bars are displayed as a function of temperature (Figure 4.4). The TMRX spectrum of a highly diluted MNP sample ($m_{Fe} = 0{,}2$ µg) is shown in Figure 4.4. The error bars are therefore particularly large.

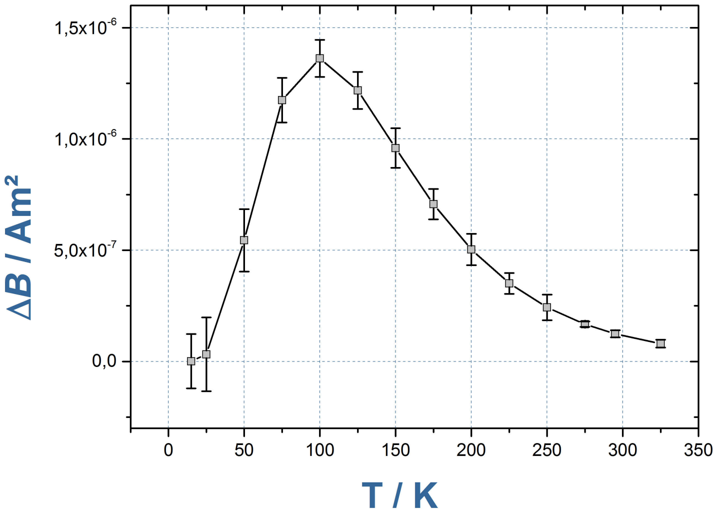

Figure 4.4: TMRX graph with error bars determined from the residuals of the fitted relaxation curves. The error bars are more or less pronounced depending on the signal strength at each temperature. The fit quality varied from a good average of 0.8 at room temperature to a low quality of 0.2 below 100 K.

4.1.3 Analysis of the Switch-Off Time of the Superconducting Magnet

The switch–off time of the superconducting magnet is an important factor for determining the measurement uncertainty. As described in Section 8.1 of the Appendix, the persistent–current switch must be heated prior to changing of the current in the coil. Because of the increase in temperature, a small portion of the circuit loses its superconductivity, and the current in the coil is reduced. If the magnet is in *persistent* mode, the magnitude of the power supply's current must be matched with the current flowing in the magnet. The higher the active current in the coil, the more time this process takes. Furthermore, if the current in the superconducting coil is changed, a current is also generated in the detection coil via induction. To prevent the detection coil from charging, a small section of this coil is also heated.

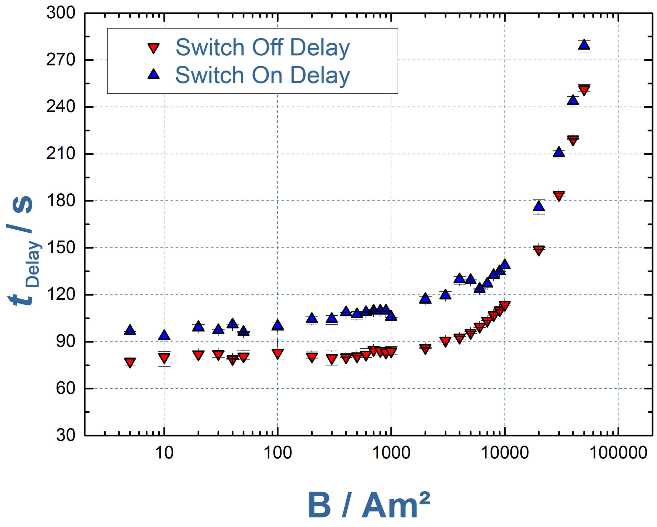

Figure 4.5: Switch–off and switch–on times of the MPMS superconducting magnet for set fields ranging from 0,1 mT to 5 T.

In order to switch the magnet back on, the persistent switch must be heated to induce a current in a similar manner. Using the attached current source on the switch, a current can be brought into the superconducting magnet. After setting the required field, the switch must then be cooled again in order to achieve *persistent* mode; because an active switch would increase the noise level. A side effect of the magnetization of the coil is the so–called *flux creep*, a relaxation effect of the magnetic field in the system. This effect causes a slight field change in the superconducting magnet, which again induces a current in the detection coil and therefore leads to a SQUID drift. While the linear portion of the SQUID drift is compensated by the MPMS control system, the non-linear portion cannot be compensated. A short delay is thus added after the field has been changed. For higher magnetic fields, the flux creep is more pronounced, and hence the wait time is longer. This field dependency can be seen in Figure 4.5. The average switch–off time for fields below 1 T is approximately 75 s. For fields above 1 T, the delay increases exponentially up to 250 s. The switch–on time is approximately 20 s to 30 s longer than the switch–off time for all changed fields. Based on this data, the relaxation measurements performed in the present study were executed with fields ranging from 1 mT to 10 mT because the switch–off times of these fields are fairly short.

4.1.4 Communication with a Magnetic Property Measurement System

In general, communication with the MPMS is achieved via the sequence manager of the MultiVu software (see also 8.1). However, other more direct forms of communication with the MPMS are also possible. The command–system in the background of the MultiVu software is the EDC language (see also Section 8.1). While single EDC commands can be sent directly via the MultiVu software, an additional (script-)language is needed to perform a sequence of measurements. In order to avoid the switch–off time of the MPMS, magnetization of the sample was attempted using the AC–coil in the system, rather than the superconducting magnet. This normal conducting coil is designed to perform AC measurements in the MPMS. Even though the maximum generated field of the coil is only 0,1 mT, it would be sufficient to magnetize a sample for TMRX analysis. Because the sequence manager of the MultiVu software does not include a DC setting for this coil, its activation was achieved using EDC commands that were initially sent directly over a LabVIEW interface. For the communication via LabVIEW, the GPIB port of the MPMS was utilized. The GPIB port enables a user to send any three–letter EDC command string to a specific address in the MPMS (e.g., the RSO–motor). Ultimately, the EDC commands were sent via a Delfi script because the LabVIEW interface was found to be insufficient for the intended task.

LabVIEW

In order to send direct EDC commands to the MPMS, LabVIEW software from National Instruments was utilized. This software was installed on a second computer connected to the MPMS over a USB to a GPIB cable. When operating in general mode, the MultiVu software frequently sends EDC commands to check the status of the system. If one of those EDC commands is sent at the same time as one of the EDC commands from LabVIEW, complications with the MPMS may occur. Thus, although running LabVIEW and MultiVu at the same time is possible, it is not recommended. The main part of the LabVIEW program consists of predefined EDC command strings. These strings include specific tasks that are required for the TMRX sequence, i.e., temperature and field settings. As is the case for the MultiVu software, there are also frequently repeating EDC commands in the LabVIEW program, such as the temperature read-out and a vigilance command for the MPMS to confirm that the operating PC is still operational. If this vigilance command is not received by the MPMS regularly, the system shuts down in safe mode. Eventually, a stable LabVIEW communication system for sending direct commands to the MPMS was developed. However, complete replacement of the MultiVu software with the modified LabVIEW program suffered from complications because of the need for replacement frequent background EDC commands from the MultiVu software. Even though long delays between the single EDC commands were included, the MPMS missed some commands, and as a result the entire communication system was unreliable. The decision was thus made to halt work on the LabVIEW–based communication system and switch to the Delfi script expansion package.

Delfi

The Delfi expansion package was offered as an add-on to the existing Multivu software. It proved more reliable than LabVIEW–based communication. The script expansion package enabled the inclusion and execution of user designed EDC–based scripts via the MultiVu sequence manager. Use of the MultiVu software in combination with written Delfi scripts was advantageous compared to the LabVIEW communication approach because it was not necessary to replace the entire MultiVu system; Delfi scrips were only required for the new program elements. The new commands included in particular, use of the AC coil for DC magnetization. Ordinary tasks such as temperature settings were retained in the MultiVu sequence manager. Quantum Design offered various example scripts for their Delfi expansion package, which was an added perk. Using these examples, the AC coil in the MPMS was successfully utilized for DC magnetization of the sample space. In contrast to the large superconducting magnet, the AC coil in the MPMS is not superconducting and can only generate very small fields of 0,1 mT. However, the AC coil has a very short switch–off time of less than a second. Consequently, a single RSO measurement takes a long time, which is a limiting factor when using the MPMS for fast TMRX analyses. Thus, although the switch–off time with the AC coil was set to less than a second, the first RSO measurement point still took 30 s, eliminating the time gain that was achieved by using the AC coil. A second attempt to accelerate the analysis was then made by directly reading the MPMS SQUID signal. The read-out was realized over the J-C10 serial–port on the rear side of the MPMS using a digital storage oscilloscope (Agilent Technologies, DSO-X 2004A). Unfortunately, the oscilloscope measurements revealed a strong drift in the first 30 s, even without a sample. This background signal exceeded the relaxation signal of a typical MNP sample by a factor of 100. Therefore, the AC coil not only magnetized the MNP sample but also parts of the MPMS sample chamber. The background signal is most likely because of magnetization of the superconducting magnet and the pickup coil and additional flux creep. In ordinary RSO measurements, the long wait time and offset corrections adjust for this background relaxation so that it does not interfere with the analyses. In addition, use of RSO measurements in combination with the AC coil would still result in a delay of approximately 5 s because of the RSO measurement time. In combination with the small magnetization field of 0,1 mT, this delay would result in a severe signal loss.

It was therefore not possible to significantly accelerate the relaxation analyses using the MPMS. Hence, the development of a custom TMRX device looked more promising.

Conclusion

In the first part of this chapter an analysis method for relaxation data obtained with the MPMS was introduced. In order to consistently determine the relaxation amplitude change an exponential curve was fitted via least squares. The measurement quality value of standard RSO data files was used to create a weighted exponential fit and further optimize the fit accuracy. In addition, the residue of each relaxation curve could be determined by subtracting the exponential fit. The residue was then displayed as error bars in a typical TMRX plot.

In the second part an alternative magnetizing procedure was implemented in the MPMS with the intention of accelerating the TMRX measurement procedure. In order to do so an AC coil in the MPMS had to be utilized for DC magnetization of the sample. This could be achieved by sending direct commands to the MPMS via a LabView or Delfi interface. However, it turned out that a significant acceleration was not possible with the MPMS because of interfering background relaxation signals which are probably caused by flux creep. This led to the decision to design a custom measurement system for faster TMRX measurements which is explained in detail in chapter 6.

4.2 Influence of Magnetic Nanoparticle Amount on the TMRX Spectrum

Abstract 4.2 In this chapter the influence of the total amount of magnetic nanoparticle on the TMRX signal is discussed. To do so, a dilution series of very small non–interacting particles with known iron content was investigated. In the course of this thesis a novel MNP quantification method was developed based on the correlation between the TMRX amplitude and the total amount of magnetic iron in the sample. The quantification of MNPs in tissue or cell samples plays an important role for different biomedical applications of MNPs. To demonstrate the applicability of the introduced MNP quantification method, the MNP uptake in two different cancer cell lines was determined.[a] ■

---

[a] The content of this chapter was published in 2013 [43]

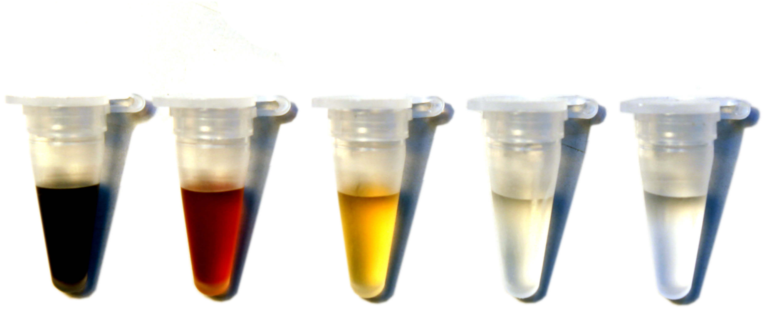

Figure 4.6: Dilution series of the CD021110 magnetic nanoparticle solution in PCR tubes.

Investigated Particles

Feraheme® is a commercial drug product with the active drug substance ferumoxytol (AMAG Pharmaceuticals Inc., formerly Code 7228). Feraheme® is indicated for the treatment of iron deficiency anemia [86]. It is also being developed as a diagnostic agent for first–pass contrast–enhanced magnetic resonance angiography to assess peripheral arterial disease [49]. The iron oxide Feraheme® is surrounded by a carbohydrate coating composed of polyglucose sorbitol carboxymethyl ether.

CD021110 consists of carboxydextran–coated superparamagnetic iron oxide particles for pre-clinical use and synthesized based on patent US 5,424,419.

Preparation of Dilution Series Samples

In this work a dilution series of immobilized reference samples of the CD021110 MNP solution was prepared using an automated pipetting robot (epMotion 5070, Eppendorf). Each subsequent dilution step involved dilution with aqua dest. by a factor of three, starting with the original MNP suspension (iron concentration = 0,1 mol/L). A mannitol solution containing 15 % mannitol was then added to each dilution, and the resultant MNP solutions were stabilized in polycarbonate capsules via freeze drying to obtain immobilized samples. Thus, the nominal iron content in the dilution series varied from several micrograms (1:3) to a few nanograms (1:2187) (see also Table 4.1).

TMRX Measurement Procedure

The analyses were performed using a Quantum Design SQUID magnetometer (MPMS) via RSO measurement following the procedure described in Chapter 3.2.5.

4.2.1 Analysis of a Magnetic Nanoparticle Dilution Series

In a first step, the relaxation of the magnetic moment for the CD021110–nanoparticle preparation was recorded at various temperatures (see Figure 4.7). For a better graphical representation, the magnetic moment obtained at the end of each recording period was subtracted from the relaxation curve such that the last data points coincided for each temperature. In addition, only 10 out of 17 relaxation curves are displayed. The magnetic moment of each RSO scan is represented as a single data point. Two different measurement modalities of the MPMS SQUID magnetometer were used in a single relaxation measurement: the single RSO scan and three RSO scan average. The single RSO scan offers a faster determination of the magnetic moment at the price of a higher measurement uncertainty compared to that of the three RSO scan average. Hence, during the first 7 min of the analysis, when the relaxation signal was strongest, the single scan technique was used. Averaging of three scans was subsequently employed for the remainder of each analysis.

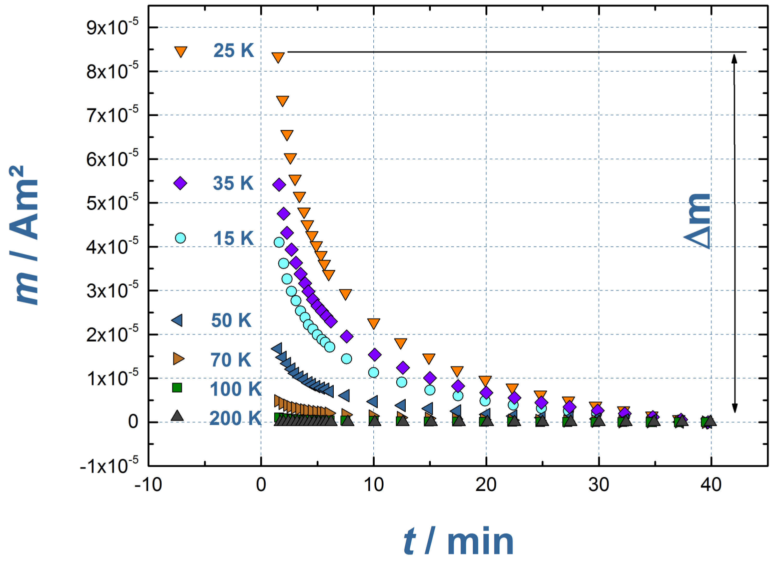

Figure 4.7: Relaxation curves for the CD021110 solution at different temperatures (10 of 17 curves are displayed). In the first 7 minutes, each data point was determined from a single RSO scan while the subsequent points obtained by averaging 3 RSO scans.

For MNP signals within the time window Δt=1,5 min–40 min typical relaxation behavior was observed, i.e., the magnetic moments decayed in curves described as stretched exponentials. While the relaxation curve amplitudes varied considerably with temperature, the shapes of these curves remained identical within the measurement uncertainty. Above 200 K, no magnetization signal was detected; a measurable relaxation amplitude within this window appeared only below 100 K. When displaying only the amplitude change (Δm) at each temperature, the amplitude increased dramatically as the temperatures decreased and reached a maximum at approximately 20 K (see Figure 4.8).

At room temperature, virtually all of the particles in the MNP distribution were too small to generate a relaxation signal within the measurement time window. When the maximum was observed, the majority of the particles relaxed within the measurement time window while at lower temperatures, the amplitude decreased again because increasing numbers of particles relaxed too slowly to be detected in the constant time window.

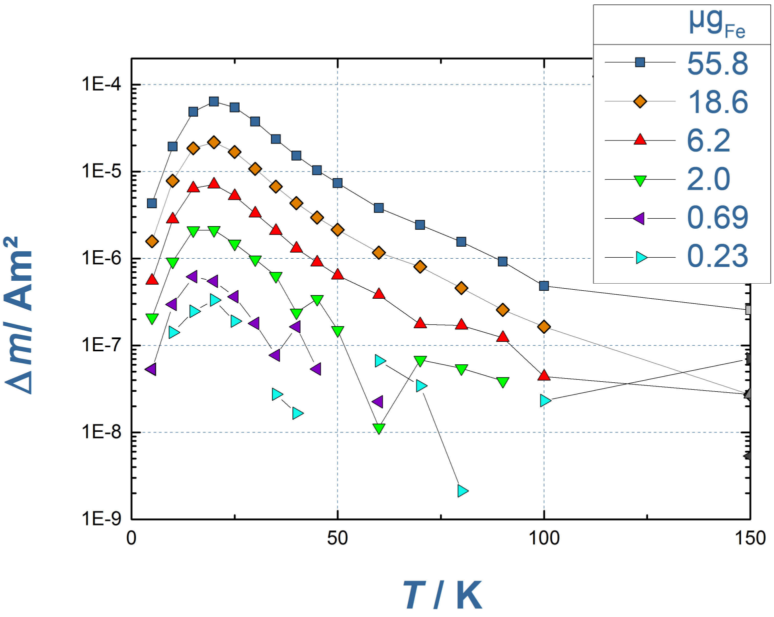

Figure 4.8: TMRX spectra of the different CD021110 dilution samples. The amplitude change (Δm) of each relaxation curve is displayed at the measured temperature. The maximum amplitude for each sample was observed at approximately 20 K. The detection limit for this dilution series was determined with approximately $5 \cdot 10^{-8}$ Am^2. Due to the logarithmic display negative data points are not shown. At temperatures above 200 K no relaxation was observed within the measurement time window.

In Figure 4.8, the amplitude change (Δm) is displayed as a function of temperature for the different dilution samples. The iron amount in these samples varied from 55,8 µg to 0,23 µg. Interestingly, it can be seen in Figure 4.8 that each TMRX spectrum had the same peak temperature at approximately 20 K, and all of the spectra had a similar shape. However, it can be clearly seen that the amplitude change scaled with the iron content, implying that for this dilution series, the Néel relaxation time (τ_N) was not affected by the amount, and only the amplitude (A) of the magnetic moment changed:

$$M(t) = A \cdot exp\left(-\frac{t}{\tau_N}\right) \tag{4.3}$$

These findings revealed that the amplitude at the peak temperature could be correlated to the known total iron content.

4.2.2 Quantification of the Iron Content via *Peak Comparison*

In order to use TMRX analysis for quantification, the measured amplitude change must be correlated to the iron content in the sample. For the CD021110 samples, the nominal iron contents were

Dilution Step	Nominal Iron μg_{Fe}	Quantified iron μg_{Fe}
1/3	55.8	54.6
1/9	18.6	54.6
1/27	6.2	5.2
1/81	2.0	1.4
1/243	0.69	0.36
1/729	0.23	0.19

Table 4.1: Iron amount in CD021110 dilution series.

determined via M(H) analyses performed using the MPMS. A linear relationship was revealed by comparing the amplitudes at the peak temperature with the known iron contents in the samples. All of the TMRX spectra exhibited maximum amplitudes near the same peak temperature (T_{max}, approximately 20 K). The linear correlation between the amplitude change (Δm) and the nominal iron content is displayed in Figure 4.9. For this type of MNP analysis, the detection limit was estimated to be approximately 250 ng iron.

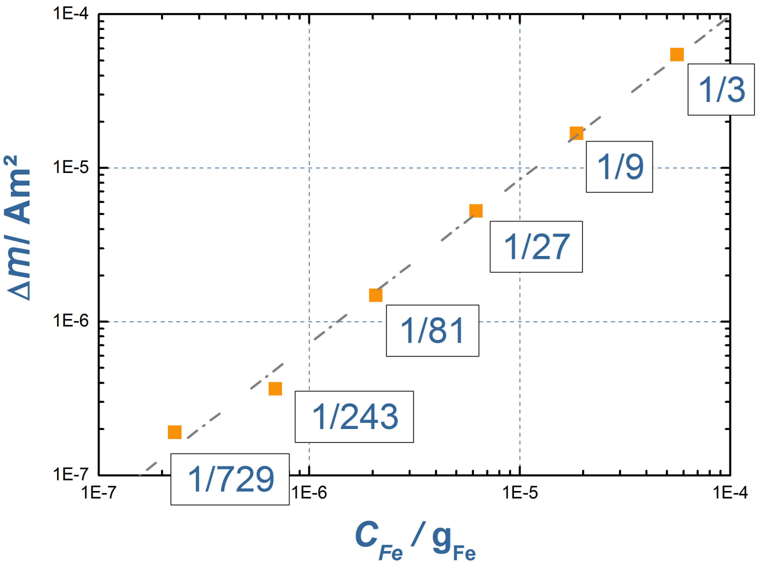

[H]

Figure 4.9: Total Iron Contents in the CD021110 dilution samples versus their relaxation amplitudes (Δm) at their peak temperatures.

Because a linear correlation between the total iron content and amplitude at the peak temperature was demonstrated, the new method was applied to *in vitro* quantification.

4.2.3 Analysis of Magnetic Nanoparticles in Cell Samples

For this *in vitro* experiment, HeLa and Jurkat tumor cell lines were incubated by colleagues at the Charité [1] using Feraheme® and CD021110 iron oxide MNPs. After 30 h, approximately 10^6 cells of each type were harvested. The cell samples were incubated with different quantities of CD021110 or Feraheme®. As a control, one cell sample was incubated without exposure to an MNP solution. In Figure 4.10, the relaxation amplitudes (Δm) of the initial MNP solutions are plotted as a function of temperature. The different shapes of the two TMRX spectral curves reflect the different size distributions of the two MNP systems. The maximum amplitude for CD021110 occurred at a slightly higher peak temperature than that for Feraheme®. This result is attributed to the different core diameters of the particles. These observations illustrated that TMRX spectral shapes can be utilized to characterize the magnetic properties of MNP preparations, and, in particular, to identify changes in the particle size distribution.

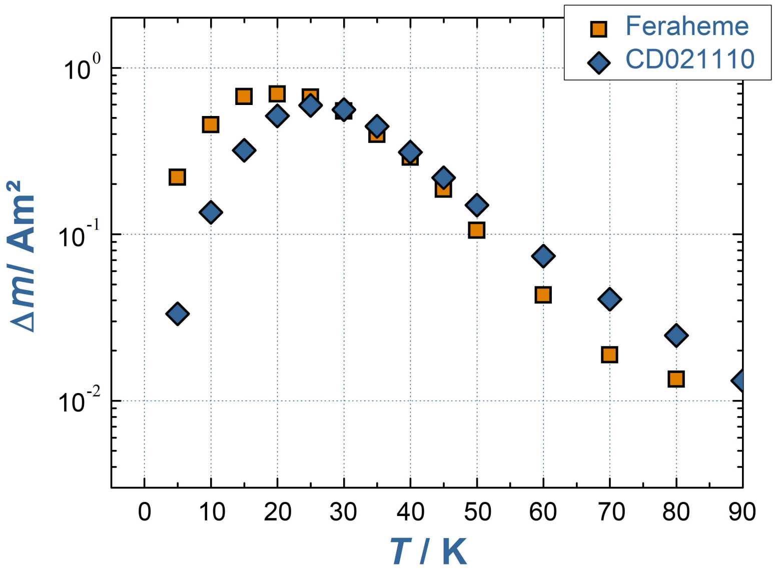

Figure 4.10: Relaxation amplitude (Δm) as a function of temperature for CD021110 and Feraheme®. Even small differences in the particle characteristics resulted in noticeable changes in the relaxation amplitude curves.

In addition, the MNP specificity of the relaxation curves was be illustrated using the control data obtained for the cell sample that was not exposed to MNPs, as shown in Figure 4.11. Absolute magnetic background moments of approximately 0,3 μAm^2 were determined for a tissue sample without MNPs using single and averaged RSO scans, respectively.

---

[1] Ines Gemeinhardt, Monika Ebert, Jörg Schnorr, Susanne Wagner, Matthias Taupitz

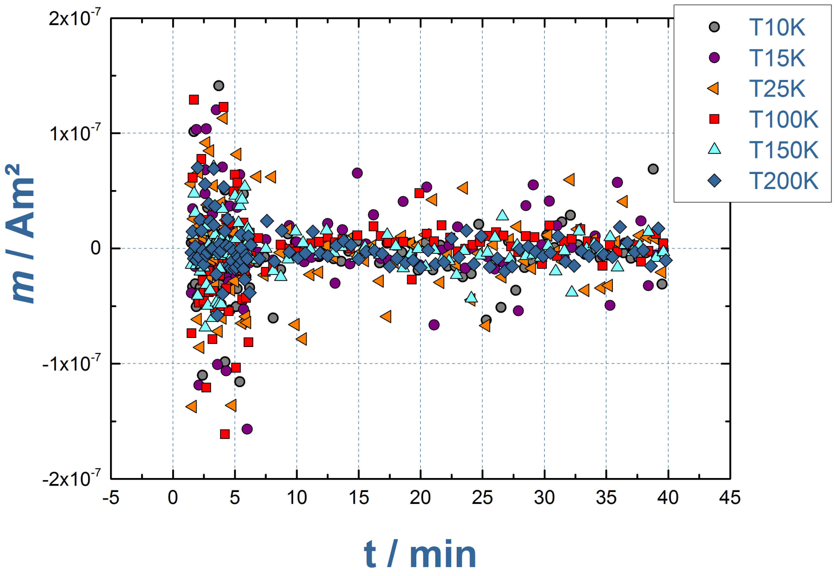

Figure 4.11: MRX analysis of the control sample. No relaxation was observed. The background signal was 0,3 µAm^2 for the first 7 min of detection and, then decreased to approximately 0,1 µAm^2 because of the change in the number of averaged RSO measurements.

Subsequently, TMRX analyses of the different incubated cell samples were performed. Figure 4.12 presents the TMRX spectra of HeLa cell samples with low and high MNP concentration and a CD021110 reference sample (m_{Fe} = 55,84 µg). Using a reference sample with known iron amount, it was possibleto apply the peak comparison method for quantification of the cell samples.

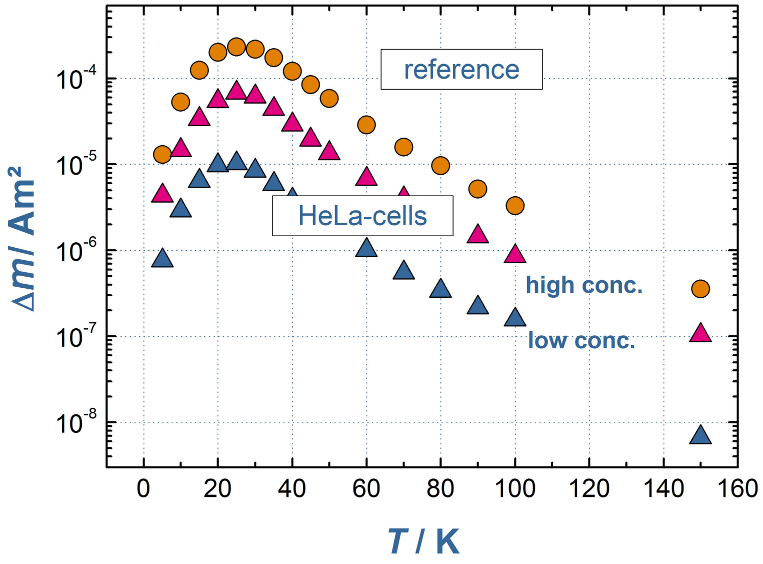

Figure 4.12: Temperature dependent magnetorelaxometry spectra for HeLa tumor cell lines and the initial CD021110-MNP solution as a reference. The TMRX spectra indicate that the MNP signals mainly differed in their relaxation signal strengths. The shapes of the curves remained the same for the incubated and non–incubated MNP samples.

Again, all of the spectra exhibited a similar shape, and their maxima occured roughly at the same peak temperature (T_{max}). Although the amplitudes of the peaks in the spectra of the tumor cell

Name	Exposure	M(H)μg_{Fe}	TMRX μg_{Fe}
Hela-5	Low	15(1)	16(1)
Hela-8	High	111(5)	107(6)
Jurkat 16	Low	15(1)	13(1)
Jurkat 18	High	178(9)	177(10)

Table 4.2: Iron amount in CD021110–exposed tumor cells.

lines were considerably reduced, they remained above the detection limit. Without additional MNP interaction, the relaxation moment is directly proportional to the iron content. Therefore, the iron content of the cell samples was determined from the ratio of the peak amplitude in the reference MNP solution spectrum and the amplitudes at the peak temperature in the spectra of the cell samples. The results for the dilution series and control indicated an accuracy of approximately 250 ng for the CD021110 particles and the current setup. The last sample of the mannitol dilution series that could be analyzed had a total iron content of 200 ng. A slight shift in T_{max} and very small but systematic deviations in the shape of Δm were be noticed in the spectra of the HeLa (Fig. 4.12) and Jurkat cell samples. These results may be because of areas of high, local MNP concentrations in the cell samples that altered the relaxation behavior with respect to the reference sample via dipole–dipole interactions [24]. The shift in the relaxation amplitude curve may also be attributed to size–selective MNP uptake. Shifts in the peak temperature of up to 10 % were also observed and resulted in a quantification uncertainty of approximately 6 %. These two phenomena have also been shown to influence other properties, such as the M(H) signal, by several percent [25]. The M(H) measurement uncertainty was estimated to be approximately 5 %. Hence, both methods provide similar results within the limits of uncertainty.

Conclusion

In this chapter a dilution series of non-interaction MNPs were analyzed via TMRX in order to investigate the influence of the MNP amount on the relaxation signal. The measurements revealed a linear correlation of the total particle amount to the peak amplitude of the TMRX curves. The method was furthermore used to successfully quantify the MNP uptake in HeLa and Jurkat tumor cell lines. The determined iron contents were in accordance with other established quantification methods. In addition, it was shown that it is possible to distinguish different MNP types based on their TMRX spectra. The measurements performed in the course of this thesis therefore expanded the field of application of the TMRX method.

4.3 Influence of the Magnetizing Field Strength on the TMRX Spectrum

Abstract 4.3 The influence of the magnetization field on the TMRX signal was investigated. A *DDM 128* sample was evaluated at magnetization field strengths of 1 mT, 10 mT, 50 mT and 100 mT. DDM 128 is a precursor of the contrast agent Resovist and, like Resovist, is bimodally distributed. Because of the size dependence of the saturation magnetization, the field strength affected the particles in the distribution differently depending on their core sizes. Variation of the magnetization field strength was found to be a facile method for visualizing the dispersity of a particle system, i.e., to determine whether the particle core sizes are more mono- or polydisperse. ■

Investigated Particles

MNPs of the precursor of Resovist (Bayer Schering Pharma AG) were investigated. Resovist is a commercial contrast agent for MRI that is used to detect malign liver tumors. The contrast agent consists of superparamagnetic iron oxide nanoparticles (SPION) coated with carboxydextran. Resovist and its precursor particles are known to have bimodal size distributions with particle core diameters ranging from 8 nm to 26 nm [90][23].

Preparation of Dilution Series Samples

The highly concentrated original DDM 128 solution (500 mmol) was diluted to create a solution with a defined iron content. Specifically, the original solution was diluted with distilled water in order to achieve an iron concentration of 1 mol/L which was assumed to be sufficiently dilute to prevent particle interaction. A 15 % mannitol solution was then added to 30 µL of the dilute MNP solution, which was then immobilized in a polycarbonate capsule via freeze drying.

TMRX Measurement Procedure

The measurements were performed using a Quantum Design SQUID magnetometer (MPMS-XL) with RSO measurements following the previously described procedure (3.2.5). In order to investigate the influence of the field strength, the TMRX sequence was performed using a magnetization field strengths of 1 mT, 10 mT, 50 mT and 100 mT. The switch–off time of the magnetization field varied for the different fields from approximately 1,3 min to 1,5 min (see 4.1.3), and was therefore considered constant. Both the magnetization and the measurement times were left unchanged.

4.3.1 Magnetizing Field Strength dependent Changes in the Relaxation Signal

TMRX analysis was first performed using the diluted DDM 128 sample. The same sample was measured repeatedly using TMRX sequences with different magnetization field strengths, and the absolute relaxation amplitude change (Δm) is plotted as a function of T in Figure 4.13. When $B_{Mag} = 1\,\mathrm{mT}$, two distinct peaks were observed in the TMRX spectrum at 15 K and approximately 150 K. The peaks differed in both width and absolute height, or signal strength with the 150 K peak nearly twice as high as the 15 K peak.

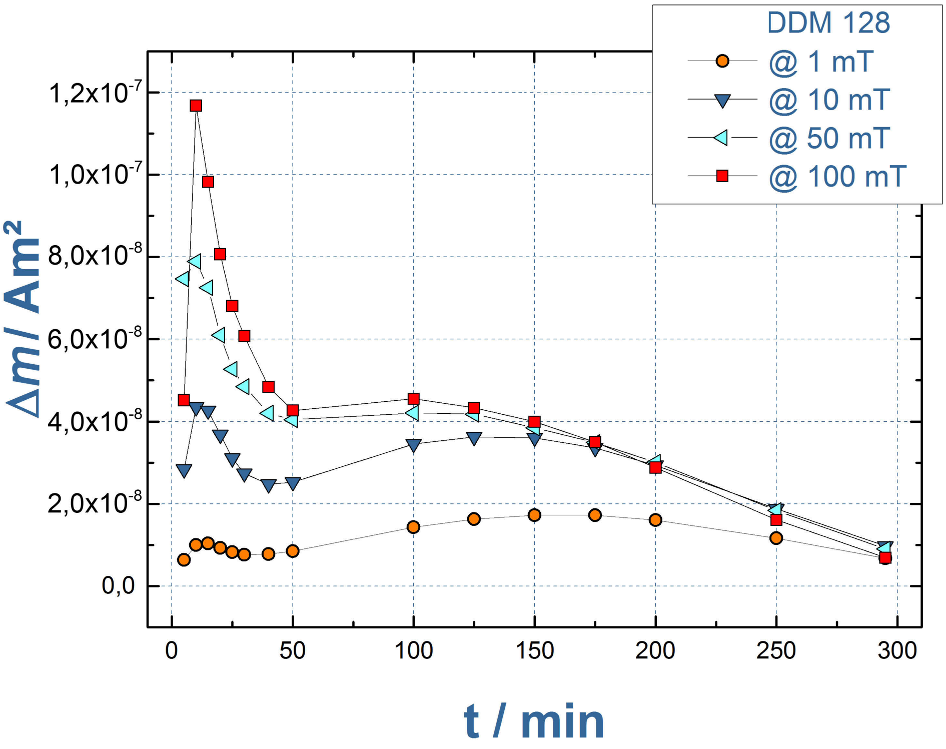

Figure 4.13: TMRX signals for the Resovist precursor DDM 128 at different magnetization field strengths. The TMRX signal for DDM 128 exhibited two distinct peaks at 15 K and 150 K that were attributed to the bimodal distribution of the particle core size. Changes in the field strength had varying impacts on the particles of different sizes. The larger particles were less affected by higher field strengths because they were already saturated.

When $B_{Mag} = 10\,\mathrm{mT}$, the TMRX signal increased at all temperatures, and the two peaks became even more pronounced. In addition, while the temperatures at which the peaks occurred remained nearly unchanged, the ratio of the intensities of the two maxima was drastically altered with the 15 K peak exhibiting a similar relaxation amplitude to that of the 150 K peak. This trend continued for the 50 mT and 100 mT measurements. The change from 50 mT to 100 mT had a significant effect on the amplitude of the 15 K peak but negligible effect on the 150 K peak. A slight shift in the 150 K peak to lower temperatures also occurred at higher magnetization field strengths; at 100 mT, the second peak was observed at 100 K rather than 150 K.

It is known from previous studies [90][23] that Resovist and its precursor DDM 128 have a bimodal size distribution, i.e., there is a small fraction with core diameters of approximately 5 nm and a large fraction with core diameters ranging from 15 nm to 20 nm. The two distinct peaks seen in Figure 4.13 are attributed to these two size distributions within the MNP sample. As described in Chapter 3.2.3, the two magnetic core volumes have different relaxation times and corresponding energy barriers. Hence, their relaxation amplitude changes peak at different temperatures.

Using the Langevin equation (Equation 2.2), the magnetization behavior of the differently sized

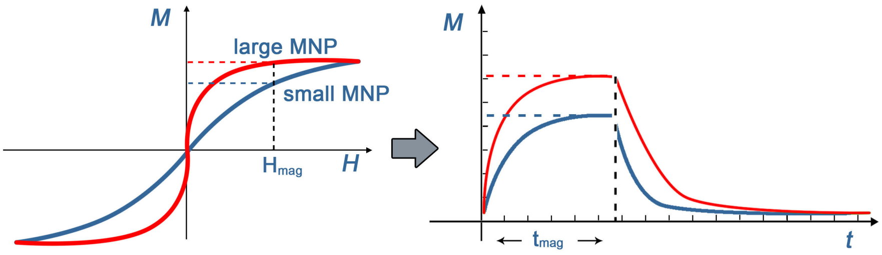

Figure 4.14: Left: Magnetization curves for small (blue line) and large (red line) superpara–magnetic particles. The larger MNPs exhibited a steeper slope than the smaller particles. Right: Magnetization and relaxation processes during an MRX procedure. The larger particles required a lower magnetization field strength to reach their saturation magnetization. Therefore, the larger particles were less magnetized than their smaller counterparts when exposed to the same magnetic field H_{mag}. This leading to a smaller amplitude change during the relaxation process.

particles can be visualized. In Figure 4.14, the idealized magnetization curves for the small and large particles are displayed on the left. These magnetization curves illustrate, that the larger particles require a lower magnetization field strength (H) to reach saturation magnetization, which directly affects the relaxation process (Figure 4.14, right) and leads to different relaxation amplitude changes for the differently sized particles.

Therefore, when H increased from 1 mT to 10 mT, both particle distributions within the sample increased their magnetic moments. However, when the field strength was increased further to 50 mT and 100 mT, the fraction of larger particles reached saturation, whereas the signal strength of the smaller particles continued to grow. The saturation effect for the large particles also explains the temperature shift for the relaxation peak from 150 K to 100 K as the magnetization field increased. The fraction of larger particles itself consisted of log-normal distributed (2.1.3) smaller and larger particles. The change in the magnetization field affected these diverse MNPs differently. While the larger particles within the log-normal distribution were already saturated, the smaller continue to experience gains in their magnetic moments. As a result the peak for the entire fraction of larger particles shifted to lower temperatures.

Finally, the question remained as to why the maximum amplitude change for the fraction of smaller particles at 15 K was nearly three times as pronounced as the maximum amplitude change for the fraction of larger particles at 100 mT. As introduced in Chapter 4.2, the amplitude change is linearly dependent on the MNP concentration. The different pronounced peaks can therefore be attributed to the total quantities of small and large MNPs in the sample. However, to determine the nominal MNP concentrations of the different fractions, a reference sample with known quantities of each fraction is needed.

Conclusion

The performed experiment can be used to visualize the dispersity of a particle distribution. For the DDM 128 sample, the fraction of smaller particles with a peak at 15 K appeared to be much less affected in terms of peak-shifting. This result indicated that this fraction was actually monodisperse. The peak shift of the fraction of larger particles, in contrast, indicated a larger variance in the log-normal distribution of the particle core diameters. In addition, the field dependence can be used to determine the ratio of two fractions within one sample. For exact determination of the nominal iron concentration, however, reference samples for each fraction are needed.

4.4 Influence of Particle Aggregation on the TMRX Spectrum

Abstract 4.4 The influence of particle interactions on the relaxation signal was investigated. In order to provoke dipole–dipole interactions, citrate–coated MNPs were deliberately aggregated via the addition of a sodium chloride solution. A stable dilution series of MNPs was prepared and subsequently aggregated. The magnetic properties of both the stable and aggregated solutions were then examined using temperature dependent magnetorelaxometry. The previously presented quantification method (Section 4.2) was employed in this case because the underlying interaction process was independent of the macroscopic concentration. [a] ■

---

[a] The content of this chapter was published in 2014 [42]

Figure 4.15: Left: 30µL of the original particle solution in distilled water. Right: Visible aggregation and sedimentation 30 min after addition of a sodium chloride solution (c_{NaCl} =1 mol/L).

Investigated Particles

For the quantification experiment, a solution of citrate–coated small iron oxide MNPs manufactured by Charite Berlin was used. Two dilution series of the original particle system ($c_{Fe} = 0.1\mathrm{mol/L}$) were prepared. One was prepared by diluting with distilled water, and the other by diluting with a sodium chloride solution (c_{NaCl} =1 mol/L) in order to force aggregation. The addition of sodium chloride led to visible aggregation after 30 min (see Figure 4.15). Subsequently, the samples were immobilized by freeze drying after addition of 30 µL mannitol (c_{mannit} =50 mmol/L) solution over night.

TMRX Measurement Procedure

The measurements were performed using a Quantum Design SQUID magnetometer (MPMS-XL) and RSO measurements as described in Section 3.2.5.

4.4.1 Influence of Dipole–Dipole Interactions on the TMRX Spectrum

For both the aggregated and unaggregated MNP samples, the peak temperature of the amplitude (T_{max}) was observed well below room temperature. Forced aggregation via the addition of sodium chloride led to a change in the shape of the relaxation curve. The peak temperature of the amplitude increased from 130 K for the unaggregated particles to 210 K for the aggregated system, as can be seen in Figure 4.16. This shift resulted from a change in the relaxation time (τ) for the aggregated particles, which required more time to fully relax than the unaggregated particles.

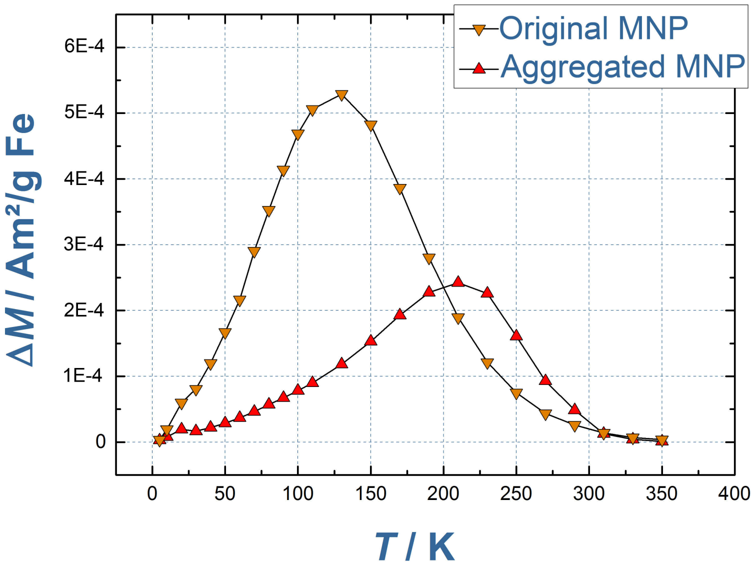

Figure 4.16: Changes in the TMRX signal through enforced aggregation. Both the stable and aggregated MNP samples exhibited relaxation signals at nearly every investigated temperature, with peak temperatures at 130 K and 210 K, respectively.

Investigation via TMRX revealed that each sample exhibited a broad relaxation spectrum, i.e., the samples displayed relaxation signals from 5 K to ambient temperature. This width can be explained by broad distributions of the magnetic core sizes within the samples. In addition, the small shoulder at 20 K in the spectra for both samples indicated the presence of a second smaller fraction of particles within the sample.

While aggregation led to an increase in the peak temperature of approximately 80 K, it affected the relaxation at temperatures other than the peak temperature significantly less, resulting in more of a stretched deformation of the curve to higher temperatures than an equal shift. In addition, comparison of the peak temperatures revealed an amplitude loss of more than 50 %, with a decrease in the overall amplitude per milligram iron. This change can be explained by an elongation of the Néel relaxation time (τ_N) because of the dipole–dipole interaction energy E, as in Equation 4.4:

$$\tau_N = \tau_0 \exp\left(\frac{KV}{k_B T} + E\right). \tag{4.4}$$

With a longer τ_N, relaxation of the aggregated particles at most temperatures was too long to be detected within the constant measurement window (t_{start} =1,5 min to t_{end} =40 min). However, aggregation did lead to an increase in the amplitude at temperatures ranging from 200 K to 310 K. In this temperature range, the particles relaxed very rapidly prior to aggregation and lost a portion of their relaxation amplitude in the first 1,5 min, i.e., prior to initiation of the measurement window started. Their relaxation behavior at these temperatures then slowed down because of aggregation, resulting in an increase in the relaxation amplitude.

Signal alterations at temperatures near 300 K are particularly relevant because nanoparticles for biomedical applications are applied at ambient temperatures. Signal changes caused by concentration effects, aggregation, and immobilization are therefore important for applications such as imaging and hyperthermia.

4.4.2 Quantification of Aggregated and Unaggregated Particles

TMRX analyses of the aggregated and unaggregated samples revealed that their curve shapes and maximum temperatures (Figure 4.17) did not change with concentration. These results indicated a constant relaxation time for each dilution series, which is contrary to previous results in which the peak temperature (T_{max}) was observed to scale with the concentration (see also Chapter 5.1) [106]. In addition, the decrease in amplitude was directly proportional to the nominal iron content within the samples, as can be seen in Figure 4.18.

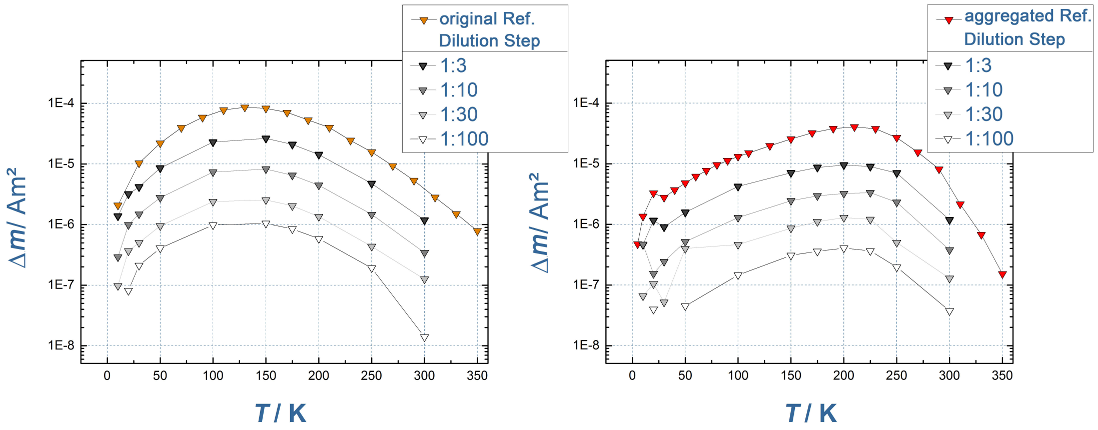

Figure 4.17: TMRX signals of original (left) and aggregated (right) particles at different concentrations. The overall amplitude declined with increasing dilution. The peak temperatures at 130 K for the original and 210 K for the aggregated MNP samples remained unchanged for the different dilution steps.

Thus, the iron content of a sample may be determined via peak comparison (see also Chapter 4.2) using a known reference sample [43]. Quantification via TMRX peak comparison is, however, only reliable if the curve shapes of the TMRX spectra remain unchanged. The known reference sample must therefore have a similar TMRX spectrum as the sample to be quantified.

Dissolution	Total Iron Amount [g]	$\Delta m[Am^2]$ at $T_{Max} = 200K$
1	$6.9 \cdot 10^{-4}$	$3.93 \cdot 10^{-5}$
1 to 3	$2.3 \cdot 10^{-4}$	$9.53 \cdot 10^{-6}$
1 to 10	$6.9 \cdot 10^{-5}$	$3.22 \cdot 10^{-6}$
1 to 30	$2.3 \cdot 10^{-5}$	$1.29 \cdot 10^{-6}$
1 to 100	$6.9 \cdot 10^{-6}$	$4.06 \cdot 10^{-7}$
1 to 300	$2.3 \cdot 10^{-6}$	$1.56 \cdot 10^{-7}$
1 to 1000	$6.9 \cdot 10^{-7}$	–

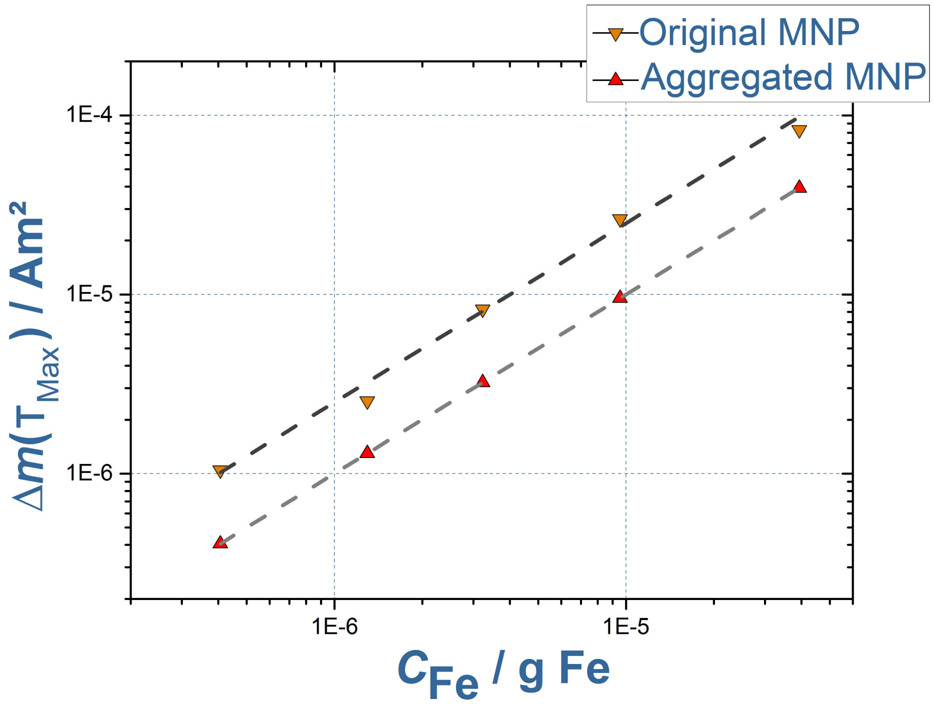

Figure 4.18: Nominal total iron content versus relaxation amplitude at the maximum temperature for aggregated and unaggregated particles. While the samples had different peak temperatures, the ratio of the amplitude to the iron content was the same for both.

Conclusion

TMRX reveals detailed information about the magnetic behavior of MNPs. In the present study, aggregation led to an increase in the temperature of the amplitude maximum because of dipole–dipole interactions. The aggregated particles had a smaller average core–to–core distance, which increased the interaction energy and slowed down particle relaxation. Notably, the dilution series revealed that the magnetic relaxation signals scaled linearly with concentration, implying that the underlying interaction process was independent of concentration. Hence, dipole–dipole interactions are attributed to the formation of a local MNP superstructure consisting MNP clusters or aggregates. The dipole–dipole interactions within the superstructure predominate over interactions caused by concentration effects.

4.5 Multicore Particle Analysis via TMRX of Underlying Fractions

Abstract 4.5 The applicability of TMRX for the investigation of Multicore Particles was illustrated. An MNP solution was separated into two fractions via static separation and the separation products analyzed via TMRX. *Gum Arabica*–covered multicore particles [67] designed for MRI use and their precursor particles were used for this study. A static separation process was performed on the precursor particles in order to determine whether or not only certain fractions were integrated into the multicore particles. ■

Introduction

All biomedical applications of magnetic nanoparticles depend on the particular magnetic properties of the MNPs. How suitable a particle type is for a specific application is amongst, other things, determined by its magnetic characteristics, size, and surface properties. One method for improving these characteristics is to develop advanced chemical processes that produce MNPs tailored for a desired task. Another approach is to improve existing particle solutions through specific filtering procedures, i.e., the separation of desired particles. MNP separation is a currently developing research field within the nanoparticle community with growing impact. Unlike purely mechanical filtration, magnetic separation divides the particles based of their magnetic properties, and not just their geometric sizes. In biomedical applications, magnetic separation is used to improve the quality of magnetic tracer particles for magnetic particle imaging and magnetic resonance imaging.

Investigated Particles

The precursor particles were produced by thermal decomposition of Fe(acac)3 in organic solvent and then coated with meso-2,3-dimercaptosuccinic acid (DMSA). The DMSA coated MNPs were then reacted with Gum Arabica (GA), leading to the formation of covalent bonds between the DMSA and GA, and thus multicore particles. GA is a hydrophilic, composite polysaccharide harvested from the exudates of Acacia senegal and Acacia seyal trees. To solutions of the DMSA-coated precursor and GA–containing multicure particles, 30 µL mannitol solution (containing 15 % mannitol) was added. Each solution was then immobilized in a polycarbonate capsule via freeze drying to obtain stable samples. A solution of the precursor was also forcefully aggregated via dehydration. The iron concentrations of the original precursor and GA–coated multicore particle solutions were 1,37 mg iron per mL and 1,2 mg iron per mL, respectively. Transmission Electron Microscopy (TEM) using a 100-kV JEOL JEM1010 microscope was performed to characterize the particle size of the DMSA particles (Figure 4.19).

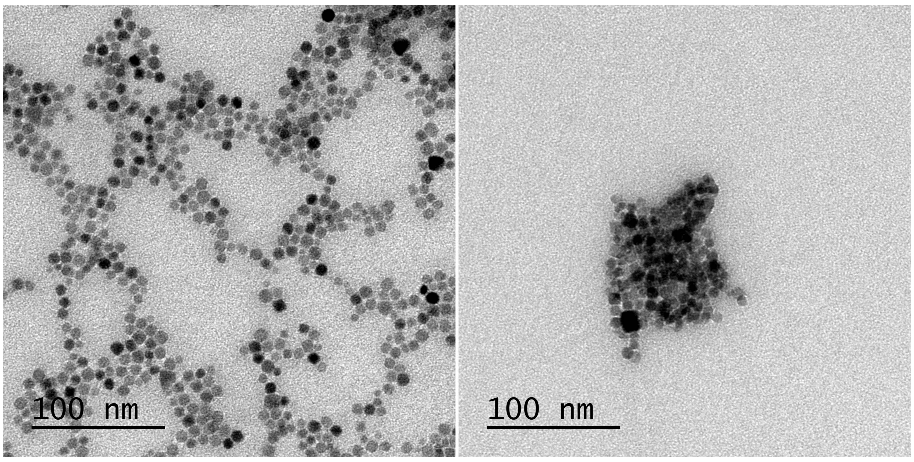

Figure 4.19: (Left) Transmission Electron Microscopy (TEM) image of the DMSA–coated precursor and (right) Gum Arabica multicore particles. (Picture from [67])

TMRX Measurement Procedure

The measurements were performed using a Quantum Design SQUID magnetometer (MPMS-XL) and RSO measurements following the procedure described in Section 3.2.5.

Separation Procedure

The original precursor solution was diluted with distilled water to an iron concentration of 0,1 mg iron per liter. The diluted sample was then separated using commercial cell separation columns (Miltenyi Biotec MACS) in combination with a permanent magnet (Miltenyi Biotec MiniMACS Separator). The strong magnetic gradient in the column led to retention of the larger MNPs and passage of the smaller particles. The retained and collected fractions are referred to as the eluate and discharge, respectively.

4.5.1 TMRX Analysis of Multicore and Precursor Particles

First, samples of the immobilized precursor and multicore particles were analyzed using the described TMRX sequence. Notably, even though the magnetic cores within the precursor MNPs and MCNP were the same, their magnetic relaxation behaviors were unequal. The TMRX measurements displayed in Figure 4.20 show the amplitude changes as a function of temperature for the two MNP samples. The DMSA–coated single core particles exhibited the largest relaxation amplitude at 60 K and a secondary maximum at 120 K. However, the GA–covered, multicore particles only showed a single maximum at 130 K. In addition, the overall amplitude per milligram of iron was reduced to approximately 50 % for the latter sample. The TEM analyses (see Figure 4.19) indicated that the precursor consisted of MNPs with a narrow core size distribution of 7,1 nm ± 1,4 nm. While the multicore particles consisted of these cores, the cores were combined into larger structures. The TMRX signal of the GA–covered multicore particles reflected the magnetic characteristics of particles with larger cores. A temperature peak at 130 K is typically obtained for particles with magnetic iron oxide cores of 15 nm to 18 nm. It was uncertain, however, whether the results of these TMRX measurements indicated that the multicore particles included a fraction of particles

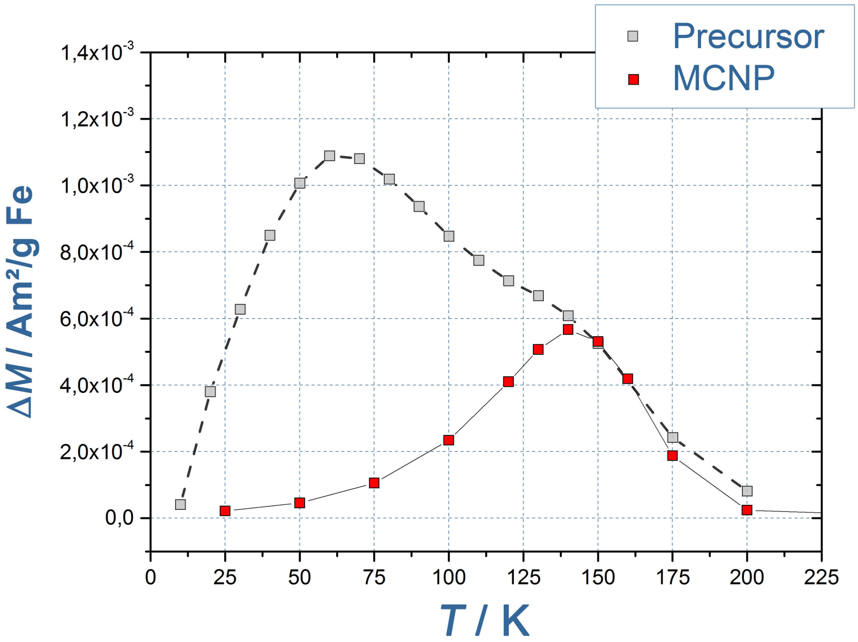

Figure 4.20: TMRX Spectra of precursor and GA-coated MNPs. The precursor particles (gray squares) exhibited the largest relaxation amplitude at 60 K and a secondary shoulder at 120 K. The GA–covered multicore particles (red squares) only exhibited one maximum at 130 K.

larger than the median precursor particles or whether these unusual TMRX signals were because of dipole-dipole interactions.

4.5.2 TMRX Analysis of Separated Particles

In order to investigate the single core MNPs in more detail, a static separation was performed because the TMRX signal of the sample indicated the presence of two fractions with different size distributions. The subsequent static separation divided the solution into discharge, i.e., smaller particle fraction, and eluate, or larger particle fraction. The TMRX analyses (Figure 4.21) of the eluate exhibited a peak amplitude at 110 K, whereas the peak amplitude of the discharge appeared at 70 K to 80 K. The amplitude strength per mg iron was slightly higher than that of the original precursor for both fractions. Separated fractions typically have higher signal per gram iron ratios than original solutions because the relaxation spectra are narrower for separated particles. The presented results indicated that the static separation of the precursor particles was successful, and that fractions of larger and smaller particles were separated. It was, however, still unknown whether the large fraction contained 20 nm–sized particles or if it consisted of agglomerates of 7 nm single core particles that interacted with one another. Analysis of the TEM images did not indicate the presence of 20 nm–sized particle cores. In order to obtain a sample with dipole–dipole interactions, the precursor solution was aggregated via drying. The TMRX signals for this aggregated sample, the multicore particles, the two separated fractions, and the original precursor are displayed in Figure 4.22. It can be seen in the figure that the amplitude per gram iron steadily declined with rising peak temperature. The discharged particles had the highest amplitude and the lowest peak temperature of 70 K while the eluate particles had a peak temperature at 110 K and a slightly lower amplitude. The Gum Arabica covered multicore particles and aggregated precursor followed the latter trend.

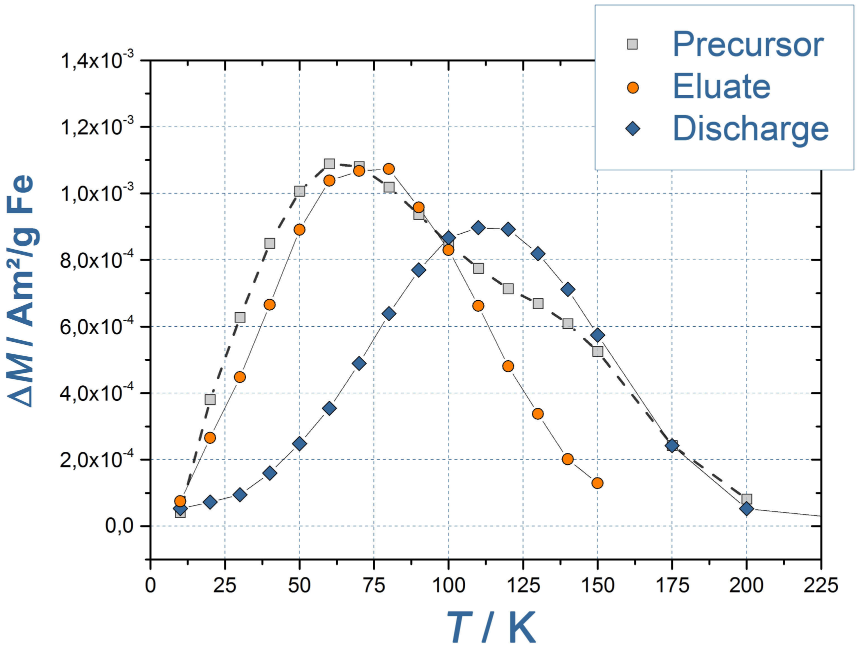

Figure 4.21: The eluate (blue diamonds) exhibited a peak amplitude at 110 K whereas the discharge (orange circles) displayed a maximum at 70 K to 80 K. The amplitude strength per mg of iron for both fractions was slightly higher than that of the original precursor.

This tendency can be attributed to increasing dipole–dipole interactions between the single particle cores. The discharged solution contained only freely moving single core particles with core diameters of 7 nm that experienced almost no interactions. The eluate, however, already contained

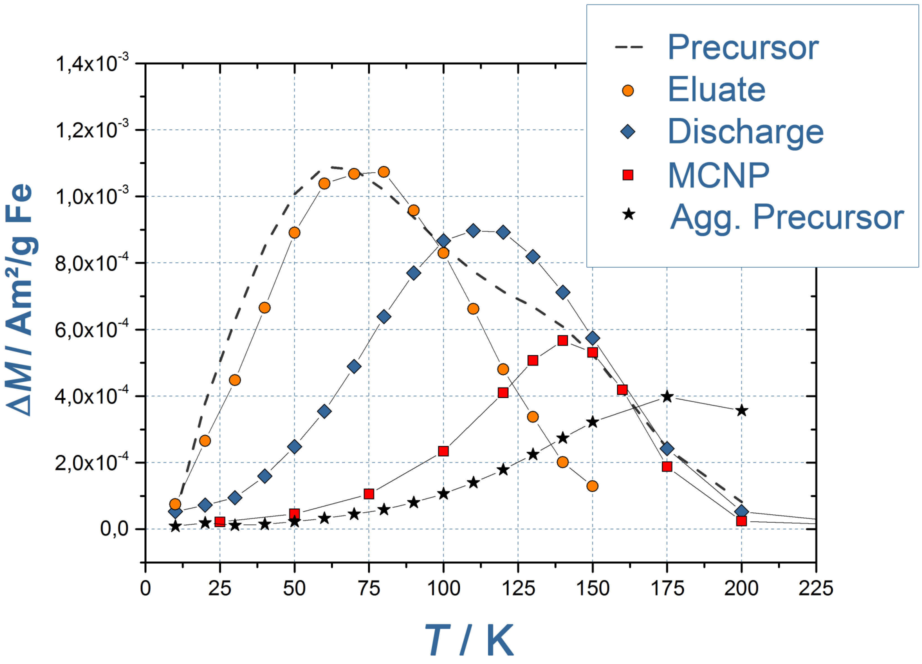

Figure 4.22: TMRX results for the aggregated precursor (stars) compared to the signals shown in Figure 4.20 and 4.21. The peak temperature for the aggregate was 175 K, and its amplitude per gram iron was only 30 % of that of the precursor.

agglomerates of these single core particles. The particles therefore came close enough to each other to allow interaction of their magnetic moments. In the Gum Arabica–coated multicore particles, the single cores were densely packed and experienced even more pronounced dipole–dipole interactions. Finally, in the aggregated form, the single magnetic cores were even closer to one another because their coatings were dehydrated. The magnetic behavior of these MNPs was attributed to the retarding effects of dipole–dipole interactions, as described in Chapter 4.4.

Conclusion

To conclude, the magnetic behavior of the Gum Arabica covered multicore particles was strongly influenced by dipole–dipole interactions and they exhibited the magnetic characteristics of particles 15 nm to 18 nm in size. The precursor, in contrast, showed a predisposition to form these multicore structures even without the Gum Arabica as connector. The magnetic signal of the precursor therefore consisted of a mixture of interacting and non-interacting particles. For this MNP system, the combination of magnetic separation and TMRX analysis enabled further understanding of the underlying magnetism of the multicore particles and their precursor.

5. Numerical Simulation of TMRX Spectra

5.1 Influence of Dipole–Dipole Interactions on the TMRX Spectrum

Abstract 5.1 Dipole–dipole interactions play an important role in relaxation measurements because these interactions can easily alter the MRX or TMRX signals. In order to investigate the influence of dipole–dipole interaction on the TMRX spectrum we analyzed a dilution series of the clinical contrast agent Endorem. TMRX analysis of the series revealed changes in the peak signal temperature and curve shape that correlated with sample concentration, clearly indicating the degree of dipole–dipole interactions at each concentration step. Next, TMRX spectra were simulated using various equations (Langevin equation for MNP magnetization, Néel formula for particle relaxation, ect.) in combination with information about the size distribution of the particles. While the simulated results reproduced the relaxation behavior of the most dilute samples, they were not in agreement with the data for the samples with higher concentrations. In order to slow down the relaxation for the highly concentrated samples, a dipole–dipole interaction term was included. Specifically, an interaction energy term was numerically adapted because conventional approaches for dipole–dipole interactions were not sufficient to describe the experimental data. The different simulations were evaluated based on their quantification accuracy and plausibility. Notably, introduction of the novel numerical interaction term enabled accurate simulation of the TMRX spectra of the investigated dilution series and quantification of the individual samples. ■

Magnetic Nanoparticle Samples

The contrast agent Endorem contains dextran–coated superparamagnetic magnetite nanoparticles with core size diameters ranging from 5 nm to 10 nm. The MNP stock suspension with c_{Fe} =11,2 mg/mL was diluted using distilled water (Milli-Q, Millipore Corporation) to six different iron concentrations, and subsequently 100 µL volume samples were immobilized by freeze drying. The concentration of the freeze dried stock suspension **S** was 106 mg iron per gram sample. The resulting solid dilution samples **C1**–**C6** had concentrations of 58,9 mg, to 0,16 mg iron per gram sample, respectively. These samples were the same as those recently used in an AC susceptibility study [52]. In that study, the Endorem dilution series was analyzed and used as references for the quantification of MNPs in the liver and spleen tissues of rats. Here, the same dilution series was investigated using TMRX in order to compare the experimental data with simulated results. The given iron contents from [52] are listed in Appendix 9.1.

TMRX Measurement Procedure

The measurements were performed using a Quantum Design SQUID magnetometer (MPMS-XL) according to the procedure described in Chapter 3.2.5.

TMRX Measurement of the Dilution Series

The effect of decreasing dipole–dipole interactions as a consequence of the increasing inter–particle distance between the MNPs in more dilute solutions was apparent, as can be seen in the TMRX spectra shown in Figure 5.2, where the relaxation amplitude is plotted as a function of temperature. Here, a decrease in the amplitude and a shift in the maximum temperature toward higher temperatures were observed. These signal changes are similar to previously published data concerning dipole–dipole interactions [39]. The different dilution steps for the MNP solution exhibited distinct relaxation maxima at different temperatures well below the room temperature. The increasing dipole–dipole interactions led to a decrease of 50 % in the amplitude and a shift of the relaxation maximum toward higher temperatures by approximately 15 K. While the maximum for the original Endorem solution appeared at 30 K, that for the most diluted fraction C6 was observed at 15 K.

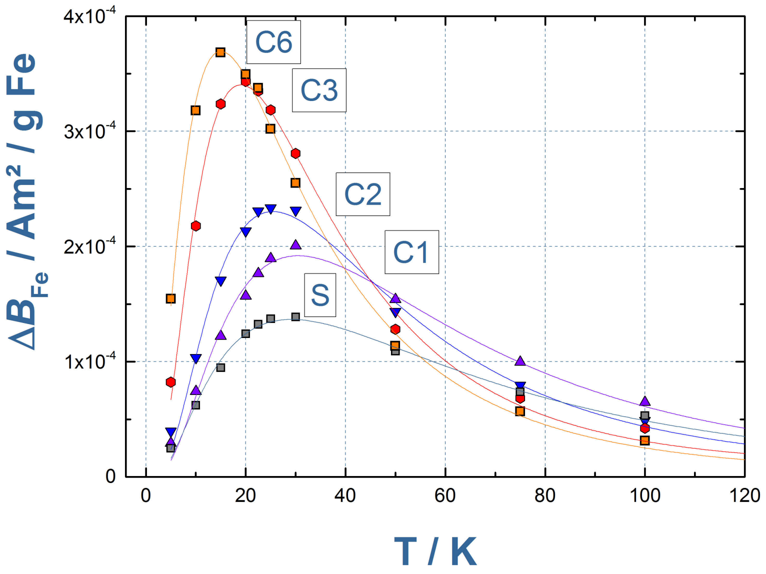

Figure 5.1: TMRX spectra of the investigated MNP dilution series normalized to the iron content. The spectra were well described by a log-normal distribution of temperatures, from which the median temperature T_{med} was extracted.

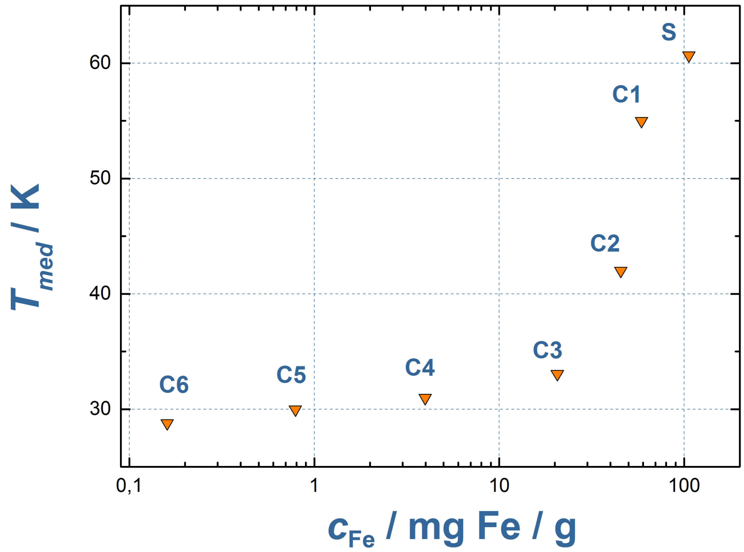

Figure 5.2: Median temperature obtained from the log-normal fit of the TMRX spectra for the Endorem dilution series. The medium temperature was plotted as a function of the corresponding concentration.

The TMRX spectra shape was well–described by fitting a log–normal distribution, which also provided the position of the maximum and the width of each individual TMRX spectrum. The log–normal fit parameters displayed in Figure 5.2 revealed that the median temperature (T_{med}) of the original Endorem solution was twice as high as T_{med} for the diluted solutions. Importantly, the median temperature remained nearly the same for the three least–concentrated fractions. Therefore, C6 can be assumed to be interaction free.

5.2 Simulation of TMRX Spectra of Non–Interacting Particles

Abstract 5.2 TMRX spectra of non-interacting particles were simulated based on the Néel relaxation process. A log-normal distribution of the sample core diameters was assumed. In order to include this distribution, a numerical discretization of the Néel equation was performed. The sample's relaxation behavior at a specific temperature was assumed to be the sum of the underlying relaxations of the discretized magnetic moments. ■

The magnetic relaxation signal of single MNPs can in general be described through the equations given in Chapter 2.1. However, real magnetic nanoparticle samples normally exhibit a distribution of core diameters, which commonly is described by a log-normal distribution with median core diameter $\tilde{d}$ and variance σ_d (see also Chapter 2.1.3). The size distribution must be considered in the relaxation time because τ is dependent on the core volume of the particles. Analogously, the magnetization amplitude is also dependent on the particle core diameter d.

The probability density function (Equation 2.8) must therefore be discretized in order to obtain the individual probabilities of the different core diameters in the sample. Here, the discrete probability function ($P(d_i)$) is defined over $i = 1, 2, 3 \ldots N$ as

$$P(d_i) = P_i = \frac{1}{\sqrt{2\pi}\sigma_d d_i} \exp\left(-\frac{\ln^2(d_i/\tilde{d})}{2\sigma_d^2}\right), \tag{5.1}$$

with

$$\int P(\bar{d})(d)\bar{d} \approx \sum_i^N P(d_i)\Delta d = \sum_i^N P_i \Delta d = 1. \tag{5.2}$$

The vector $\bar{d}$ contains the possible discrete core diameters d_i from $d_0 = 0\,\text{nm}$ to $d_N = 100\,\text{nm}$. The discretization step size is defined as $\Delta d = (d_N - d_0)/N$. In order to display the discretization of the probability density function, the core diameters of vector $\bar{d}$ were plotted over their probability (see Figure 5.3) assuming a median diameter ($\tilde{d}$) of 10 nm and variance (σ_d) of 0,3.

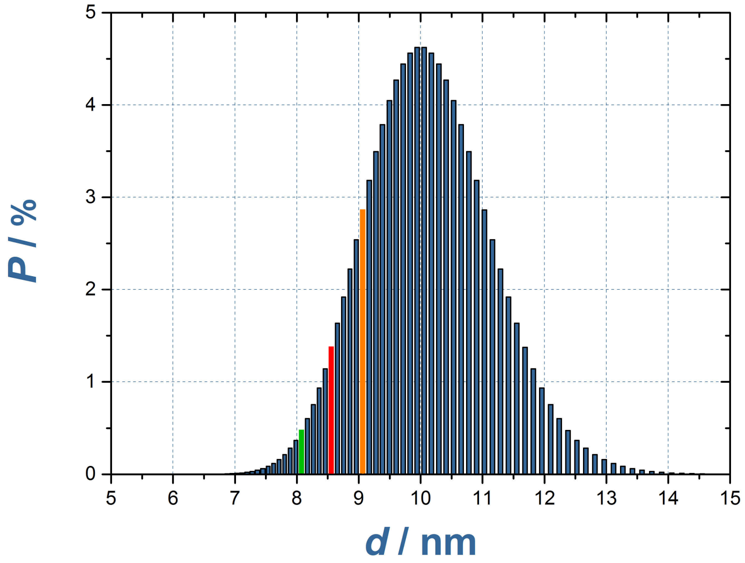

Figure 5.3: Discretized core diameters (d_i) with corresponding probability densities (P_i) when $\tilde{d} = 10\,\text{nm}$ and $\sigma_d = 0,3$. In order to illustrate the discretization of $\bar{d}$, a particular large discretization step size was chosen. Highlighted respectively in green, red, and orange are the discrete values for the 8 nm, 8,5 nm, and 9 nm sized particles in the simulated distribution. In Figures 5.4 and Figure 5.5, their influence on the magnetization process and relaxation signal at a specific temperature are displayed.

The relaxation of a sample's magnetic moment toward its equilibrium state is generally described by Equation 2.3: $M(t) = A\exp(-t/\tau_N)$, with the Néel relaxation time τ_N, and an initial magnetization amplitude A. Assuming the net magnetic relaxation signal of the sample is a combination of the single relaxations of individual particles according to their probabilities, the time dependency of the sample's magnetic moment may be written as

$$M(t) = \int P(d)A(d)\exp\left(\frac{-t}{\tau_{\mathrm{N}}(d)}\right)\mathrm{d}d \approx \sum_{i}^{N} P_i A_i \exp\left(\frac{-t}{\tau_{\mathrm{N}i}}\right)\Delta d. \tag{5.3}$$

The magnetization behavior of the discretized core diameters can then be calculated according to the Langevin equation (Equation 2.2). In the present cases, for each diameter d_i, a corresponding magnetic moment m_i was calculated using $V_i = 1/6\pi d_i^3 = m_i M_S$, and a constant saturation magnetization of 379 400 $\mathrm{Am}^2/\mathrm{kg}$, which is typical for magnetite MNPs, was assumed:

$$M_0(d_i) = M_{0i} = NP\frac{\pi d_i^3 M_S}{6}\left(\coth\left(\frac{\pi d_i^3 M_S B}{6k_{\mathrm{B}}T}\right) - \frac{6k_{\mathrm{B}}T}{\pi d_i^3 M_S B}\right). \tag{5.4}$$

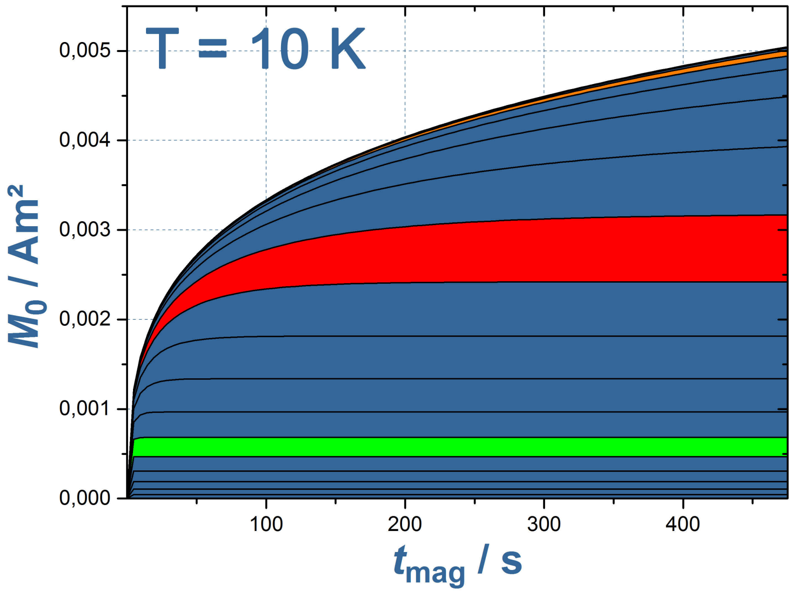

Figure 5.4: Simulation of the magnetization process at 10 K based on the 10 nm particle distribution displayed in Figure 5.3. The time dependency of the magnetizing phase was calculated using Equation 5.6. The net magnetization of the sample was calculated by summing up the magnetizations of the discretized particle sizes according to their probability densities. In the MPMS magnetization process, the magnetization time (t_{mag}) was set to 480 s and the external field to 1 mT. Although the particle distribution exhibited a median at 10 nm, the particles that were active at 10 K were in the 8 nm (green) to 9 nm (orange) range. Most prominent was the influence of the 8,5 nm particles (red) on the magnetization curve.

Here, B represents the external magnetic field and T represents the sample temperature. Boltzmann's constant (k_B) is defined as $1{,}38 \cdot 10^{-23}$ J/K, and the number of particles NP is defined as an adjustable scaling factor. During the magnetization interval (t_{mag}) the sample's net magnetic moment exponentially converges toward the magnetization-value M_0. The discretized amplitude $A(d_i) = A_i$ of this initial magnetization is given by

$$A(d_i) = A_i = M_{0i}\left(1 - \exp\left(-\frac{t_{mag}}{\tau_i^{field}}\right)\right). \tag{5.5}$$

The magnetization of the sample is the sum of the magnetic moments of the discretized single particles and their corresponding probability densities. The magnetization process for a distribution of MNPs is illustrated in Figure 5.4.

$$A(t) = \sum_i^N P_i M_{0i}\left(1 - \exp\left(-\frac{t_{mag}}{\tau_i^{field}}\right)\right) \tag{5.6}$$

Similar to the Néel relaxation process the magnetization process, can be described through a magnetization time constant (τ^{field}) which is field dependent [22]:

$$\tau^{field}(d_i) = \tau_i^{field} = \tau_0 \exp\left(\frac{KV}{k_B T}\left(1 - \frac{0.82 B \mu_0 M_S}{2K}\right)\right). \tag{5.7}$$

A typical fixed value of $1 \cdot 10^4$ J/m^3 for magnetite MNP was used as the value of the magnetocrystalline anisotropy constant (K). The relaxation time constant τ_0 was assumed to be $1 \cdot 10^{-11}$ s. The Néel relaxation time (τ_N) was then calculated for each discretized core diameter d_i:

$$\tau_N(d_i) = \tau_{Ni} = \tau_0 \exp\left(\frac{K\pi d_i^3}{6 k_B T}\right). \tag{5.8}$$

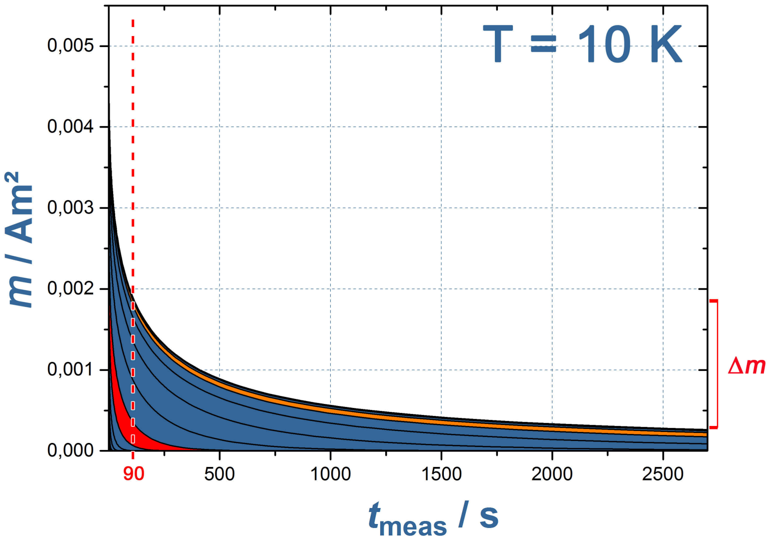

Figure 5.5: Relaxation process for the 10 nm particle distribution shown in Figure 5.3 simulated using the discretized Néel formula (Equation 5.8). The relaxation signal is the summation of the individual decaying moments of the discretized particles. At 10 K, particle cores with a diameter of 8,5 nm(red) relaxed mainly in the first few minutes. Smaller particles (e.g., 8 nm, green, see Figure 5.4) relaxed in the microsecond range and are therefore not seen here. Only larger particles with diameters near 9 nm relaxed over the entire measurement time of 45 min. A dead time of 90 s, which is typical for MPMS analyses, is indicated with a red dashed line. The amplitude change (Δm) is the difference between the magnetic moment at the end of the dead time and the remaining magnetic moment at the end of the measurement phase.

Using Equations 5.3 – 5.8, it was then possible to simulate the relaxation processes of MNP samples with distributions of the core diameters. The final relaxation moment is a summation of the individual moments of the discretized particles based their probability densities. The relaxation of a 10 nm particle distribution (see Figures 5.3 and 5.4) is shown in Figure 5.5. In the simulation, the time parameters were the same as those used for the MPMS analyses, i.e., a delay time of 90 s and a measurement time of 45 min.

In Figure 5.5, the relaxation process is displayed for $T = 10\,\mathrm{K}$. In particular, particle cores with diameters of 8 nm – 9 nm contribute to the relaxation signal at this temperature. In the temperature dependent MRX simulation, the relaxation process for a sample is therefore calculated at temperatures ranging from 5 K to 300 K. In the TMRX plot, the amplitude change (Δm) is displayed as a function of temperature. In Figure 5.6, the simulated TMRX spectrum is plotted for the 10 nm particle distribution shown in Figure 5.3, which had a core diameter variance of $\sigma_d = 0,3$. For comparison, a 10 nm particle sample with no size distribution is also displayed (blue line).

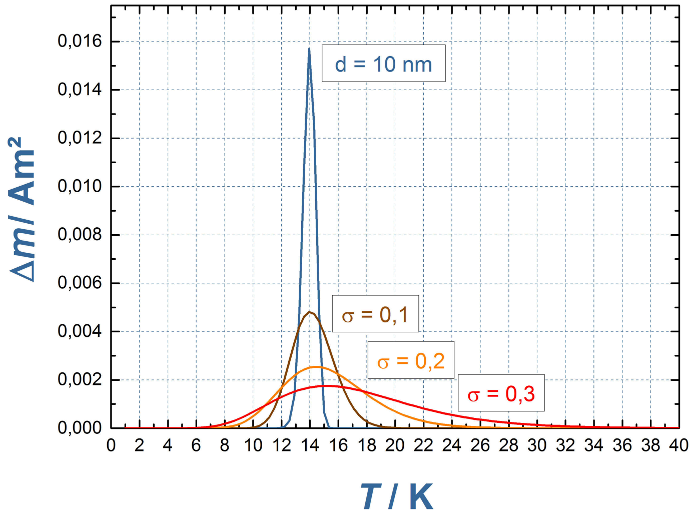

Figure 5.6: Simulated TMRX spectra of four different simulated samples displayed as a function of temperature. The spectrum for a monodisperse sample consisting only of 10 nm particles is illustrated in blue while the spectrum for a simulated MNP sample with a core size distribution of $\tilde{d} = 10\,\mathrm{nm}$ and $\sigma = 0,3$ is presented in red. Distributions with $\sigma = 0,2$ (orange) and $\sigma = 0,1$ (brown) are also shown.

The influence of the size distribution width can be clearly seen in the figure. The maximum temperature slightly decreased from 16 K for the distributed particles (red) to 14 K for the monodisperse sample (blue). Even more pronounced was the change in the width of the TMRX spectrum for the samples with a particle size distribution. The sample with a variance (σ) of 0,3 yielded a relaxation over the temperature range 6 K to 34 K while the non–distributed particles (blue) only generated a narrow relaxation signal from 12 K to 16 K.

Using this simulation approach, the experimentally obtained TMRX spectra for the Endorem samples were further analyzed in order to extract information about the particle's core size and distribution width. However, this simulation did not include an interaction energy term. Therefore, any signal alterations because of dipole–dipole interactions were expected to falsify the analyses. In the Endorem dilution series, only the most diluted sample was assumed to be interaction free (Figure 5.2, sample C6).

5.3 Simulation of TMRX Spectra Including Dipole–Dipole Interactions

Equation 2.4 for the Néel relaxation time is valid for non–interacting particle systems. As described in Chapter 2.1.4, the Vogel–Fulcher equation is one approach for including dipole–dipole interactions in the Néel equation in order to slow down the relaxation time such as in spin glasses. In the Vogel–Fulcher law (Equation 2.11) a critical temperature (T_0) is introduced to compensate for the difference in the measured and calculated blocking temperatures. The Vogel–Fulcher law may be discretized based on the core diameters in the distribution d_i with $i = 1,2,3...N$:

$$\tau_i = \tau_0 \exp\left(\frac{\Delta E}{\mathrm{k_B}(T - T_{0i})}\right) = \tau_0 \exp\left(\frac{K\pi d_i^3}{6\mathrm{k_B}(T - T_{0i})}\right). \tag{5.9}$$

As introduced in Chapter 2.1.4, one method for estimating T_0 for an ensemble of nanoparticles is by using simplified dipole–dipole interaction equation (Equation 2.14):

$$T_0 \approx \frac{E_{\mathrm{dipole}}}{\mathrm{k_B}} \approx \frac{\mu_0 m^2}{4\pi \mathrm{k_B} D^3}. \tag{5.10}$$

For the equations that were discretized in the previous chapter, it was sufficient to calculate the independent behavior of a single particle and summarize the resulting magnetic moments according to their probabilities. However, the dipole interaction term for a discrete particle diameter in a distribution can not be calculated without information about the particles it interacts with. Therefore, the interaction energy term must include information about all the particles in the sample and their probabilities.

Discussed below are four different possible numerical implementations of the dipole energy term and a comparison of the calculated results obtained for each of the quantitative data presented in Figure 5.2.

Approach A

One way to include dipole–dipole interactions is to calculate the critical temperature using the median magnetic moment ($\tilde{m} = \tilde{V} M_S$):

$$T_0(\tilde{m}) \approx \frac{E_{\mathrm{dipole}}}{\mathrm{k_B}} = \frac{\mu_0 \tilde{m}^2}{\mathrm{k_B} 4\pi D^3} \tag{5.11}$$

This approach implies that the interaction energy (E_{dipole}) affects each discretized relaxation time (τ_i) with the exact same value $T_0(\tilde{m})$.

Approach B

The interaction energy term can also be calculated using only the discretized magnetic moment (m_i). This approach implies that only particles of the same size are interacting.

$$T_0(m_i) \approx \frac{E_{\mathrm{dipole}}}{\mathrm{k_B}} = \frac{\mu_0 m_i^2}{\mathrm{k_B} 4\pi D^3} \tag{5.12}$$

In this implementation, each discretized relaxation time ($\tau_i = \tau(m_i)$) is affected by a corresponding discretized critical temperature.

Approach C

In approach C, the interaction energy term is the product of the current discretized magnetic moment (m_i) and every other magnetic moment (m_j) and their probabilities ($P_j = P(m_j)$), with $j = 1,2,3...N$:

$$T_0(m_i) \approx \frac{E_{\mathrm{dipole}}}{\mathrm{k_B}} = \frac{\mu_0 m_i \sum_j P_j m_j}{\mathrm{k_B} 4\pi D^3}. \tag{5.13}$$

The critical temperature $T_0(m_i)$ in this approach therefore combines information not only about the simulated single particle but also about the entire particle distribution in the sample.

Approach D

Although different concepts have been proposed regarding the origin of the Vogel–Fulcher law [85] [99], it remains an empirical equation. It is therefore reasonable to discuss other empirical approaches for describing the inclusion of dipole interactions in the Néel relaxation time. Thus, instead of reducing T by a critical temperature T_0, it is possible to directly add the interaction energy term (E_{dipole}) to the anisotropy energy, as in approach D:

$$\tau_{\mathrm{N}} = \tau_0 \exp\left(\frac{K m_i / M_s + E_d(m_i)}{\mathrm{k_B} T}\right). \tag{5.14}$$

E_{dipole} here is calculated in a manner similar to that used in approach C:

$$E_d(m_i) = \frac{\mu_0 m_i \sum_j P_j m_j}{4\pi D^3}. \tag{5.15}$$

Approaches A – D serve the purpose of slowing down the relaxation time as the dipole–dipole interaction energy increases. This retardation of the relaxation process can be attributed to the increasing geometrical frustration of the MNP system [20]. The influence of the particle distribution is, however, different for each approach. Approaches A, B, and C are expansions of the Vogel–Fulcher model, whereas approach D represents a different empirical model. In order to visualize the different influences of approaches A to D on the TMRX signal, simulations were performed, and the results are presented in Figure 5.7. In these simulations, the particle distribution was constant ($\tilde{d}$ =8 nm, $\sigma = 0,25$), and only the interaction energy term was changed by decreasing the interparticle distance (D).

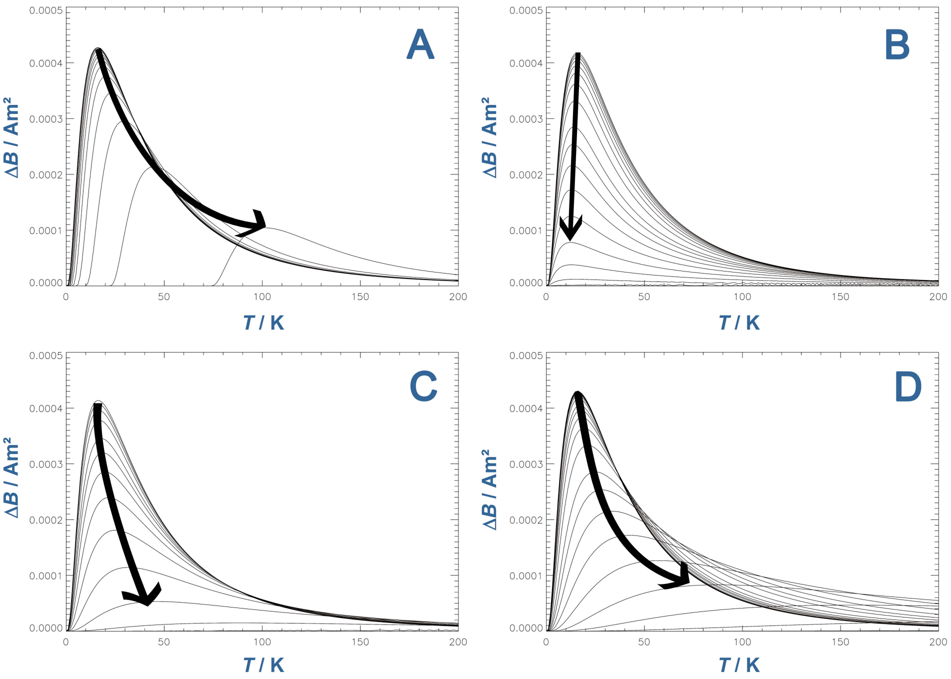

Figure 5.7: TMRX simulations of a log-normal distributed particle system with a mean diameter of 8 nm and a size distribution with $\sigma = 0,25$. Different interaction energy terms (Ed) for the approaches A, B, C, and D were implemented. With a decreasing inter–particle distance (D), the maximum temperatures and shapes of the TMRX spectra changed. The arrows indicate how the increasing interaction energy changes the value of T_{max} in the TMRX spectra.

Starting from a non–interacting distance of 100 nm, the inter particle distance D was decreased in 10 nm steps with logarithmic decreasing step size. As can be seen in the resulting TMRX spectra in Figure 5.7, at the largest simulated distance ($D = 100$ nm), the signal reached a maximum at

15 K. In addition, for all of the approaches (Equations 5.11, 5.12, 5.13 and 5.15) the interaction energy increased as the distance D decreased, resulting in a lengthening of the relaxation time. In all four approaches, this slow–down led to an overall decrease in the amplitude change, i.e., the absolute relaxation signal intensity was reduced. Simultaneously, the peak temperatures changed with increasing interaction energy (indicated by arrows in Figure 5.8). For approaches A, C, and D, T_{max} increased as the interaction energy increased while for approach B, it surprisingly decreased. Approach B was therefore no longer considered because it was unable to describe the experimentally observed increase in T_{max} with increasing interaction energy (see Figure 5.2). Furthermore, the decline in the relaxation amplitude accompanying the change in maximum temperature was different for each approach shown in Figure 5.7, and in most cases nonlinear. Specifically, an increase in T_{max} from 15 K to 20 K was predicted result in amplitude losses of 17 %, 46 %, and 23 % for approach A,C, and D, respectively. This alteration of the TMRX spectra is of utmost importance for quantification because the process involves scaling of the simulated spectra to the experimentally obtained results. The introduction of the interaction energy terms not only change the maximum temperatures but also the shapes of the TMRX spectra. Previous analyses indicated that that the interaction energy often has a broadening effect on TMRX spectra (see also Chapter 4.4, Figure 4.16). The TMRX spectra of interacting samples therefore have the same appearance as those of non-interacting particles but with a broader size distribution σ. In approach A, the entire TMRX spectrum was shifted to higher temperatures with increasing interaction energy (Figure 5.8, A). On the contrary, the TMRX spectra obtained using approaches C and D appeared to be more stretched (Fig. 5.8, B and C).

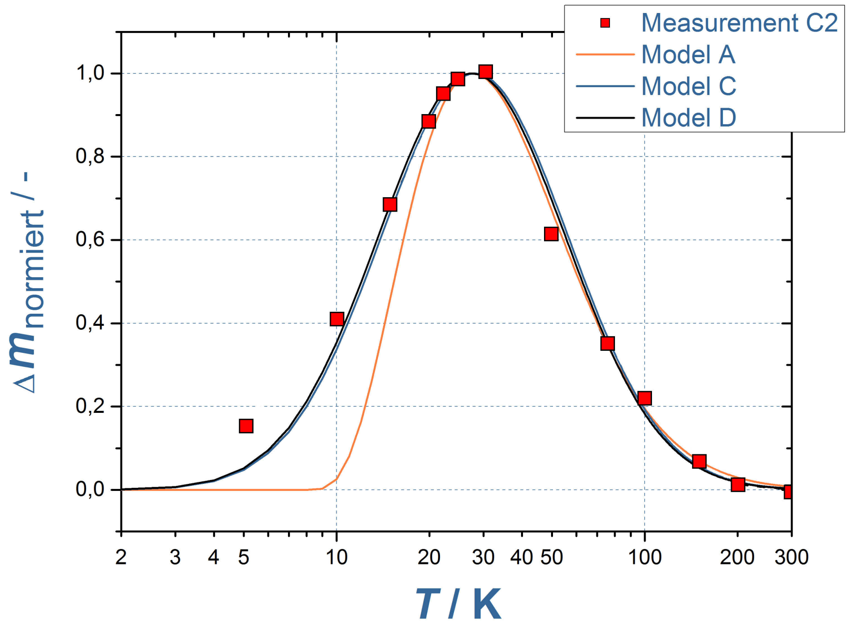

Figure 5.8: TMRX results for dilution step C2 (red squares). Simulation of approaches A, C, and D for a log-normal distributed particle system with a mean diameter of 8 nm and a size distribution of $\sigma = 0,25$. The interaction energy for each approach caused a shift of T_{max} from 15 K to 28 K. In approach A, the spectrum was shifted as a whole and not stretched like in approaches C and D.

A comparison of the simulated and experimentally obtained TMRX spectra revealed that approaches C and D have a better correlation with the actual data for dilution step C2 (Figure 5.8). In contrast, the simulated spectrum obtained using approach A exhibited a significant lack of TMRX signals at temperatures below 28 K. One criterion for evaluating the different approaches was to calculate the residuals between the simulated and measured relaxation spectra. A large residual was determined for approach A for the experimental spectrum of the highly concentrated sample.

The quantification accuracy of the different approaches was a second criterion for evaluating their applicability. For non-interacting particles, a valid method for determining the iron content in an unknown sample involves comparison of the peak amplitude at T_{max} in its TMRX spectrum to the peak amplitude at T_{max} in the spectrum of a known sample [43]. This method is referred to as quantification by **peak comparison**. However, the relative amplitude per gram iron can be significantly lowered because of the interaction energy (Figure 5.2). For the Endorem dilution series, this quantification method worked well for T_{max} from 15 K to 20 K. However, the three most concentrated fractions were underestimated by 35 %, 45 %, and 62 % when using the peak comparison method (Figure 5.9 and Table 9.2 in the Appendix).

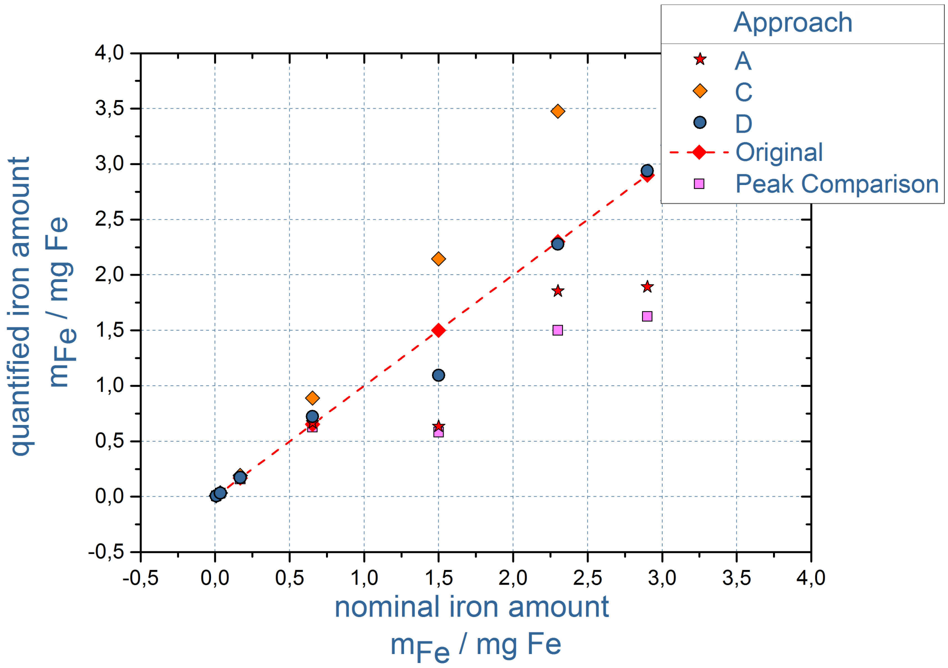

Figure 5.9: Relationship between the experimentally determined nominal iron contents of the Endorem dilution series and the iron contents quantified using the approaches A, C, and D and the peak comparison method.

A comparison of the nominal iron content with the iron content calculated using approach A revealed a similar underestimation as that obtained using the peak comparison method (Figure 5.9). For the low–concentrated dilution steps, the calculated iron content equaled the nominal iron content. For the samples with high levels of interactions, however, the iron content was underestimated by 20 % to 58 % (see Table 9.3 in the Appendix). The quantification accuracy of approach C was similar to that of approach A, although the iron content was overestimated for the highly concentrated particle suspensions (150 % – 190 %, see Table 9.4 in the Appendix). However, using approach D, the quantified iron content was in good agreement with the nominal iron concentration for most samples (see Table 9.5 in the Appendix). Only the content in the most concentrated dilution step was underestimated by 27 %; the concentrations in the other samples were calculated with an accuracy of approximately ± 10 % (Figure 5.9, Model D).

Thus, compared to the other three approaches, model D had the highest quantification accuracy. Finally, a comparison of the estimated interparticle distances (D) for the four approaches was performed. In the original dipole interaction equation for two ideal spheres (Equation 2.13), D describes the center–center distance. In Equation 5.10 used for these simulations, however, D represents the average distance between the particles. The particles in the distribution have a median core diameter $\tilde{d}$ and an additional coating with a thickness of several nm (r_{coating}), and therefore D should not be less than $\tilde{d} + 2r_{\text{coating}}$. For the Endorem dilution series, the Dextran coating thickness was approximately 3 nm. Unlike for approaches A and C, the center–center distance was found to be less than $\tilde{d} + 2r_{\text{coating}}$ when fitted using Approach D for the more highly concentrated suspensions, and was therefore unrealistic.

Conclusion

Simulation of TMRX spectra was performed by employing a novel mathematical model that describes the dipole–dipole interaction within an MNP sample. The calculated spectra were compared with experimental obtained data for an MNP dilution series. The simulated spectra revealed changes in the maximum amplitude T_{max} and also the decline in the amplitude strength because of dipole–dipole interactions.

A homogenous distribution of the particles in the sample without local clusters or specific bindings was assumed. Some of the interparticle distances fitted using the novel model fell in an unrealistic range. Therefore, they cannot be interpreted as absolute values. The introduction of an additional factor may, however, enable their adjustment to real values. The determination of this factor would require further experiments and knowledge of the actual interparticle distances in the MNP samples.

6. Development of a TMRX System for the Short Time Regime

6.1 Custom TMRX Measurement System

Abstract 6.1 A non–magnetic, cryogenic system that provides a variable sample temperature environment from 5 K to 290 K was constructed. The helium cryostat was intended to hold standard PCR sample tubes and to fit into the warm bore of the 6-channel MRX system [2] (see also Appendix 9.1). The cryostat was designed to be combined with an Oxford Instruments low loss transfer tube (LLT 600) with a needle valve for helium transfer regulation. The most prominent difference from commercially available cryogenic systems was the use of a glass fiber–reinforced material for construction of the cryostat walls. The non-magnetic cryogenic system is suitable for magnetic measurements with fast changing fields because disruptive eddy currents do not occur. The cryostat is also connected to an external copper coil and is thus capable of performing temperature dependent MRX analyses in combination with the multichannel SQUID system. The coil was designed to magnetize an MNP sample in the center of the magnetizing coil at 1 mT to 5 mT. Although this cryostat was designed to fit into the 6-channel MRX system, it can be moved freely and be used as a temperature–controlled sample holder for other analytical systems. ▪

6.1.1 Description of the Temperature Controlled Sample Holder

The cryogenic system comprises an evacuated, double-walled glass fiber–reinforced plastic (GRP) Dewar vessel combined with a commercial liquid helium transfer tube. In order to fit into the warm bore of the 6-channel MRX system, the insulating outer tube is 25 mm in diameter and 97,5 cm long. The sample space within the double-walled tube is 14,5 mm in diameter. It bears a single-walled, 57 cm long and 7 mm thin GRP tube that transfers liquid helium from the outlet of the helium transfer tube to the sample holder. The outer tube's rear flange has a thread suitable for fitting the helium transfer tube. A commercial 12 V heating coil and a cryogenic temperature sensor (Omega/Newport CY670) are also located inside the Dewar. Their connectors are installed at the rear flange of the transfer tube. In order to minimize heat transfer via thermal radiation, the evacuated GRP double wall contains eight layers of an aluminum–coated polyester fabric [83]. In contrast to the often utilized reflective BoPET film Mylar, the aluminum–coated fabric does not produce eddy currents when exposed to changing magnetic fields. In addition to the fabric, a small amount of granulated activated carbon was placed inside the evacuated double wall. When cooled down, the activated carbon works as a high-capacity adsorbent because of its huge surface area. It therefore removed any remaining or leaking helium particles from the vacuum.

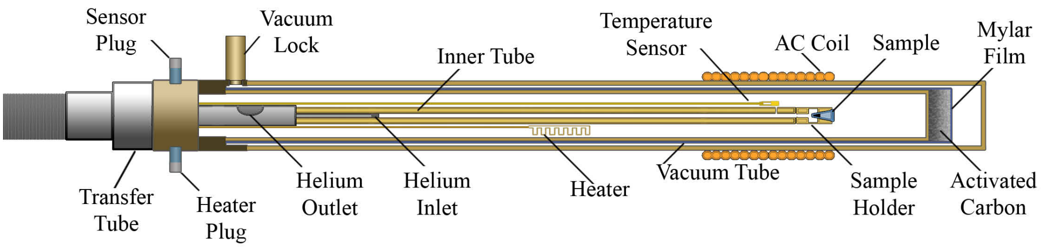

Figure 6.1: Experimental Setup: The data acquisition system (DAQ) reports the relaxation signal (**a**) obtained using the SQUID system and controls the magnetization coil (**b**). The temperature controller reports the data for the temperature sensor (**c**) in the glass reinforced plastic (GRP) cryostat and controls the needle valve (**d**) in the helium transfer tube. The measured temperature is then transmitted to the DAQ System (**a**).

Insulation Fabric

The insulating fabric, previously presented by Seton et al., is made of woven polyester fibers and coated on both sides with 25 nm of aluminum [84]. The single strings consist of 24 10 µm polyester threads and are woven to a pitch of 300 µm. Where the strings touch each other, the metallization on each string is interrupted. The aluminum coating offers excellent reflecting properties while the interrupting thread structure prevents eddy currents. Because the evacuated area between the inner and outer tubes is only 2,5 mm wide, there are currently only 8 layers of the aluminum–coated fabric installed. Prior to the final construction, the materials were tested for magnetic impurities and eddy currents, and the performance of the fabric was compared to that of the conventional Mylar film. Both materials were found to be sufficient for the intended MRX analyses (see Chapter 6.2.2).

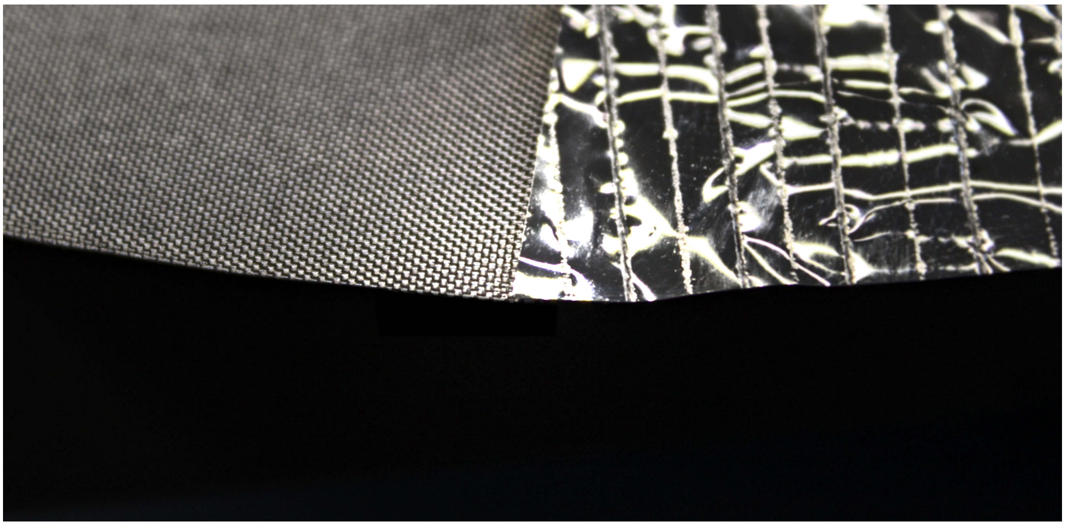

Figure 6.2: One layer of (left) aluminum-coated fabric and (right) slit Mylar film. The aluminum-coated fabric is used as insulation in the Dewar.

Magnetizing Coil

The magnetizing coil is located around the outer GRP tube and directly below the SQUIDs in the multichannel system. Because of the orientation of the coil, the SQUIDs are not disturbed by its magnetic field. The coil consists of 170 windings of a 0,4 mm diameter copper wire. The entire coil is 6,9 cm long and approximately 25 mm in diameter.

Temperature Sensor

In this TMRX setup, a silica temperature diode (Omega/Newport CY670) was used. The voltage of the diode changed with temperature while applying a constant current of 10 mA over the ITC. It was possible to upload a voltage–to–temperature conversion table on the ITC in order to directly monitor the temperature. Because all CY670 silica diodes have a standardized calibration curve, each individual diode does not require a separate calibration, which is advantageous when comparing the signals of two different CY670 diodes during the sample calibration process (see Chapter 6.2.4). The small dimensions of the diode (1 mm $\times$ 1 mm $\times$ 2 mm) make it ideal for taking measurements inside the GRP cryostat. These temperature sensors cover a temperature range of 1 K to 400 K.

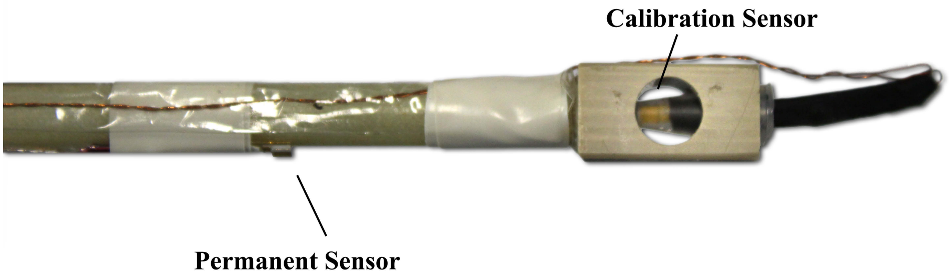

Figure 6.3: Arrangement of the temperature diodes around the sample space. During MRX analyses, the permanently installed temperature diode can only measure the system temperature 4 cm from the sample. In order to calibrate the system, a second (calibration) sensor is installed in a sample dummy.

Glass Reinforced Plastic Tubes

To prevent the generation of induced eddy currents because of magnetic field changes, a non-magnetic and electrical insulating material was required for the cryostat walls. Researchers at the Friedrich-Schiller-Universität in Jena [44] demonstrated that glass fiber–reinforced plastic is a suitable alternative to steel. In particular, researchers found that a thin glass-textured wall with a thick lacquer film (>0,1 mm) can reduce the permeability of the GRP. However, because of its internal structure, the GRP has a higher helium permeability than stainless steel, which leads to overall restriction of the lifetime of the insulating vacuum. Considering this data, glass reinforced plastic tubes from Erhard Hippe KG (EP GC 22.15) were chosen because they have a high density and a lacquer film suitable for vacuum and helium applications.

Resistance Heating Coil

The temperature control unit (Mercury ITC) controls a resistance heater in order to regulate the temperature in the flow cryostat. In conventional cryostats, the heater is installed directly at the sample holder. Typically, this sample holder is a massive copper block with good thermal conductivity. For the intended MRX setup, however, the use of such a copper block was not possible because it would result in the formation of eddy currents that would interfere with the measurements. The resistance heater was therefore installed 6 cm away from the sample holder in order to avoid interference with the measurements. Therefore, the heater cannot be used to directly heat the sample or to warm up the incoming gas. It is, never–the–less, possible to heat the entire system during the warm up sequence. This feature is advantageous it reduces the total measurement time. The dimensions of the foil are 400 mm $\times$ 45 mm, with a thickness of just 1 mm (see also Figure 6.2 in the Appendix).

6.1.2 Description of the 6-Channel TMRX Measurement Setup

The constructed GRP cryostat can be utilized as a temperature controlled sample holder and magnetization unit. However, for TMRX analyses, additional components are required. Thus, a helium transfer tube with an automated needle valve is attached to the cryostat. The transfer tube is capable of reducing the gas flow via the automated needle valve, which is controlled by the temperature and gas flow control unit. In addition, a temperature diode is integrated in the cryostat to determine the sample temperature. This temperature sensor data is also recorded by the temperature and gas flow control unit. Finally, a data acquisition system (DAQ) was developed to store the temperature data and perform the cool down procedure for the cryostat. Magnetic SQUID TMRX analyses are performed using the 6-channel MRX system [2] that existed prior to this work and is therefore not a part of this dissertation. An illustration of the entire setup can be found in the Appendix (Section 9.5).

Temperature Controller (Oxford Instruments Mercury ITC)

A commercial temperature and gas flow control unit (Oxford Instruments Mercury ITC) was used to regulate the temperature within the GRP cryostat. In its stock version, the Mercury ITC is capable of reading out one temperature sensor, controlling one heating resistor, and operating one needle valve. By adding additional plug–and–play expansion cards, the capabilities of the system can be expanded to record data from up to 9 temperature sensors. One of the main features of the system is that it can independently regulate and hold the temperature of the cryostat and run predefined temperature curves and temperature sweeps. The mercury ITC can be operated manually over the build–in touch screen or remotely over the LabVIEW interface.

Helium Transfer Tube (Oxford Instruments LLT 600)

The Oxford Instruments low loss transfer tube (LLT) is designed to transfer liquid helium to horizontally fed cryostats. It has been developed to supply continuous flow (CF) cryostats similar to the temperature controlled sample holder designed in the course of this dissertation. It is ideally suited for the TMRX setup because it can transport gas bidirectionally. The cold gas that exits the cryostat is therefore used to cool the insulation surrounding the incoming liquid within the transfer tube. The transfer tube consists of a 1,3 m long Dewar leg, that fits into the helium vessel, and a 1,2 m long flexible section. The flexible part enables easy adjustment of the GRP cryostat position in the 6-channel system. Its most essential feature is the automated needle valve, which enables regulation of the helium flow used to cool the cryostat. The stepper motor at the valve can be controlled using the mercury ITC, which itself can be programmed via the designed LabVIEW interface. In addition, helium can be transported at temperatures as low as 2,5 K. Consequently, the LLT 600 is ideal for the intended application. A descriptive graphic of the transfer tube can be found in the Appendix (Section 9.4).

The Data Acquisition System (DAQ)

The data acquisition system (DAQ) controls the Mercury ITC and all the MRX–related components and collects the incoming measurement data. Data transfer from the Mercury ITC to the DAQ system occurs via USB. In order to display and save the transferred data in the DAQ, a virtual user interface (VI, see Appendix, Figure 9.6) was designed using LabVIEW (V.12.0.1f5). The required commands for interacting with the ITC using the LabVIEW software and some example applications were provided by Oxford Instruments. All control of and data acquisition from the Mercury ITC and the connected LLT 600 helium transfer tube were achieved using the virtual interface (see Figure 9.6 in the Appendix). The interface was developed and implemented in the course of the dissertation. The implemented commands include readout of the system temperature, opening and closing of the needle valve, and activation of the resistance heating coil. The VI offers the possibility to read in ASCII files in order to perform specific temperature sweeps. Information about the measurement time and date, the temperature, and the percentage opening of the needle valve are also saved in an ASCII text file.

6.2 Characterization of the GRP Cryostat with Magnetizing Coil

Abstract 6.2 Different elements of the cryostat were characterized, including properties and switch-off timing of the magnetizing coil. The magnetic impurities in the raw materials used for construction of the cryostat were also examined. In addition, the optimal position of the sample relative to the magnetizing coil and the appropriate cool down procedure for the cryostat were determined. ■

6.2.1 Characterization of the Magnetizing Coil

An essential part of the MRX setup is the magnetizing coil which had to be specifically designed for the purpose of performing TMRX analyses using the 6-channel SQUID system. The size of the warm bore of the multichannel system restricted the outer diameter of the coil to 26 mm while the size of the outer GRP tube of the cryostat required that the inner diameter of the magnetizing coil be 25 mm.

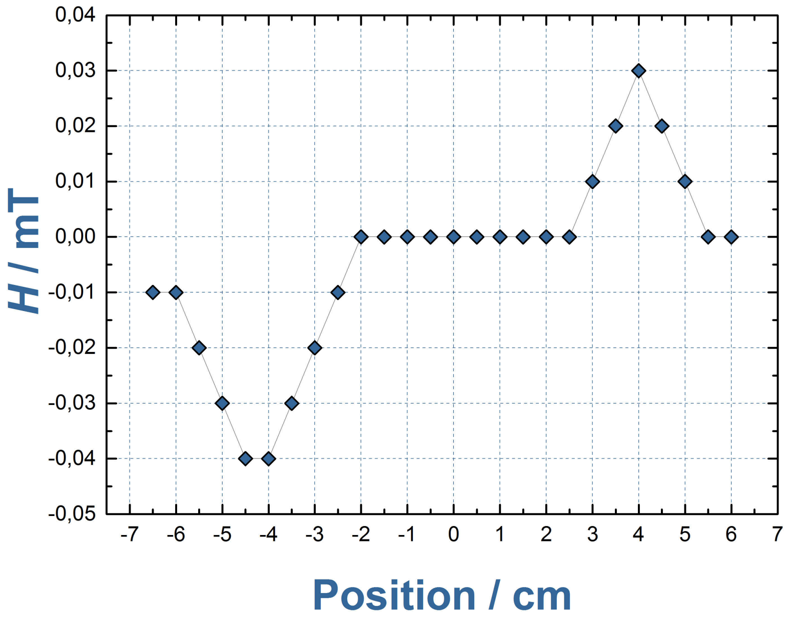

Figure 6.4: Transversal field at the center of the magnetizing coil at 356 mA for different longitudinal offsets. The longitudinal center of the 6,9 cm long coil is marked as zero on the X-axis. The direction toward the helium transfer tube is negatively notated. The curve reveals that the coil produces a small transversal field that is strongest at its longitudinal boundaries. The maxima are therefore at −4,25 cm and 4,0 cm. The transversal field strength at 356 mA ranges from 30 µT to 40 µT at these maxima.

A 0,4 mm copper wire was used for the solenoid magnetizing coil. The single spooled solenoid required a retracting wire that, unfortunately, could only be placed unsymmetrically. Because of its position and orientation, the wire was expected to cause interference for the SQUID sensors. The coil had 170 windings, a total length of 69 mm, and could safely conduct a maximum current of approximately 2,2 A (as determined by its diameter). The measured resistance and inductivity of the coil were 2,2 Ω and 20 µH, respectively. The longitudinal field strength for 356 mA, which is used to magnetize MNP samples, was 1 mT (Figure 6.5) while the maximum transversal field strength ranged from 30 µT to 40 µT (Figure 6.4) because of the small inhomogeneities created by the retaining wire.

The relaxation amplitude strength is directly related to the magnetic moment of the magnetized sample. A higher magnetization field increases the magnetic moment of the sample, as described by the Langevin equation (Equation 2.2). A strong magnetization field therefore improves the detection limit of the system. Although the coil supports currents up to 2,2 A a small current of only 356 mA was chosen for creating a magnetization field that is comparable to the 1 mT used in the MPMS. With an applied field strength of 1 mT, it is feasible to perform the intended MRX and TMRX analyses. In addition, the relaxation signal of small MNPs is strongest at lower temperatures, which also improves the detection limit.

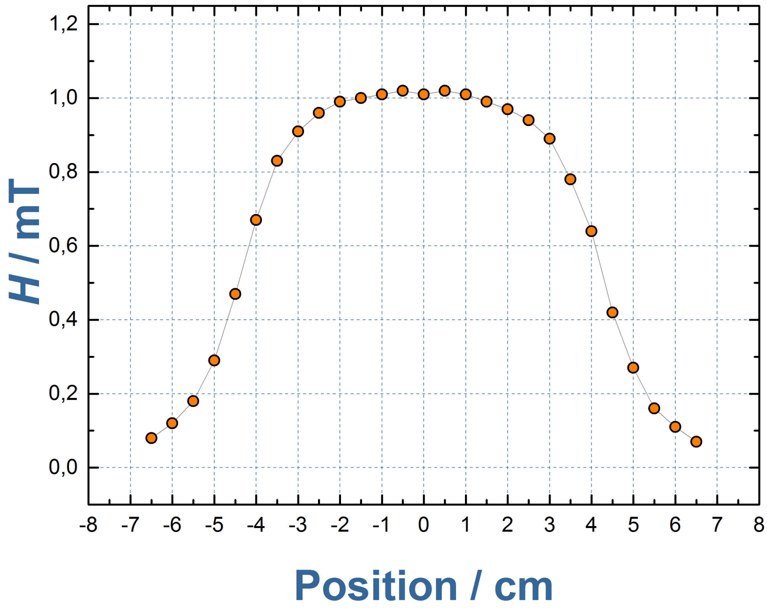

Figure 6.5: Longitudinal field in the center of the magnetizing coil at 356 mA for different axial offsets. The center of the 6,9 cm long coil is marked as zero on the X-axis. The direction toward the helium transfer tube is negatively notated. The curve reveals a maximum plateau ranging from -2 cm to 2 cm with a field strength of approximately 1 mT.

Coil Switch-Off Timing

An important parameter for MRX analyses is the delay time between the end of the magnetization phase and the beginning of the measurement phase. In general, it is favorable to minimize the delay time as much as possible. A long offset between switch-off of the magnetizing coil and the start of the actual measurement results in a high loss of relaxation signal strength. This loss can be compensated for by using longer magnetization and measurement times, which is why the time setting in the MPMS is particularly long. To improve the measurement modalities compared to the MPMS, the dead time in the 6-channel SQUID system was therefore reduced to a minimum.

The necessary length of the delay time in a SQUID-based measurement system is essentially determined by the SQUID's control electronics. In measurement mode, these control electronics compensate gradual shifts. However, during switch-off of the magnetizing coil they must be in *reset mode*. The time when the SQUID sensors may operate again depends on the lingering of the coil and possible flux creep in the Dewar.

In order to reduce the noise level and accelerate the switch-off process, the magnetizing coil is not directly connected to the current source[1]. Instead, a metal-oxide semiconductor field-effect transistor (MOSFET)-switch manages the connection and separation of the circuit. A 10 kΩ resistor is connected in series to the solenoid in order to accelerate the switch-off process. Several Zener diodes with a breakdown voltage of 150 V are located parallel to the magnetizing coil. Below 150 V, the Zener diodes essentially prevent any current flow and therefore reduce the thermal noise of the 10 kΩ resistor.

---

[1] The different devices required to perform the MRX analyses *except* the magnetizing coil were preexisting [33][35] and are therefore not part of this dissertation. These devices include, in particular, the MRX current source, the MOSFET-switch unit with Zener diodes, and the SQUID measurement system.

Using an oscilloscope, the lingering behavior of the magnetizing coil after the switch-off was measured (Figure 6.6).

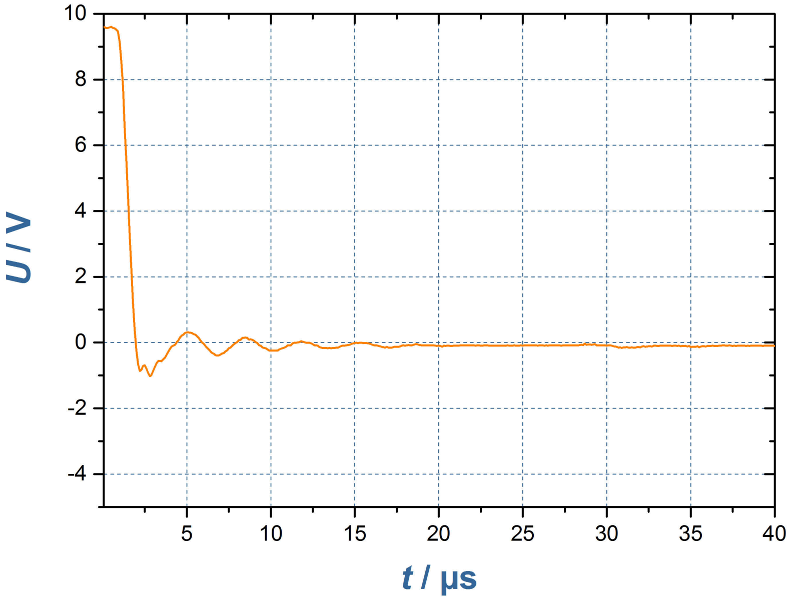

Figure 6.6: Switch-off procedure for the magnetizing coil measured with a Digital Storage Oscilloscope (Agilent Technologies, DSO-X 2004A). After the switch-off impulse is initiated at $t = 0$ s, the voltage in the coil drastically decreases. After 20 µs, the overshooting oscillation ceases as well.

It was found that although the magnetizing coil was deactivated within 20 µs in the existing system, the SQUIDs only began measuring again after 100 µs. The additional interfering signal was attributed to magnetic after–effects in the 6-channel MRX system.

6.2.2 Magnetic Characterization of the System

Magnetic Impurities of GRP Parts

When working with highly sensitive SQUID sensors in a magnetic shielded environment even small magnetic moments in the femtotesla range can be detected. It was therefore crucial to carefully investigate all parts and materials before they were permanently incorporated into the new instrument; even the smallest impurities in otherwise nonmagnetic materials can influence the analytical results. All construction methods, such as cutting and drilling, must be executed with special nonmagnetic tools in a dust–free environment. In addition, all materials must be checked for magnetic contamination after each construction step.

In order to create a magnetically clean cryostat, larger numbers of important parts, such as the GRP tubes, were ordered to ensure that only parts with low magnetic noise were included in the device. The different GRP parts were investigated using the 304-channel SQUID system in the Berlin Magnetically Shielded Room (BMSR-2) at the PTB [9].

Part:	Magnetic Field [pT] at 3 cm distance
Outer Vacuum Tube before cleaning	20
Outer Vacuum Tube after cleaning	10 – 15
Inner Vacuum Tube before cleaning	30
Inner Vacuum Tube after cleaning	5 – 10
Inner Helium Transport Tube	10 – 12
Sample Holder	< 2
Cap	< 2
Flange	< 2

Investigation of the GRP tubes revealed some magnetic contaminants that could be traced back to the manufacturing process. During the production process, the GRP matting is wound along an iron rod in order to form the tube. The contamination was therefore assumed to be primarily on the inside of the tubes and potentially removable. The interiors of the GRP tubes were therefore cleaned using hydrochloric acid (10%) and their subsequent magnetic moments were found to have decreased.

Magnetic Moment of the Insulation Material and its Influence on MRX Analyses

Similar to the GRP parts, the insulation material in the cryostat was also evaluated for magnetic contamination. It is however important to keep in mind that insulation materials such as Mylar film are coated with a reflective metal in order to block thermal radiation. Conducting materials placed close to the MRX magnetizing coil cause eddy currents that can interfere with the measurement. The insulation materials were therefore not only revealed for magnetic impurities but also for their behavior when performing MRX analyses. In order to identify the insulation material with the least interference, both a conventional Mylar film and the aluminum–coated fabric (see Chapter 6.1.1) were investigated. It should be noted that the Mylar film was slit in order to reduce potential eddy currents. The investigation was performed using the magnetizing coil and the 6-channel SQUID system at ambient temperature. A typical MRX sequence with a magnetizing time of 1 s and a measurement time of 1 s was performed for a 30 µL Resovist sample using sample chambers covered in either Mylar film or aluminum–coated fabric. An MRX analysis was also performed for the same sample in a non-insulated sample chamber. In all three spectra, the resulting amplitudes of the peaks appearing at the maximum temperature were identical within the range of the measurement accuracy. This result indicated that no detectable eddy currents were present because the insulation had no disturbing influence on the measurement.

The Mylar film and aluminum–coated fabric were also evaluated for magnetic impurities using the 6-channel SQUID system. Several layers of each insulation material were placed around a sample rod and moved to different longitudinal positions relative to the center of the coil. The amplitude changes (ΔB) for both materials did not exceed ± 5 pT, which was within the range of the background noise.

Magnetic Signal of the Temperature Sensor Diode

The influence of the temperature sensor on the TMRX signal was also a very important factor considered during the design of the GRP cryostat. In general, it is preferable to place the temperature sensor as close as possible to the sample in order to more accurately measure its temperature. However, because the sensor is made partially of metal, it is not possible to do so. Because the distance that the sensor needed to be placed from the sample depended on the strength of the interfering signal, the sensor signal was measured at different positions within the 6-channel SQUID system. Specifically, the temperature diode was placed at different longitudinal positions within the 6-channel SQUID system, and the changes in the amplitude of the peak appearing at the maximum temperature in the MRX spectra were detected.

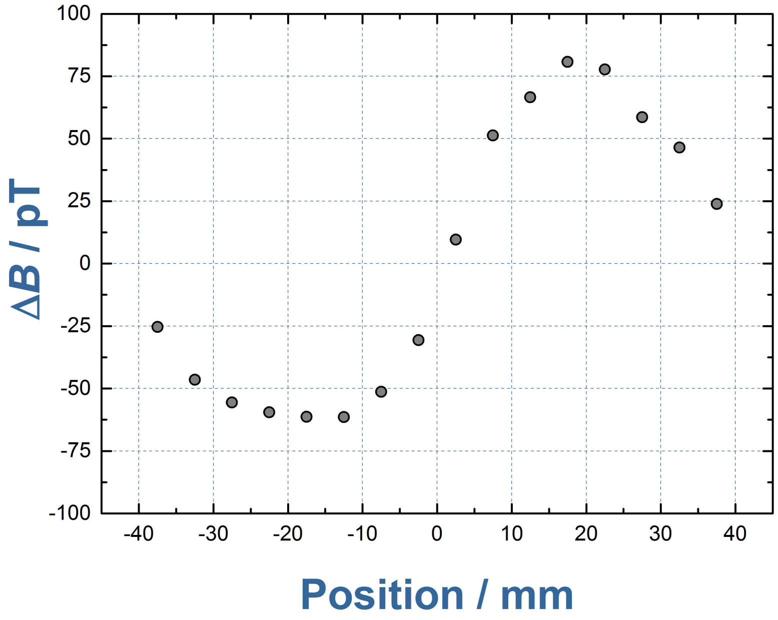

Figure 6.7: MRX relaxation amplitude changes for the silica diode at different longitudinal positions in the 6-channel SQUID system are displayed for one SQUID sensor. The temperature sensor generates a dipole moment similar to that of an MNP sample because of its magnetic elements. The MRX analysis of the sensor was performed at different longitudinal positions from −40 mm to 40 mm relative to the center of the magnetizing coil. A typical MRX sequence (B_{mag} =1 mT, t_{mag} =1 s, t_{meas} =1 s) was performed at each position, and the sensor was operating during the MRX analysis. Therefore, the wires connected to the sensor conducted a 10 µA current.

As can be seen in Figure 6.7, the silica diode caused two distinct maxima at −15 mm and 15 mm respectively. The maximum relaxation signal created by the sensor was about 75 pT. The magnetic moment generated by the sensor can be attributed to impurities in the braze joints of the diode. Therefore, in order to minimize the interference of the temperature sensor on the TMRX analyses, it was determined that the sensor be placed more than 40 mm from the center. Alternatively, the sensor could be positioned at the center of the coil.

Magnetic Signals of other Materials

Additionally the influence of the activated carbon was investigated as it is placed at the rear end of the GRP cryostat and therefore close to the sensors. It did however not produce any interfering relaxation signal. Another concern was the influence of the stainless steel helium transfer tube tip. The tip does produce disruptive eddy currents when placed closed to the magnetizing coil. Due to the design of the GRP cryostat the transfer tube is placed 50 cm away from the sensor and therefore outside of the 6-Channel SQUID system and far enough away from the sensor. The transfer tube therefore produced no detectable signal at that position.

6.2.3 Determination of the Sample Position

During the magnetization phase of a TMRX analysis, the sample must be magnetized by the longitudinal field of the coil. During the measurement phase, the SQUID sensors detect the decaying net magnetic moment of the sample. The orientation of the magnetizing coil is transversal to the measurement direction of the SQUID sensor. Therefore, the longitudinal field of the coil will not be detected by the SQUID sensors. An MNP sample in the center of the coil will create a dipole field when magnetized. If the sample is placed acentrically under the SQUID sensor, the transversal component of the dipole field becomes detectable for the SQUID. This design feature is illustrated in Figure 6.8. The optimal position for the sample was found to lie between 1 cm and 4 cm from the center. At 3,5 cm, the SQUIDs receive the highest transversal response from the MNP sample. Similar to the magnetizing coil, the sample creates a magnetic dipole field with the poles along the long axis of the coil. If the sample is placed directly beneath the SQUID, the sensor is only affected by the longitudinal field. However, our SQUID system is designed to measure the transversal field. The sample must therefore be placed beneath the SQUID with a longitudinal offset, for the sensor to face the transversal magnetic field of the dipole.

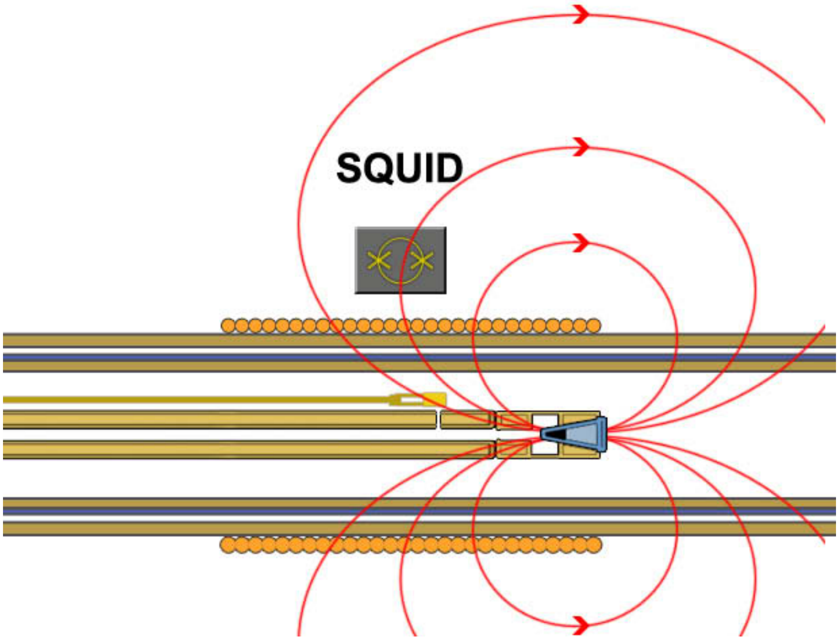

Figure 6.8: Illustration of the sample position relative to magnetizing coil and SQUID. The sample is not positioned directly under the SQUID because the sensor can only detect transversal magnetic fields. Instead, it is placed with a longitudinal offset of approximately 4 cm in order to optimize the transversal magnetic field relative to the SQUID. The magnetizing coil and the permanent temperature sensor are placed directly beneath the SQUID. Through this arrangement, the sensor is less affected by the magnetic dipole fields because they are mainly longitudinal at the center position.

The sample holder was designed in such a way that the permanent temperature sensor is located 4 cm from the sample position. Depending on the position the temperature sensor itself can create a magnetic response that would disturb the measurement. As is shown in Figure 6.7, however, the sensor does not interfere with the measurement when it is placed sufficiently far away from the coil or directly at the center. The permanent temperature sensor was therefore positioned at the center of the coil while the sample was placed at a distance of 4 cm, where it was magnetized by a 1 mT field.

Influence of Thermal Expansion

The sample position within the instrument is important because it determines how the MNPs will be magnetized and the strength of the transversal field received by the SQUID sensors. Any change in its position can therefore result in a signal change and in inaccurate analysis results. The MNP sample is placed in the sample holder, which is located on the inner helium tube. The inner helium tube is a 58 cm long GRP pipe that is mounted on the tip of the stainless steel helium transfer tube. During the cool-down procedure, the stainless steel pipe is 44 cm deep in the installed GRP cryostat. When performing TMRX analyses, the inner GRP tube and the steel tip experience temperature changes of approximately 285 K. Depending on the material, such a thermal change can result in expansion or contraction. Stainless steel, for example, has a coefficient of thermal expansion (α_{steel}) of $17 \cdot 10^{-6}\mathrm{K}^{-1}$, which results in a length change (ΔL_{Steel}) of approximately 2 mm for the given temperature change. The coefficient of thermal expansion for GRP (α_{GRP}) depends on the preferred direction of the material. The given values vary from $7 \cdot 10^{-6}\mathrm{K}^{-1}$ to $27 \cdot 10^{-6}\mathrm{K}^{-1}$, which can result in length changes (ΔL_{GRP}) of 1 mm to 4 mm, respectively. Therefore, the sample position may change between 3 mm and 5 mm in total.

$$\frac{\Delta L}{L_0} = \alpha \cdot \Delta T \tag{6.1}$$

In order to determine the exact influence of changes in the sample position on the signal the thermal expansion coefficient of the GRP tube was determined. A 25 cm long GRP tube was therefore cooled with liquid nitrogen (boiling point 77 K). Using the measured length change ($\Delta L = 0{,}05$ mm) and Equation 6.1, a thermal expansion coefficient for α_{GRP} of $10 \cdot 10^{-6}\mathrm{K}^{-1}$ was determined. Therefore, the GRP tube in the cryostat is expected to contract by approximately 1,5 mm when cooled from ambient temperature to 5 K. For the stainless steel, a length change of 2 mm was assumed. The total position change of the sample was therefore determined to be 3,5 mm for a temperature change of 285 K. According to the positioning tests performed at ambient temperature, such a change in the sample position was determined to lead to a signal loss of 3 %. In order to compensate for this signal change, it is possible to introduce a linear correction term. However, the embedding of such a linear correction term into the analysis software exceeded the scope of this dissertation.

6.2.4 Temperature Calibration at the Sample Position within the Cryostat

The main function of the GRP cryostat is to provide a defined sample temperature from 5 K to 290 K in order to perform TMRX analyses. It is therefore crucial to know the exact temperature of the sample at the time of the measurement. However, the temperature sensor can not be located directly at the sample position because it would interfere with the MRX analyses. The temperature of the sample must therefore be calibrated prior to each analysis.

An MRX analysis using the 6-channel system takes 1 s for magnetization and 1 s for measurement of the relaxation of the sample. Therefore, a temperature sweep procedure was performed using the cryostat to cool the sample at less than 0,5 K/s. This cooling rate is sufficiently slow to assume a constant temperature for individual MRX analyses. During the predefined temperature sweep, the system lowers the temperature continuously. After the intended temperature is reached, the helium inlet is closed and the system heats up again. In order to perform a temperature sweep, a defined temperature alteration rate is mandatory.

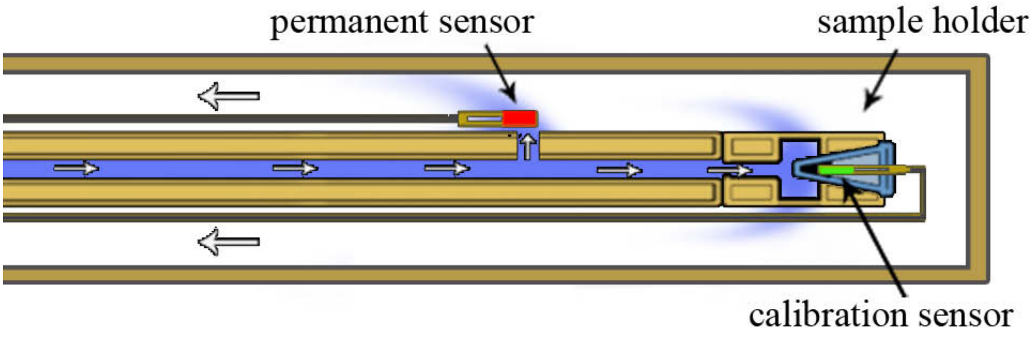

Figure 6.9: Arrangement of the temperature diodes around the sample space. The helium flow is illustrated in blue. The permanent sensor (red) can only measure the sample temperature indirectly. The calibration sensor (green) is installed in a sample dummy. During calibration measurements, both sensor signals are stored in a look-up table.

One of the challenges when designing the GRP cryostat was temperature measurement at the sample space. In other commercial systems, the sample holder is made of a highly heat–conducting material such as copper or sapphire. Typically, the temperature sensor is directly integrated into the copper block of the sample holder. Because of the high conductivity, the temperature at the sensor is very close to that of the sample and can be easily calibrated. However, to use the cryostat for fast MRX analyses, this type of sample holder is not possible. Because of the rapidly changing magnetic field at the end of the magnetization time, eddy currents can be induced in the copper that can then produce disruptive magnetic signals. In addition, the temperature sensor must be at least 4 cm from the sample in order to prevent interference with the analyses results. Hence, it is necessary to calibrate the temperature at the sample position prior to the actual MRX procedure in order to determine the temperature offset between the sample and the actual sensor position. In Figure 6.9, the positions of the permanent temperature sensor (red) and the calibration sensor (green) are shown. The calibration sensor is installed in an empty PCR tube used to house MNP samples. The permanent sensor is placed above a 1 mm diameter hole. Through this hole, the sensor receives a constant supply of helium coolant that also cools the sample. This setup allows direct detection of temperature changes because of changes in the helium flow. Without the connection hole, the permanent sensor would only measure the back-flowing helium gas, which is already partly heated at that point.

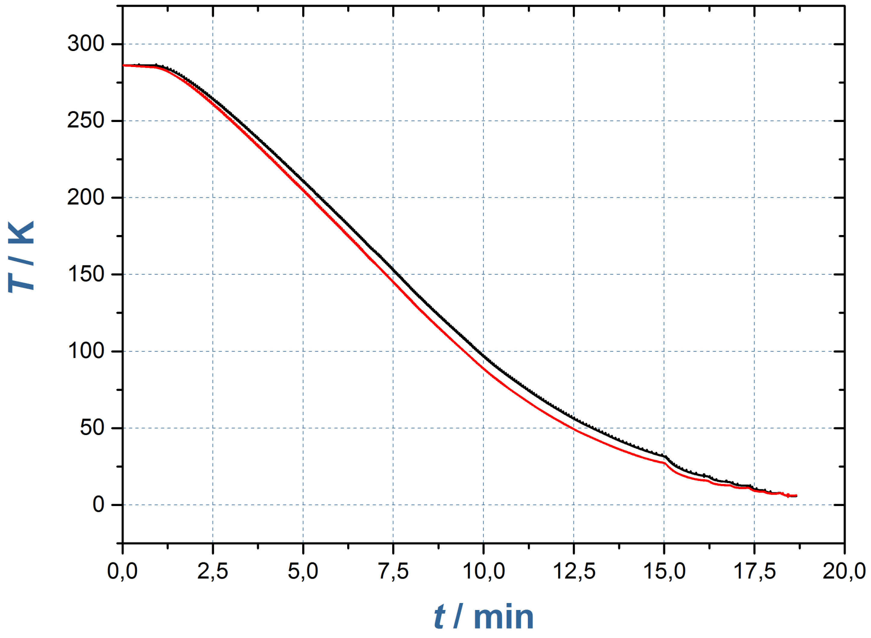

Figure 6.10: Typical temperature cool down sequence of the GRP cryostat for the calibration of the temperature at the sample position. The temperature of the diode which is four centimeter away from the sample space is displayed in black, while the sample temperature is displayed in red. In this sequence the system temperature falls from 290 K to 5 K in less than 20 minutes. During that time an offset between the sensor and the sample is visible.

Temperature Sweep

In order to cool the cryostat, the connected transfer tube (LLT) has an integrated needle valve to control the helium flow. The valve can be activated and set to a defined opening percentage by the temperature controller (Oxford Mercury ITC). The opening percentage in combination with the pressure in the helium vessel influences the cooling rate of the system. The temperature of the system increases after closing of the valve. Although the cryostat has an installed reflecting film, the thermal radiation of the outer tube is still sufficient enough to heat the system when the helium valve is closed. Therefore, after closing the valve, the system temperature slowly rises to approximately 250 K. To warm the system to ambient temperature, an additional heating coil was installed close to the sample chamber which can also be activated and controlled by the Mercury ITC. For the TMRX measurements a cool-down sweep with 7 % opening of the needle valve was used. The opening percentage was increased every time the system temperature falls below a predefined value. The resulting change in the slope of the temperature curve can be seen in Figure 6.10 below 30 K. The temperature at which the opening percentage is changed is defined in a text file that can be read by the LabVIEW interface.

Calibration Look-up Table and Repeatability

Because the sample temperature cannot be measured directly during MRX analyses, a calibration look-up table was implemented. This table links the temperature from the permanent sensor to the samples temperature. Each look-up table must be designed for a specific temperature sweep because changes in the helium valve opening only have a delayed effect on the sample and system temperature. In the course of the dissertation, look-up tables were created for a cool-down procedure from 290 K to 5 K and the reverse warm-up process. The temperature sweeps were repeated several times and the average temperature course was determined. The relationship between the temperature of the permanent sensor and the temperature at the sample space was saved in an ASCII–file. This file was accessed by the Mercury ITC LabVIEW interface and used to estimate the sample temperature. A comparison of the measured and estimated sample temperature allowed determination of the accuracy of the temperature estimation. Subtracting the real temperature data points from the estimated values provided the temperature residual function. According to this function, the difference in the estimated and real temperature values was of the order of ± 1 K. This temperature deviation is acceptable for the TMRX analyses performed in the present study. To improve the accuracy, it may be possible to install a sapphire sample holder that would conduct the temperature to the permanent sensor. Sapphire is often used in cryostat designs because it has a relatively high thermal conductivity of 42 W/mK [2] but does not produce eddy currents. Another option for improving the thermal accuracy would involve installation of a second permanent temperature sensor for measurement of the temperature of the returning helium gas. This approach would provide an improved temperature determination because the sample temperature could be narrowed down to the range between the temperatures of the incoming returning gases. Lastly, the sweep procedure could be improved; slower temperature changes have been shown to generally lead to a more accurate determination of the sample temperature.

---

[2] The thermal conductivity of copper for example is about 400 W/mK and of GRP it is about 0,3 W/mK.

6.3 Quantification of Magnetic Nanoparticles using TMRX in the Short Time Regime

Abstract 6.3 An example analysis using the GRP cryostat was performed to demonstrate its potential for the quantification of MNPs in biological samples. A Resovist dilution series previously analyzed using the MPMS (see also Chapter 4.3) was selected in order to be able to compare the results obtained with the two systems. Based on the differences in the spectra, the effects of the two time regimes on the TMRX analyses were considered. The detection limit of the short time regime was also investigated, and quantification of the dilution series was conducted. ■

Investigated Particles

DDM128, the precursor of the commercial contrast agent Resovist (Bayer Schering Pharma AG) was investigated. The MRI contrast agent consists of superparamagnetic iron oxide nanoparticles coated with carboxydextran. Resovist and its precursor particles are known to have a bimodal size distribution with particle core diameters ranging from 8 nm to 26 nm [90][23].

Preparation of Dilution Series Samples

The highly concentrated original DDM 128 solution (500 mmol) was diluted to prepare a series of solutions with defined iron contents. The original solution was diluted with distilled water in order to achieve the dilution steps with different concentrations. Finally, to 30 µL of the dilution 30 µL mannitol solution (containing 15 % mannitol) were added and then each sample was immobilized in a polycarbonate capsule via freeze drying.

MPMS TMRX Measurement Procedures

The measurements were performed using a Quantum Design SQUID magnetometer (MPMS-XL) with RSO measurements following the procedure described in Chapter 3.2.5.

6-Channel TMRX Measurement Procedures

The cool-down of the GRP cryostat was performed using the temperature sweep method described in Chapter 6.2.4. By constantly cooling the sample at approximately 0,1 K/s, the sample temperature changed from 290 K to 5 K within 30 min. During that time, the data acquisition system of the 6-channel SQUID system performed a continuous series of MRX analyses. The MRX procedure consisted of a magnetization time of 1 s, a delay time of 100 µs, and a measurement time of 1 s. Between each individual MRX analysis, a waiting time of 1 s was implemented to ensure complete relaxation of the sample. In total, 600 single MRX analyses were performed during the cool-down period.

6.3.1 TMRX Analysis of the Resovist Dilution Series

Both devices, the MPMS and the 6-channel SQUID system with the GRP cryostat, were used to perform temperature dependent relaxometry analyses on the same Resovist dilution series. The 6-channel SQUID system recorded the foremost magnetic field strength at the individual SQUID sensors in pT. First, the magnetic moment of the sample was calculated from the recorded field strength. To estimate the magnetic moment of the sample, the magnetic point dipole formula [31] was used. The SQUID sensor position ($\mathbf{r}_s$), the sample position relative to the center oft the magnetization coil ($\mathbf{r}_d$), and the orientation vector of the SQUID sensor ($\mathbf{n}$) were inserted into Equation 6.2:

$$B = \frac{\mu_0}{4\pi}\left(\frac{3\mathbf{n}((\mathbf{r}_s-\mathbf{r}_d)(\mathbf{r}_s-\mathbf{r}_d)^T)}{|\mathbf{r}_s-\mathbf{r}_d|^5} - \frac{\mathbf{n}^T}{|\mathbf{r}_s-\mathbf{r}_d|^3}\right)m. \tag{6.2}$$

After rearranging Equation 6.2, the estimated dipole moment (m) in Am^2 was obtained by inserting the measured magnetic field (B).

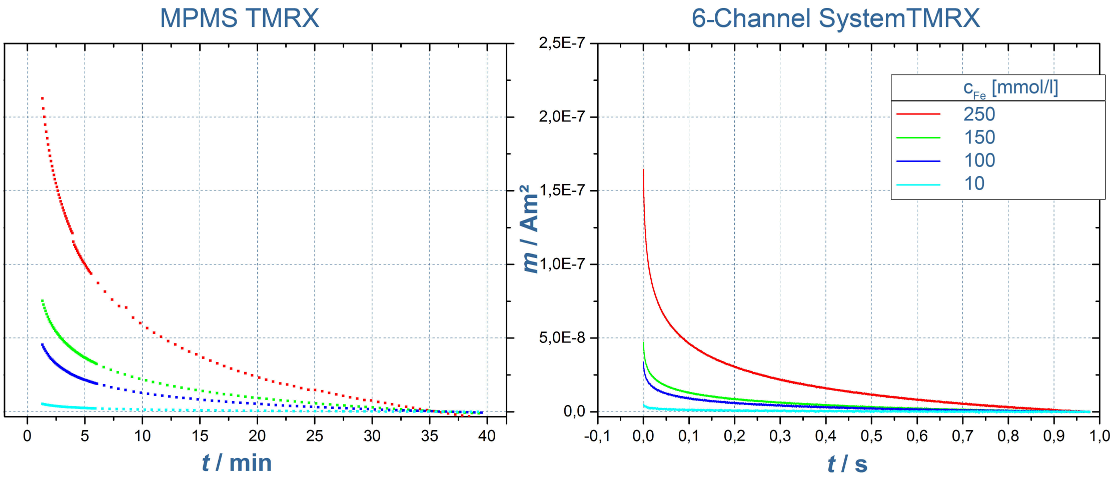

Figure 6.11: (Left): Relaxation measurement at 275 K for the most concentrated Resovist samples obtained using MPMS. The relaxation process in the long time regime took 40 min. (Right): Relaxation measurement performed using the GRP Cryostat in the 6-channel SQUID system. The measurement time in the short time regime only required 1 s. In both plots, a relationship between the amplitude change and the MNP concentration was observed. However, the decay of the relaxation after switching off the external field was significantly more pronounced in the short time regime.

A comparison of the relaxation signals obtained for each system is presented in Figure 6.11 for the short time regime of the 6-channel (right) and the long time regime of the MPMS (left). In both plots, the relaxation signals at 275 K for the Resovist samples of different concentration are displayed. From a technical point of view, the most prominent differences concerned the time scale and the sampling rate of the two systems. The MPMS measures in a long time regime of 40 min per relaxation, whereas the 6-channel SQUID system measures in the short time regime of 1 s per relaxation. In addition, the 6-channel system exhibited a higher sampling rate of 10000 data points per relaxation compared to 100 single RSO measurements for the MPMS.
Regarding the results for the Resovist samples shown in Figure 6.11, one feature was foremost apparent. The relaxation decay in the long time regime was slower than the decay in the short time regime. This difference could be attributed to the unequal measurement times of the two systems; at a defined temperature the measurement time window defines which core diameters of the particle distribution contribute to the relaxation signal. Despite these differences, the concentration was still

related to the signal amplitude in both types of spectra. This means that more concentrated samples exhibited stronger net magnetic moments.

In Figure 6.12, TMRX spectra from 5 K to room temperature obtained using both measurement systems are shown. On the right side of the Figure the influence of the higher sampling rate of the 6-channel SQUID system is illustrated with 600 single relaxation measurements equally distributed over the temperature spectrum. In contrast, the MPMS spectra shown on the left side of the figure consist of MRX analyses at 19 discrete temperatures and are therefore less smooth. The influence of the different sampling rates is particularly obvious for the most concentrated Resovist sample (red curve).

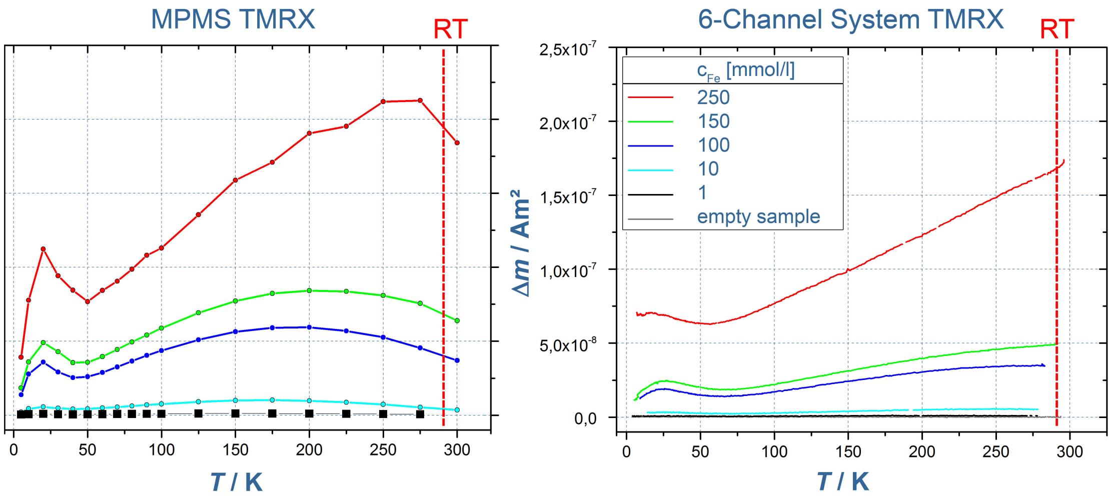

Figure 6.12: (Left) TMRX results for the Resovist dilution series performed using MPMS. (Right) TMRX results obtained using the GRP cryostat in the 6-channel SQUID system. The investigated temperature ranged from 5 K to room temperature for both systems. Both spectra were bimodal, with one peak at 25 K and a second peak at 200 K to 300 K. Notably, while the second peak was between 200 K and 250 K in the spectrum obtained via MPMS (left), it appeared near room temperature in the spectrum obtained using the 6-channel SQUID system (right).

The shape of the curves for the two sets of TMRX analyses are also clearly different. The MPMS spectra exhibit distinct signal peaks near 200 K – 250 K while the spectra obtained using the 6-channel SQUID system all display a constantly increasing signal as the temperature increased to room temperature. These different behaviors are attributed to the different measurement time regimes of the two systems. For TMRX analyses the measurement time window in combination with the relaxation time (τ) determines particle sizes that are detectable at a specific temperature. An MNP sample analyzed in the two different time regimes will therefore exhibit its strongest signal (T_{max}) at different temperatures (see also Figure 3.3 in Chapter 3.2). The signal maximum in the 6-channel spectra is assumed to be at or above room temperature. A comparison of the signal peaks obtained using the two systems is displayed in Figure 6.13. A constant offset can be seen for the signal peak of the MPMS spectra at approximately 200 K.

A second peak was also apparent at 25 K in the TMRX spectra obtained using both measuring systems. This second peak is attributed to the underlying fraction of the bimodal MNP sample with smaller diameters. In contrast to the quite obvious changes in the peak temperature for the fraction of the larger particles, the peak temperature for the fraction of smaller particles shifted only slightly (5 K) for the spectra obtained using the two measurement systems. The 5 K temperature difference is also attributed to the different time windows of the measurements. It should be noted that the overall TMRX spectra obtained using the 6-channel SQUID system (Figure 6.12, right) are less pronounced than the spectra obtained using the MPMS. This difference can also be attributed to the different time regimes and the associated detectable particle spectrum at each temperature. At a defined temperature, only the relaxations of a very distinct group of particles are detected in the long time regime of the MPMS. In the short measuring regime of the 6-channel system, on the other hand a broader range of particle sizes is detected at the same temperature, leading to an overall broader and less pronounced TMRX spectrum.

The changes in the peak intensities of the magnetic moments (*m*) are also generally smaller in the spectra obtained using the 6-channel system than those in the spectra obtained using the MPMS. This can be explained by the short magnetization time of only 1 s in the 6-channel system, during which specific types of MNPs are not fully magnetized. However, it is important to note that although the amplitude changes are generally smaller in the spectra obtained using the 6-channel system, the overall proportions of the peak amplitudes in the spectra for the different samples are the same, regardless of the analytical instrument. As was shown in Chapter 4.2, the signal ratio for the spectra of an unknown sample and a reference sample with known iron content can be used to quantify of the MNP content in the sample.

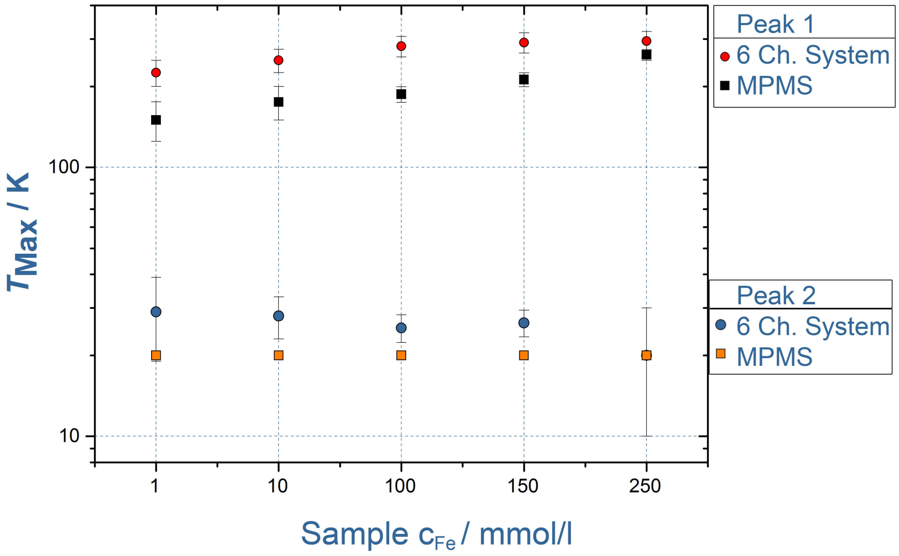

Figure 6.13: Peak temperatures for Resovist samples of different concentrations observed in the MPMS long time regime and 6-channel SQUID system short time regime. Each TMRX spectrum exhibited two distinct peak temperatures. The constant offset between the measured peak temperatures was attributed to the different time regimes.

6.3.2 Magnetic Nanoparticle Quantification Using the 6-Channel SQUID System

Quantification of the Resovist dilution series via TMRX in the short time regime of the 6-channel system was performed. To do so, the peak comparison method described in Chapter 4.2 was applied. The iron contents in the samples were also quantified via MPS analysis[51] and phenanthroline staining [78], and the results were compared to the estimated iron contents. The determined total iron content of the individual samples are plotted in Figure 6.14 as a function of the nominal iron content.

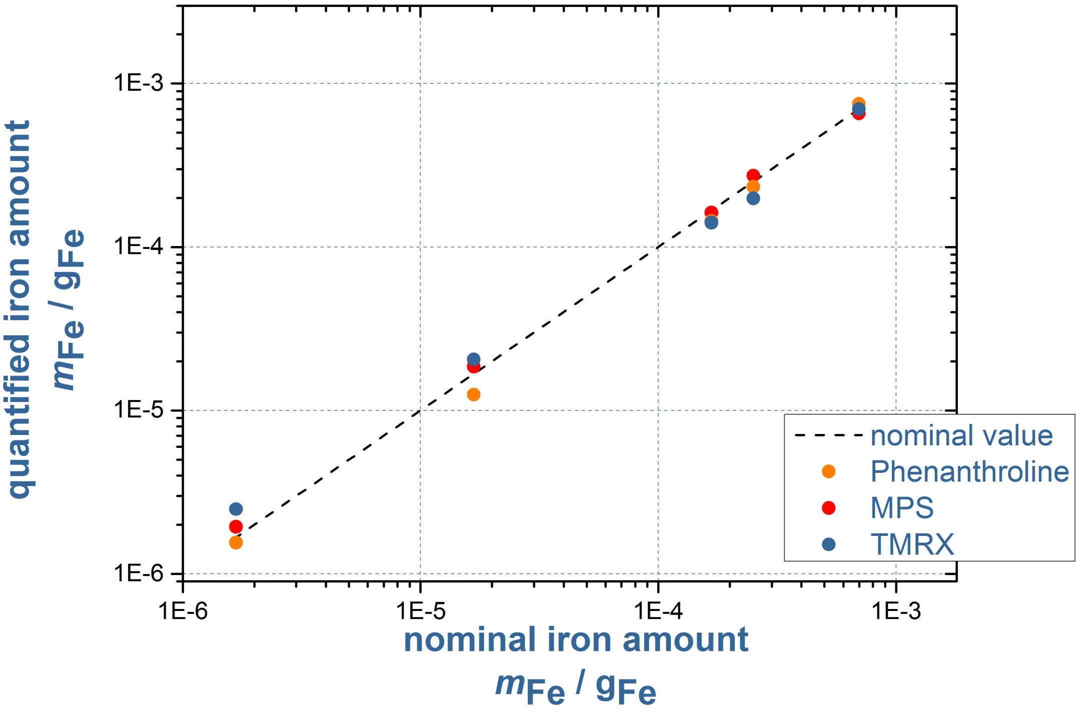

Figure 6.14: Nominal iron content in the different Resovist samples versus the iron content determined using three different methods. The concentration of iron in the samples varied by several orders of magnitude. The axis in the figure are therefore displayed logarithmically. The methods included phenanthroline staining [78], quantification via MPS [51], and quantification via TMRX peak comparison. While all three methods were generally capable of determining the iron content, they differed in their overall accuracy.

Figure 6.14 illustrates that the MNP concentration in the samples were successfully determined using all three methods. The quantification accuracy of the different methods did vary, however. The highest correlation with the nominal iron content was achieved using the MPS quantification method for this particular dilution series. The quantification analyses performed using the phenanthroline and TMRX methods suffered from slightly higher deviations. The detection limit for the TMRX quantification with the 6-channel system was estimated to be approximately 1 µg iron for the investigated Resovist samples. Below that iron concentration, the changes in the peak amplitude in the TMRX spectra were on the order of the background signal (ΔB_{noise}) of $4 \cdot 10^{-10}$ Am^2.
Next, the possible cause of the deviation of the TMRX quantification method was investigated. The applied peak comparison method requires that the maximum amplitude change in the TMRX spectra for all of the samples occurs at the same temperature. If the peak temperature changes because of particle interactions, this change must be describable and predictable using a mathematical model. For the presently investigated Resovist dilution series, it was assumed that the peak temperature was constant at room temperature in the TMRX spectra obtained in the short time

regime (Figure 6.12, right). However, it is possible that the maximum temperature changes actually occurred above room temperature and therefore not in the field of view. In addition, the TMRX spectra obtained using the MPMS in the slow time regime (Figure 6.12, left) revealed that the peak temperatures were not identical for all of the samples due to particle interactions. Although this effect would be less pronounced in the short time regime, it may have had an influence on the results.

Conclusion

TMRX measurements in the short time regime were demonstrated by measuring a dilution series of the known MRI contrast agent Resovist. The GRP cryostat was capable of cooling the samples in the temperature range from 5 K to room temperature. Compared to the long delay time of 1,5 min for the MPMS, the 6-channel SQUID system demonstrated a severely reduced delay of only 100 µs. The shorter delay time led to an overall reduced analysis time of 40 min to 60 min per sample, which is faster than the average MPMS measurement by a factor of ten. Due to the faster analysis time, more highly resolved TMRX spectra were obtained during the TMRX temperature sweeps.

The short analysis time for a single MRX measurement of 1 s for the 6-channel SQUID system also affected the shape of the obtained TMRX spectra compared to that of spectra obtained in the long time regime of the MPMS. A comparison of spectra obtained over for the same samples over the two time regimes revealed that the position of the peak temperature within the temperature spectrum was mainly affected. On the other hand, the linear relationship between the signal amplitude and the iron content remained the same and thus could be used to demonstrate the quantification capabilities of the measurement system.

Quantification of the MNP contents in samples with different concentrations was performed using the TMRX peak comparison method, and the results were compared to those obtained using other established methods. The TMRX quantification results were found to be valid, although there were slight deviations for the given samples. The deviations were within the accuracy range of the other methods and attributed to the specific behavior of the particles. The TMRX setup was capable of detecting up to 1 µg nanoparticle iron in the investigated Resovist samples.

The new measurement system therefore offered improvements in the measurement time and sample rate in combination with a solid quantification method. Hence, the potential applicability of the 6-channel SQUID system with the GRP cryostat for the determination of MNP concentrations in biological samples was successfully demonstrated.

6.4 Quantification of Magnetic Nanoparticles in Biological Tissues using TMRX in the Short Time Regime

Abstract 6.4 TMRX analysis and quantification of biological samples containing MNPs were investigated. The analyses were performed using the 6-channel SQUID system with the GRP Cryostat. Five different samples of mice liver tissue were investigated. The mice were injected with an aqueous iron oxide MNP contrast agent. Twenty-four hours after injection, the MNPs were accumulated in the livers of the mice. In order to quantify the MNP uptake, a small sample of tissue from each mouse was analyzed via magnetic particle spectroscopy (MPS) and TMRX. TMRX analysis using the 6-channel SQUID system was found to be suitable for determining the MNP content in the tissue samples; the results obtained via TMRX were in good agreement with those obtained via MPS. The TMRX spectra further revealed that the particle relaxation did not change when the MNPs were incorporated into the tissue. Therefore, it was concluded that no particle interactions or aggregation occurred during uptake. ■

Investigated MNP System

The rodents were given 50 µL of the MRI agent precursor containing iron oxide MNPs covered with a dextran coating (c_{Fe} =445 mmol/L). The magnetic core sizes of the particles ranged from 15 nm to 20 nm. In order to obtain a sample with an iron concentration comparable to the concentration in the tissue samples, the original solution was diluted with distilled water to c_{Fe} =4,5 mmol/L. Finally, to 100 µL of the dilution 50 µL mannitol solution (containing 15 % mannitol) were added, and the resultant solution was immobilized in a PCR capsule via freeze drying.

Preparation of biological Samples

Twenty–four hours after intravenous administration of 50 µL of the MRI contrast agent (445 mmol/L), four mice were sacrificed and their liver tissue harvested. For comparison, a single mouse that had not been exposed to magnetic nanoparticles was sacrificed and its liver harvested. The total quantities of liver tissue in the sample tubes used for the MPS and TMRX analyses are listed in Table 6.4.

Mouse ID	MPS tissue mass [g]	TMRX tissue mass [g]
Control	0.072	0.17
M79	0.027	0.12
M80	0.028	0.21
M82	0.043	0.12
M83	0.030	0.17

MPS Measurement Procedures

The samples were analyzed at 25 kHz using a drive field of 25 mT. The measurement time for each sample was 10 s at 300 K. Quantification of the MNP content was performed using the method of Löwa et al. [51].

6-Channel TMRX Measurement Procedures

Similar to the sequence described in Section 6.3, a temperature sweep was performed to cool down the samples. For this study, a faster cooling rate of 0,25 K/s was used, and the samples were cooled from 290 K to 5 K within 20 min. During that time, the data acquisition system of the 6-channel SQUID system continuously performed MRX analyses. The MRX procedure consisted of a magnetization time of 1 s, a delay time of 100 µs, and a measurement time of 1 s with a waiting time of 1 s between each individual MRX analysis to ensure complete relaxation of the sample. In total, 400 single MRX analyses were performed during the cool-down period. In order to increase the sensitivity of the system, a magnetization current of 1,5 A was applied, resulting in a magnetizing field of 4 mT.

TMRX Measurement of the biological samples

At room-temperature, the MNP reference sample already exhibited a relaxation behavior within the measurement time of one second. During the cool-down process, the relaxation amplitude in the spectra of the MNPs changed due to the longer relaxaton times of the particles. The amplitude changes for the spectra of the reference MNP sample are displayed in Figure 6.15 (pink line) for each temperature. The peak temperature, which exhibited the strongest relaxation amplitude (Δm), was observed at 160 K. Unlike the previously described samples (e.g., Resovist, see Chapter 6.3) the TMRX spectrum of the MNPs contained only a single peak temperature, indicating that the particle sample consisted of a monomodal size distribution. For this sample, the noise level was in the range of $1 \cdot 10^{-9}$ Am^2.

Subsequently, the 5 mice liver tissue samples were analyzed via TMRX. Four of the samples exhibited relaxation signals at room temperature. The fifth sample (Control, black line), however, showed no relaxation behavior. This result was expected because the mouse was not injected with the MNP contrast agent. The highest relaxation amplitude was exhibited by sample m80 (turquoise line in Figure 6.15). Like the spectrum of the reference sample, the spectrum of this sample exhibited a pronounced temperature peak near 160 K with an amplitude (Δm) of $1{,}35 \cdot 10^{-8}$ Am^2. The TMRX spectra for samples m79, m82, and m83, on the other hand, only contained less–pronounced temperature peaks at 160 K. Nevertheless, a decrease in the amplitude change was clearly visible below 150 K for all of the analyzed MNP samples. Similar to the reference sample, the TMRX spectra of the biosamples exhibited a noise level in the range of $1 \cdot 10^{-9}$ Am^2 or less. However, a comparison of the noise levels of the individual samples revealed that sample m80, had a significantly lower noise level than the others. This difference can be attributed to external sources of

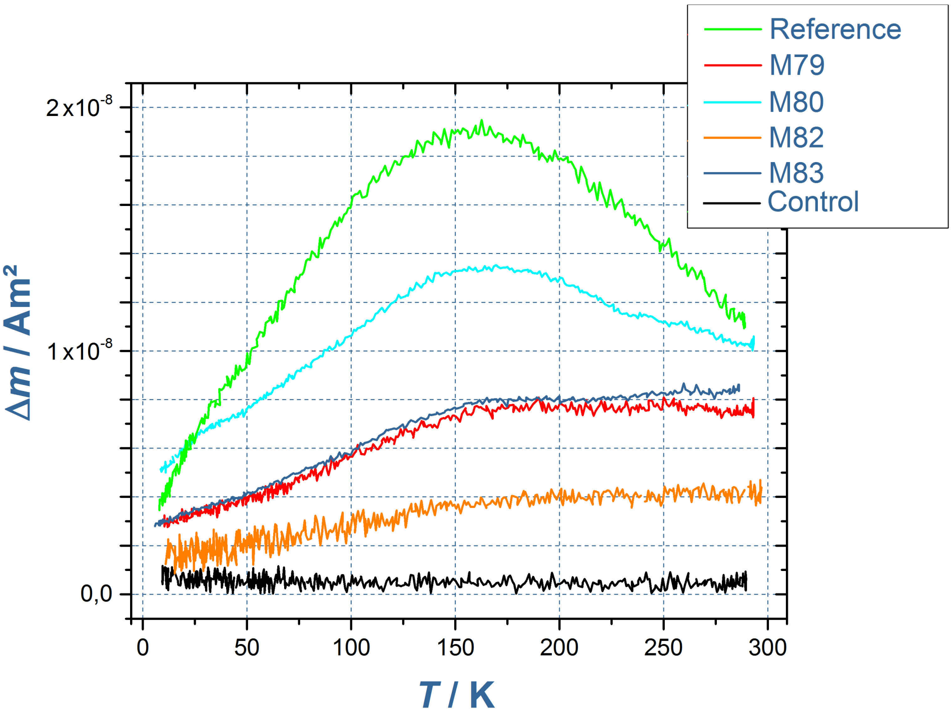

Figure 6.15: TMRX spectra of five different mice liver samples and a freeze–dried reference sample. The measurements were performed using the 6-channel SQUID system with a GRP Cryostat. The amplitude changes at each temperature for temperatures ranging from 5 K to 290 K are displayed. All of the mice liver samples with administered MNPs exhibited temperature depending relaxation signals. The highly concentrated samples and the reference sample exhibited a signal peak at 150 K to 170 K. The liver from the control mouse (black line) was not exposed to nanoparticles and did not exhibit a significant TMRX signal.

disturbance that affect the sensitive SQUID sensors. The measurement setup was shielded against most high frequency electromagnetic waves that are typically emitted from different power supply units, e.g., the power supply unit for the laptop used with the system. It was, however, not possible to completely remove the physical vibrations of the vacuum pump, which was directly connected to the GRP Cryostat. The quality of the vibration decoupling was different for each sample. It is assumed that this difference is the main source of the different noise levels observed in the spectra of the individual samples.

TMRX Quantification compared to MPS and MRX

Next, the TMRX analysis results obtained using the 6-channel system were used to determine the iron contents in the biosamples by employing the peak comparison method described in Chapter 4.2. While the more highly concentrated samples (m83, reference) had a clear peak temperature near 160 K, the samples with lower concentrations of MNPs exhibited a plateau above 150 K. The total iron content in the biosamples was determined by comparing their amplitude change at 160 K with the amplitude change of the reference sample. The relative iron concentration per gram tissue was obtained by normalizing the total iron content to the mass of each individual sample. The results are displayed in Figure 6.16. The quantification error was defined by the variance in the TMRX spectrum for each sample and the variance in the TMRX spectrum of the reference sample. These quantification errors are displayed as error bars on the TMRX values in Figure 6.16 (blue bars).

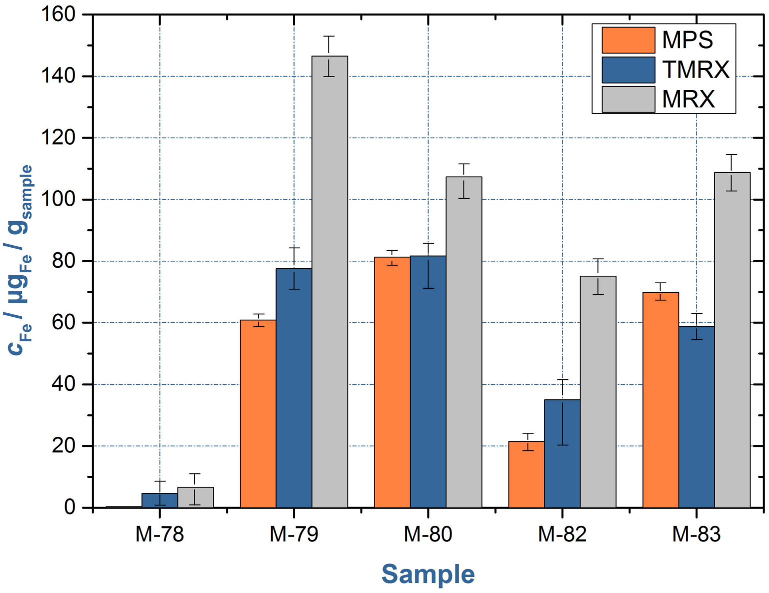

Figure 6.16: Quantification results for an MPS analysis (orange) compared to those obtained via TMRX (blue) and MRX (gray) at room temperature. The peak comparison method described in chapter 4.2 was used for the TMRX analysis. The iron contents determined using MPS and TMRX matched, although their confidence intervals did not always overlap. The deviation is attributed to the different sample volumes (see Table 6.4). Quantification via MRX at room temperature overestimated the MNP amount.

A comparison of the values determined for the relative iron contents via TMRX and MPS reveal that they were in good agreement. The biosamples used for the TMRX analyses where obtained from the same rodents as the biosamples used for the MPS analyses. However, the sample tubes used for the MPS analyses contained less tissue than the tubes used for TMRX analyses (see Table 6.4).

The deviations in the determined iron contents are assumed to be attributed to the different sample volumes.

In addition to the MPS analyses, quantification via room temperature MRX [96] was also performed. Particularly for the highly concentrated samples, the amplitude change at room temperature was different from the Δm value at 160 K. It can be seen in the TMRX spectrum shown in Figure 6.15, that the Δm values of the reference sample at room temperature and the peak temperature were approximately $1{,}1 \cdot 10^{-8}$ Am^2 and $1{,}9 \cdot 10^{-8}$ Am^2, respectively. It can be seen in Figure 6.15 that this difference between the Δm values at 160 K and 290 K was not visible for the samples with lower concentrations (m82, m83, and m79). Quantification based on the Δm value at room temperature therefore leads to a severe overestimation of the MNP concent in the samples (see Figure 6.16).

Finally, quantification via TMRX with the MPMS was attempted. Due to the limited sample volume and the long delay time, the resulting TMRX spectra where very close to the detection limit, and quantification was not possible (see Figure 9.16 in the Appendix).

Conclusion

Quantification via TMRX using the 6-channel SQUID system was presented, and the results were compared to those obtained using established quantification methods. The TMRX spectra of the biosamples revealed that the strongest amplitude change occurred at a peak temperature of 160 K. Therefore, quantification using the peak comparison method (see Chapter 4.2) was performed.

The determined iron concentrations were in accordance with the values obtained via MPS analyses. The quantification via room temperature MRX, on the other hand, led to overestimation of the iron concentrations in the liver samples. This result is attributed to the position of the peak temperature at 160 K for this particular type of MNP. For particles that have a peak temperature close to room temperature, e.g., Resovist (see Chapter 6.3), MRX quantification at room temperature is sufficient. TMRX analyses via MPMS were not sufficient to perform quantification because the overall signal quality of the biosamples was too low (see Figure 9.16 in the Appendix).

Thus, the new measurement setup with the GRP Cryostat in the 6-channel SQUID system offers a feasible method for quantification of MNP concentrations via TMRX. This method is attractive because it enables the analysis of larger biosamples, requires shorter delay times, provides overall faster TMRX results, and has the ability to depict changes in MNP signals due to particle interactions and aggregation. It is therefore a viable extension to existing measurement devices.

7. Conclusion

7.1 Summary and Conclusion

Summary

The scope of this work was to establish temperature dependent magnetorelaxometry (TMRX) measurements as quantification and characterization method for magnetic nanoparticles in biological tissue. This could be achieved by reaching several key milestones in the course of this dissertation. A commercial magnetic susceptometer (MPMS) was utilized to complete the first milestones, the development of a novel MNP quantification method, and the implementation of a consistent data analysis method.

With the MPMS, different MNP characteristics, like core diameter, size distribution and particle concentration were investigated via TMRX. Based on these measurements, a quantification method was developed for MNP in biological samples and the uptake of small MNP in cancer cells determined. The TMRX spectra measured with the MPMS also exhibited distinct alterations because of dipole–dipole interaction of the magnetic particles. With the measurement data that was collected, a simulation of the TMRX spectra could be performed. These measurements also formed the basis of the phenomenological dipole–dipole interaction model, which was developed in the course of the dissertation.

Another key milestone of this thesis was the optimization of the TMRX measurement time. Because of the magnetizing and measuring procedure TMRX measurements with the MPMS were only possible in a long time regime, i.e., the measurement of relaxations in the minute range. A single relaxation measurement took up to 40 minutes and a whole TMRX sequence took between 12 hours to 20 hours. In order to change the measurement procedure to the short time regime, a different magnetizing procedure was implemented in the MPMS. Nevertheless, a significant acceleration of the MPMS measurement was not possible, as internal background signals overshadowed the relaxation signal.

Therefore a measurement device was developed, capable of measuring relaxations in the microsecond range, i.e., the short time regime. For that purpose, an existing SQUID system was extended by a temperature controlled sample holder with magnetizing unit. The sample holder was therefore implemented in a helium flow cryostat, which was designed in the course of the thesis. With the cryostat TMRX spectra could be measured on a temperature range from room temperature down to 5 K. In addition, a LabVIEW interface was developed to control and measure the sample temperature. Finally, the uptake of MNP in biological samples that could not be quantified with the MPMS was quantified with the new TMRX device.

Conclusion

With the successfully established TMRX analysis a robust and reliable investigation method is now available. The developed measurement techniques offer not just a way to quantify MNP uptake in cells, but also to investigate alterations of the MNP signal in more detail. These signal alterations are of increasing importance for the current MNP development as they often occur in a biological environment. It is crucial for biomedical MNP applications that the particle's performance does not decrease when the MNP are exposed to biological tissue, which may happens because of aggregation, interaction or immobilization of the MNP. With the developed TMRX device a reliable and fast way to get a detailed view on the state of the MNP within the biological tissue is now available.

In addition, with the custom build measurement system, investigating larger series of biological samples with TMRX is now also feasible. This is important for the practical application of TMRX as MNP characterization method. Previously, TMRX analyses were only reasonable for a few, chosen MNP samples because of the long measurement time. The new system is now capable of providing a valuable contribution to the project related particle characterization procedures. It complements other established methods, like Magnetic Particle Spectroscopy or room temperature MRX, which do currently provide the main proportion of the standard particle characterization.

Lastly, the numerical simulation which was developed in the course of the thesis completes the TMRX analyses. Now, a more detailed analysis of the TMRX spectra is possible that also reveals information about the dipole–dipole interaction of the MNP sample. Furthermore, the novel dipole energy term is potentially applicable for other numerical simulations as well. This includes room temperature MRX but also alternating current (AC) field measurements like in Magnetic Particle Spectroscopy or Magnetic Particle Imaging.

Outlook

Our main suggestion for improvement of the TMRX measuring system concerns the cryostat itself. Through a redesign of the cryostat an important improvement concerning the sample change could be performed. Currently the design of the cryostat resembles a Dewar flask with only one single–sided opening. Hence, the cryostat has to be detached from the liquid helium transfer tube for every sample change. We therefore suggest a tube like cryostat design that provides a second opening with a retrievable sample rod. This would significantly decrease the delay time between the different sample measurements. In addition, it would increase the positioning accuracy of the magnetization coil beneath the SQUIDs.

Another improvement would be the additional installation of a thermally conducting sapphire heat bridge between the sample and temperature sensor. The heat bridge would reduce the thermal offset between the temperature sensor and sample, and therefore, increase the accuracy of the temperature measurement.

Although the fundamental principles of MNP interaction are already known nanoparticle interaction remains a research topic that attracts growing interest in the research community. The MNP performance for specific biomedical tasks crucially depends on the sensitive interaction between particles with each other or with the surrounding media. As biomedical applications are becoming more and more complex, these alterations of MNP within biological tissue become a relevant research question that needs to be addressed. Temperature dependent measurements, like the TMRX, will therefore become of increasing importance, as they are capable of presenting a detailed insight into particle interaction through *in vitro* experiments. In the future temperature dependent measurements will remain an essential tool to validate interaction models like the one presented here.

III

Appendices

8 **Magnetic Property Measurement System (MPMS)** 119
8.1 Description of the Magnetic Property Measurement System

9 **Construction** 125
9.1 6-Channel SQUID System for TMRX
9.2 6-Channel SQUID System: Additional Graphics and Pictures
9.3 Technical Drawings of the GRP Cryostat

8. Magnetic Property Measurement System (MPMS)

8.1 Description of the Magnetic Property Measurement System

TMRX measurement devices

For the measurements displayed in Section 4 a conventional SQUID magnetometer (MPMS-XL, Quantum Design, 8.1) was used. The Magnetic Property Measurement System (MPMS) excels through a temperature control system which is capable of reaching a holding temperature from 5 K to 350 K.

Figure 8.1: Quantum Design Magnetic Property Measurement System (MPMS)

SQUID

A superconducting quantum interference device (SQUID) is a very sensitive magnetometer used to determine smallest changes in the magnetic field. However, in the MPMS the SQUID does not detect the magnetic field from the sample directly. The sample rather moves through a system of superconducting detection coils which are connected to the SQUID. With this setup the current flowing in the detection coils is induced to the SQUID sensor. When a DC-current is introduced in the SQUID a detectable voltage can be measured. This voltage is strictly proportional to the current flowing in the SQUID pick up coil.

Second-Order Gradiometer

The particular alignment of the superconducting detection coils around the sample space is called a second order gradiometer. When SQUID pick up coils are aligned as a gradiometer a significant reduction in background drifts and signal noise caused by the relaxation of the superconducting magnet can be achieved. In a three coil gradiometer the upper coil and the bottom coil are bound clockwise with one turn whereas the center coil has two counter-clockwise turns. In this setup the flux change through relaxation of the superconducting magnet in the center coil will be canceled by the other two coils which experience the same flux change. However the signal produced by the sample will still be detectable as it is not constant on all three coils.

The magnetization unit

The sample chamber is surrounded by a superconducting five Tesla magnet which is constructed as a closed loop. As there is no electrical resistance in superconducting material, this setup allows running the magnet in a *persistent* mode. Once it has been set in this mode the magnet simply holds the magnetic field without the need of a constant external current. In order to change the current within the superconducting magnet the loop needs to be electrically opened. Therefore a small part of the magnets wire is wrapped around a heater. This is called the persistent-current switch. When the persistent switch is heated it loses its superconductivity and becomes normal again. In this state an electrical current may be induced. After the desired magnetic field is set, the heater is turned off and the persistent-current switch becomes superconducting again.

The RSO-Transport

The sample is positioned in the sample holder at the end of the sample rod which is then placed in the sample chamber through the airlock. The sample rod is held at the top by the RSO (Reciprocating Sample Option)-Motor. The RSO-Motor moves the sample sinusoidally through the pick up coils while measuring. A change of the sample's position comes along with a change of the flux in the system. The pick up coils induce a current into the superconducting circuit depending on the flux to which they are exposed. The position of the sample rod is tracked by a shaft encoder on the servo motor. To lower the signal to noise ratio, the sample is moved several times through the pick up coils and the measurements are averaged. The final RSO-measurement therefore consists of the absolute SQUID voltage at each position of the sample rod within the sample chamber. The incline of this bell shaped curve is then fitted and compared to the calibration curve of a palladium standard sample. This standard sample imitates a point dipole with an accuracy up to 0,1 %. For an exact fit the unknown sample should therefore have small spacial proportions of about 3 mm in diameter and 3 mm to 5 mm in height.

The Sample Rod

The MPMS sample rod is designed to carry standard polycarbonate capsules (PC capsules) with a capacity of 150 µL to 200 µL. The capsules are placed into a nonmagnetic straw at the end of the sample rod. The PC capsules may contain liquid or immobilized materials. For TMRX measurements only immobilized (freeze dried) nanoparticle samples were used.

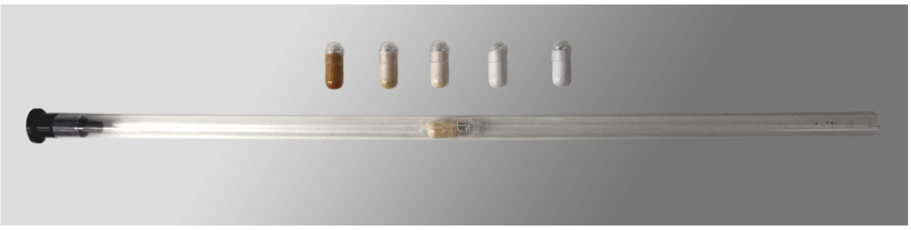

Figure 8.2: Above: A dilution series of freeze–dried nanoparticle solution in poly carbonate capsules. Below: A sample straw with an installed PC capsule.

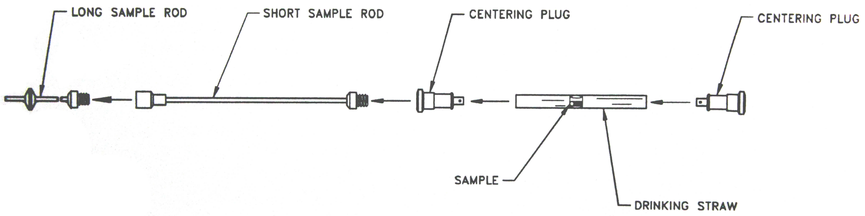

Figure 8.3: Sample rod and Sample straw setup (Picture from Manual [1])

After subtracting SQUID offset and drift the amplitude is determined by fitting a magnetic point dipole to the response curve. The signal to noise ratio can be improved through repeated RSO scanning. In the first 7 min the MPMS only performed single RSO scans (32 s per data point), after which RSO scans with three repetitions (140 s per data point) have been performed. Each relaxation measurement was executed at selected temperatures. The overall measurement time for one sample added up to about 12 h in total.

MultiVu Sequences

The MPMS MultiVu software is a Windows application to communicate with the MPMS. The software is capable of monitoring and calibration task and may perform different measurement procedures. Information about the instruments status may be displayed or logged in measurement files. SQUID measurements can be performed manually or through sequenced commands. These commands include a variety of system functions such as setting a certain magnetic field or changing the samples temperature.

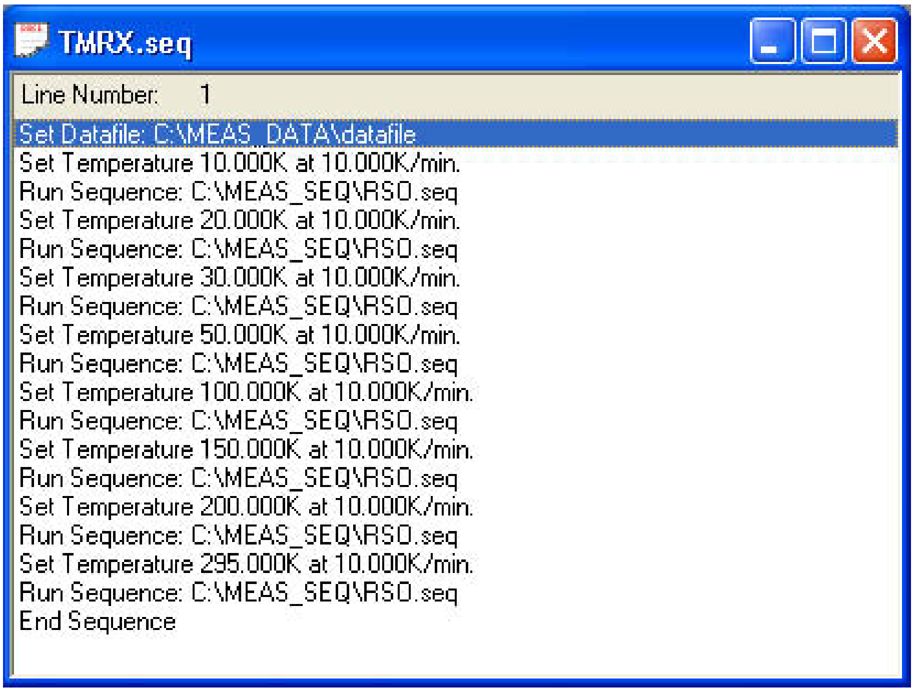

Line Number: 1

```
Set Datafile: C:\MEAS_DATA\datafile
Set Temperature 10.000K at 10.000K/min.
Run Sequence: C:\MEAS_SEQ\RSO.seq
Set Temperature 20.000K at 10.000K/min.
Run Sequence: C:\MEAS_SEQ\RSO.seq
Set Temperature 30.000K at 10.000K/min.
Run Sequence: C:\MEAS_SEQ\RSO.seq
Set Temperature 50.000K at 10.000K/min.
Run Sequence: C:\MEAS_SEQ\RSO.seq
Set Temperature 100.000K at 10.000K/min.
Run Sequence: C:\MEAS_SEQ\RSO.seq
Set Temperature 150.000K at 10.000K/min.
Run Sequence: C:\MEAS_SEQ\RSO.seq
Set Temperature 200.000K at 10.000K/min.
Run Sequence: C:\MEAS_SEQ\RSO.seq
Set Temperature 295.000K at 10.000K/min.
Run Sequence: C:\MEAS_SEQ\RSO.seq
End Sequence
```

Figure 8.4: Example of a typical MultiVu sequence: A measurement file was defined, different temperatures were set, and other sequences were called.

While working with the predefined measurement modi is quite easy with the MultiVu sequences other measurements require the usage of the External Device Control (EDC) Commands.

External Device Control

The *External Device Control* (EDC) language allows the user to communicate with the MPMS through a variate of short commands send through its *General Purpose Interface Bus* (GPIB). EDC commands are addressed directly to a device or sensor (e.g. the temperature sensor) in the system. This gives the user a more direct control over the magnetometer than it would be possible through the MultiVu sequences. Each EDC command triggers a specific task in the device it is send to. These tasks include sending and receiving data or changing the status of a component. It is important to understand that the MultiVu Sequence commands consists of EDC commands. While some of the MultiVu commands only consists of one EDC command, others may involve up to 10 or 20 different types. The current EDC activity of the MPMS can be watched in the MultiVu software under "Utilities>Diagnostics>GPIB>View GPIB Activity". With "GPIB>Send EDC commands" is also possible to send single EDC commands. If more complex command sequences are needed it is possible to include *.dll* files compiled by Borland Delphi. These *.dll* files can then be executed though the MultiVu script sequence. Another way to communicate with the MPMS magnetometer is to send the EDC commands directly through a Virtuall Intervace (LabVIEW).

Syntax: **SMP** (code)
where code = **0** turns the magnet power supply OFF
where code = **1** turns the magnet power supply ON
Initial: The power supply is OFF when
the MPMS Controller is initially started.
Purpose: Turns the magnet power ON and OFF

An example EDC Code is given above. The description is taken from the Quantum Design MPMS XL User Manual.

9. Construction

9.1 6-Channel SQUID System for TMRX

For TMRX analysis in the short time regime a magnetically shielded Dewar vessel was used. The vessel contained six SQUID (Superconducting QUantum Interference Device) sensors arranged around the center of the warm bore of the system. The horizontal warm bore of the 6-channel SQUID System measures 27 mm in diameter and 700 mm in length and is made out of a glass reinforced plastic. In order to reduce the magnetic background noise in the system a niobium shield is installed around the sample space. The superconducting niobium tube is 500 mm in length and 50 mm in diameter. The cold–warm distance between SQUID sensor and warm bore is 10 mm.

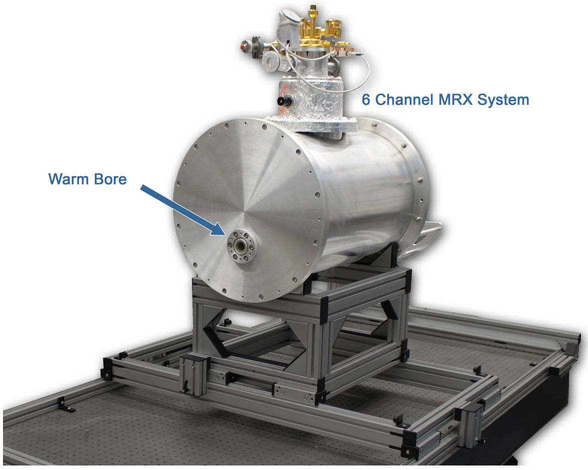

Figure 9.1: 6-channel SQUID system: A magnetically shielded Dewar vessel containing six SQUID sensors. On the front of the cylindrical Dewar the 27 mm wide opening of the warm bore can be seen. In the course of the dissertation a helium flow cryostat was designed to fit in the warm bore and to cool a biological sample for TMRX analyses.

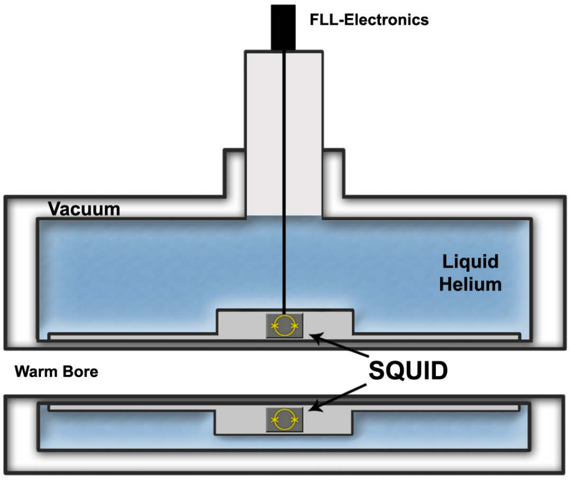

Figure 9.2: Illustration of the 6-channel SQUID system: The outer vacuum vessel surrounds the inner helium vessel. The warm bore is magnetically shielded by a niobium tube. The six SQUID sensors are operated with flux-locked-loop (FLL) electronics.

The 6-channel SQUID System was cooled down in the magnetically shielded room BMSR-2 at the PTB in order to minimize the residual field within the Dewar vessel. At the center of the warm bore a residual field of 100 nT was achieved. The Dewar vessel was manufactured by Fujihira Inc. in cooperation with the Kanawazawa Institute of Technology.

9.2 6-Channel SQUID System: Additional Graphics and Pictures

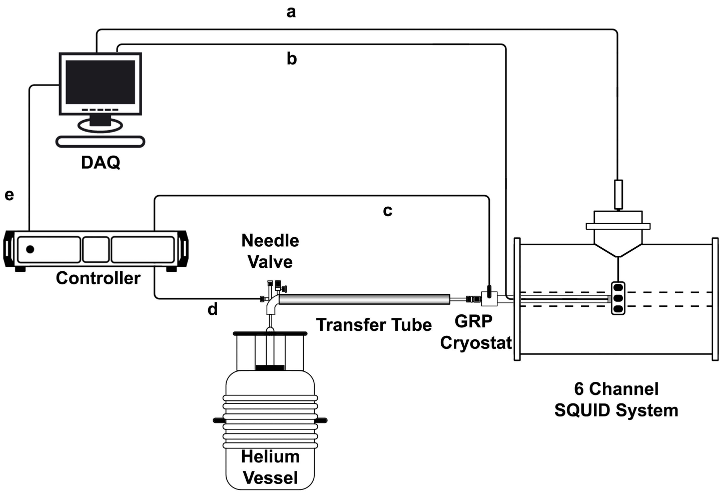
a
b
DAQ
e
c
Needle
Valve
Controller
d
Transfer Tube
GRP
Cryostat
6 Channel
SQUID System
Helium
Vessel

Figure 9.3: Experimental Setup: The data acquisition system (DAQ) reads out the relaxation signals (**a**) measured with the 6-channel SQUID system and controls the magnetizing coil(**b**). The temperature controller reads out the temperature sensor and controls the heating coil (**c**) in the glass reinforced plastics (GRP) Cryostat. In order to reach a certain temperature in the cryostat the temperature controller may open or close the needle valve(**d**) in the helium transfer tube. The measured temperature, the voltage of the heating coil, and the opening percentage of the needle valve are continuously transmitted to the DAQ System (**a**).

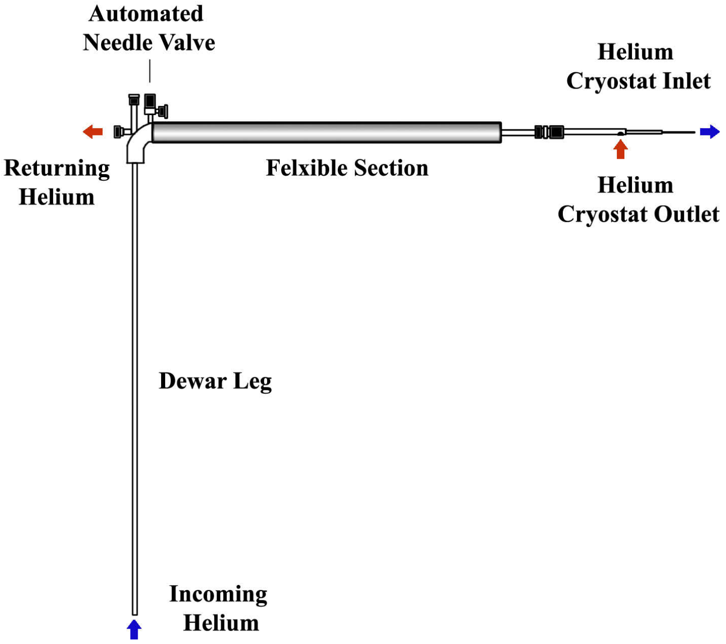
Automated
Needle Valve
Helium
Cryostat Inlet
Returning
Helium
Felxible Section
Helium
Cryostat Outlet
Dewar Leg
Incoming
Helium

Figure 9.4: Oxford Instruments low loss transfer tube (LLT): The helium coolant is taken up over the Dewar leg, which fits into our helium transport vessels. The GRP Cryostat is attached at the tip of the flexible section. At the tip, the helium cryostat inlet cools the GRP Cryostat and retrieves the warm helium gas. The returning helium is released over an outlet at the knee of the transfer tube. The stepper motor off the automated needle valve and its corresponding serial interface also located at the knee.

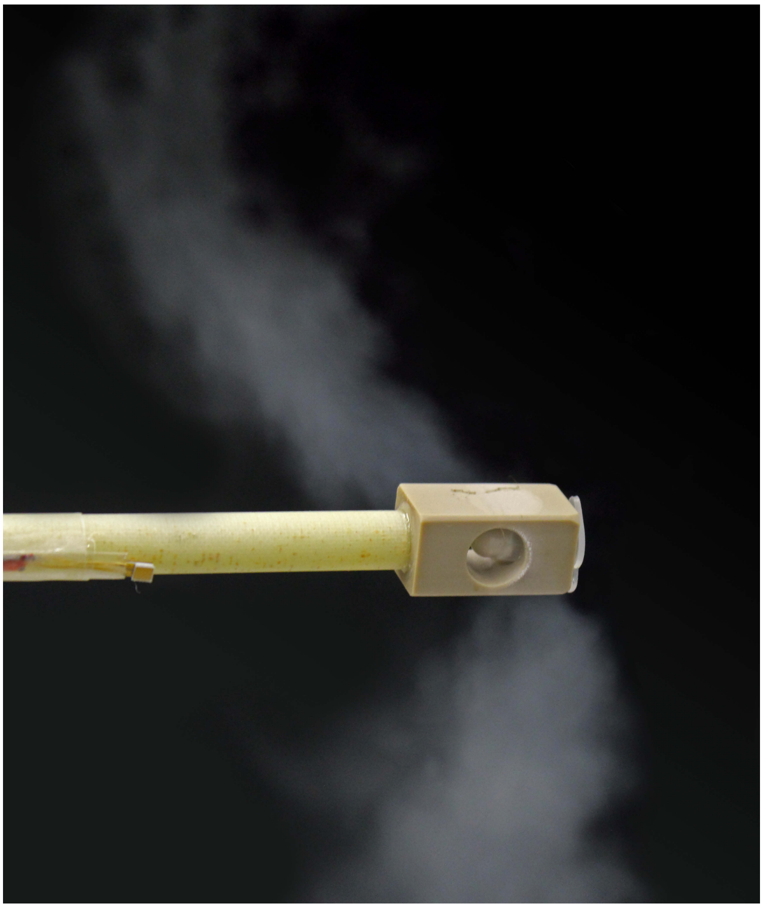

Figure 9.5: Close-up picture of the sample holder with an installed sample during the cooling process.

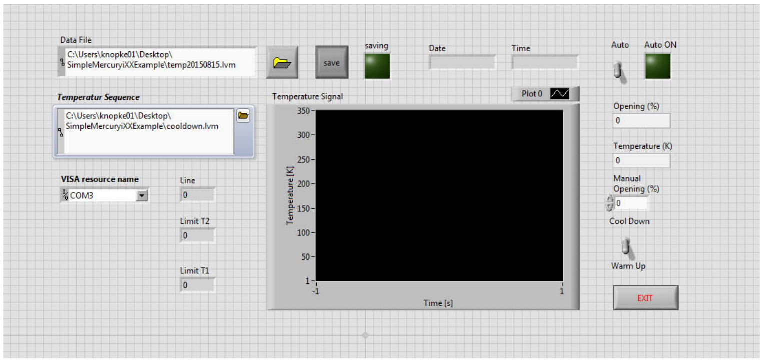

Data File: C:\Users\knopke01\Desktop\SimpleMercuryiXXExample\temp20150815.lvm

Temperatur Sequence: C:\Users\knopke01\Desktop\SimpleMercuryiXXExample\cooldown.lvm

VISA resource name: COM3

Line: 0

Limit T2: 0

Limit T1: 0

Opening (%): 0

Temperature (K): 0

Manual Opening (%): 0

Figure 9.6: The virtual interface (VI) for the Mercury ITC gives the user an easy method for sending commands and receiving data. The VI constantly measures the temperature of the permanent sensor with the option to save the data to an ASCII text file. The commands that can be sent to the ITC include manual opening of the helium needle valve to a defined percentage. In addition, an ASCII text file can be loaded in order to perform temperature sweeps. The VI allows to initiation of both cool–down and warm–up sweep procedures.

9.3 Technical Drawings of the GRP Cryostat

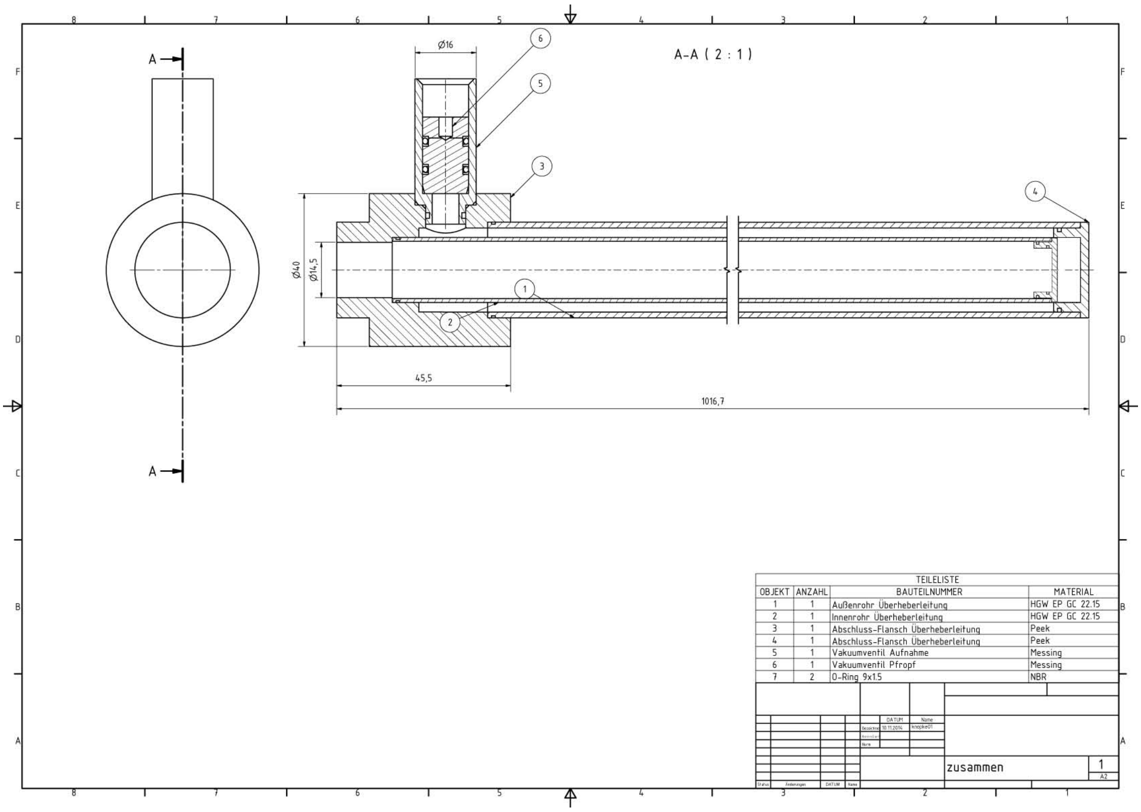
A-A (2 : 1)
A
A
Ø16
Ø40
Ø14,5
45,5
1016,7
1
2
3
4
5
6
DATUM
Name
10.11.2014
knopke01
Norm
zusammen
1
A2
Status
Änderungen
DATUM
Name

TEILELISTE			
OBJEKT	ANZAHL	BAUTEILNUMMER	MATERIAL
1	1	Außenrohr Überheberleitung	HGW EP GC 22.15
2	1	Innenrohr Überheberleitung	HGW EP GC 22.15
3	1	Abschluss-Flansch Überheberleitung	Peek
4	1	Abschluss-Flansch Überheberleitung	Peek
5	1	Vakuumventil Aufnahme	Messing
6	1	Vakuumventil Pfropf	Messing
7	2	O-Ring 9x1.5	NBR

Figure 9.7: General assembly drawing of the cryostat

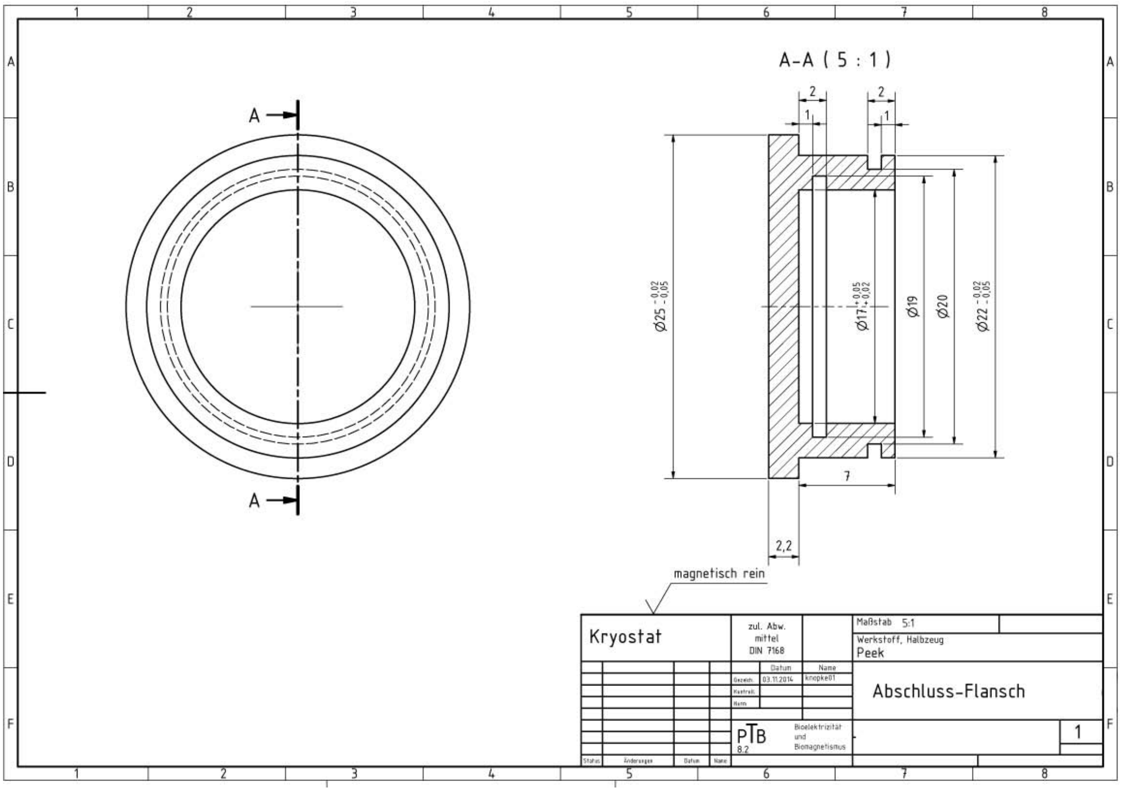
A-A (5 : 1)
A
A
2
2
1
1
Ø25 -0,02 -0,05
Ø17 +0,05 +0,02
Ø19
Ø20
Ø22 -0,02 -0,05
7
2,2
magnetisch rein
Kryostat
zul. Abw. mittel DIN 7168
Maßstab 5:1
Werkstoff, Halbzeug
Peek
Datum
Name
Gezeichn.
03.11.2014
knopke01
Kontroll.
Norm
Abschluss-Flansch
PTB 8.2
Bioelektrizität und Biomagnetismus
1
Status
Änderungen
Datum
Name

Figure 9.8: Rear end cover

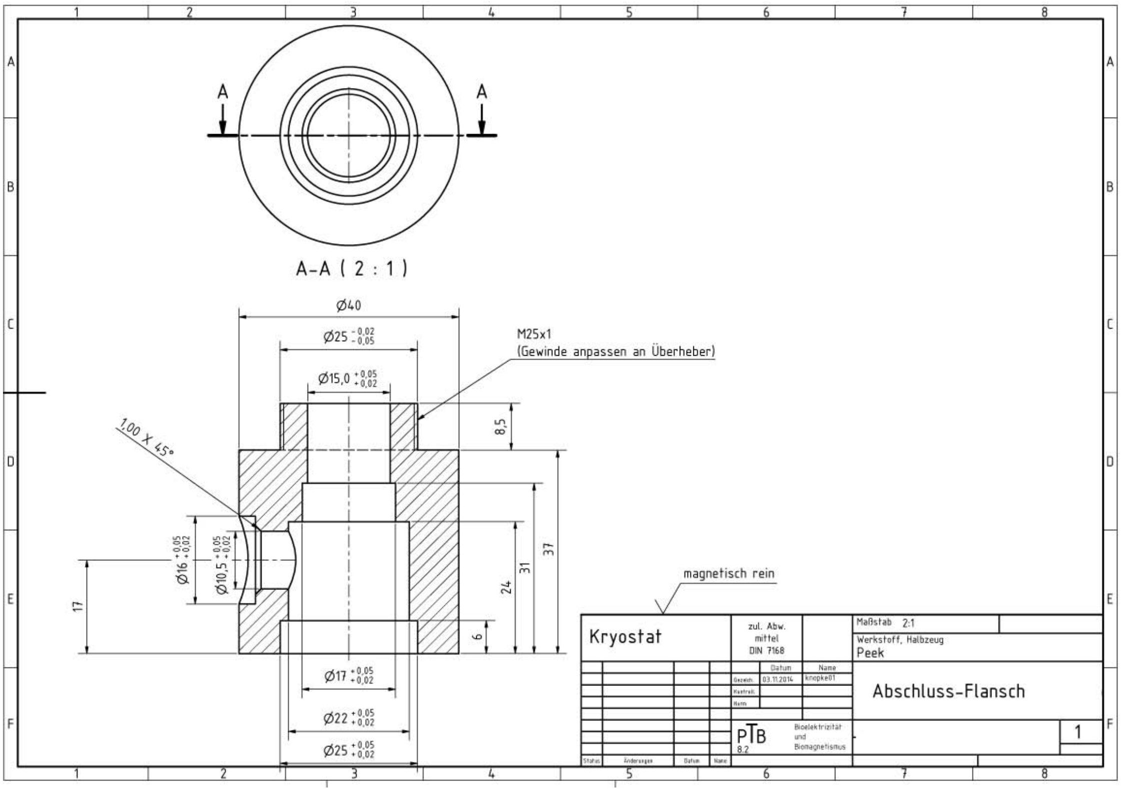
A
A
A-A (2 : 1)
Ø40
Ø25 $^{-0,02}_{-0,05}$
Ø15,0 $^{+0,05}_{+0,02}$
M25x1
(Gewinde anpassen an Überheber)
1,00 X 45°
8,5
37
31
24
6
17
Ø16 $^{+0,05}_{+0,02}$
Ø10,5 $^{+0,05}_{+0,02}$
Ø17 $^{+0,05}_{+0,02}$
Ø22 $^{+0,05}_{+0,02}$
Ø25 $^{+0,05}_{+0,02}$
magnetisch rein
Kryostat
zul. Abw.
mittel
DIN 7168
Maßstab 2:1
Werkstoff, Halbzeug
Peek
Datum
Name
Gezeich.
03.11.2014
knopke01
Kontroll.
Norm
Abschluss-Flansch
PTB
8.2
Bioelektrizität
und
Biomagnetismus
1
Status
Änderungen
Datum
Name
1
2
3
4
5
6
7
8
A
B
C
D
E
F

Figure 9.9: Front end flange

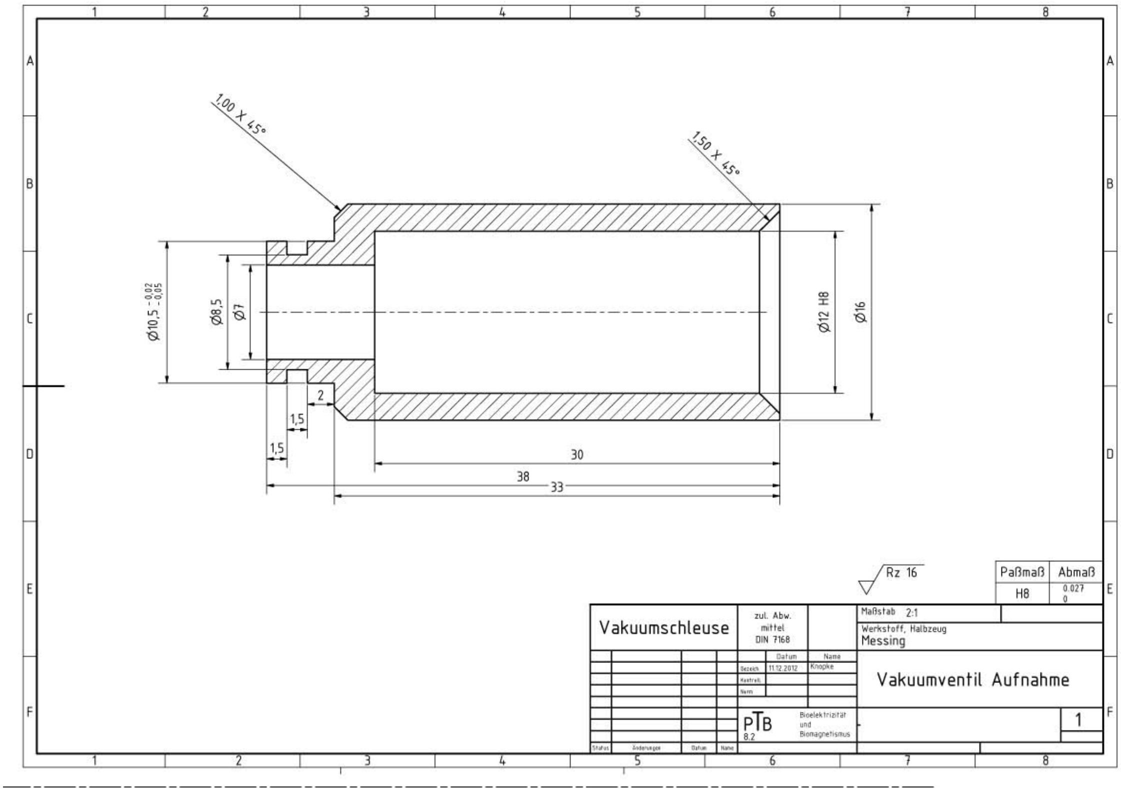
1,00 X 45°
1,50 X 45°
Ø10,5 $^{-0,02}_{-0,05}$
Ø8,5
Ø7
Ø12 H8
Ø16
2
1,5
1,5
30
38
33
Rz 16
Paßmaß
Abmaß
H8
0.027
0
Vakuumschleuse
zul. Abw.
mittel
DIN 7168
Maßstab 2:1
Werkstoff, Halbzeug
Messing
Datum
Name
Gezeich.
11.12.2012
Knopke
Kontroll.
Norm
Vakuumventil Aufnahme
PTB
8.2
Bioelektrizität
und
Biomagnetismus
1
Status
Änderungen
Datum
Name
1
2
3
4
5
6
7
8
A
B
C
D
E
F

Figure 9.10: Vacuum valve housing

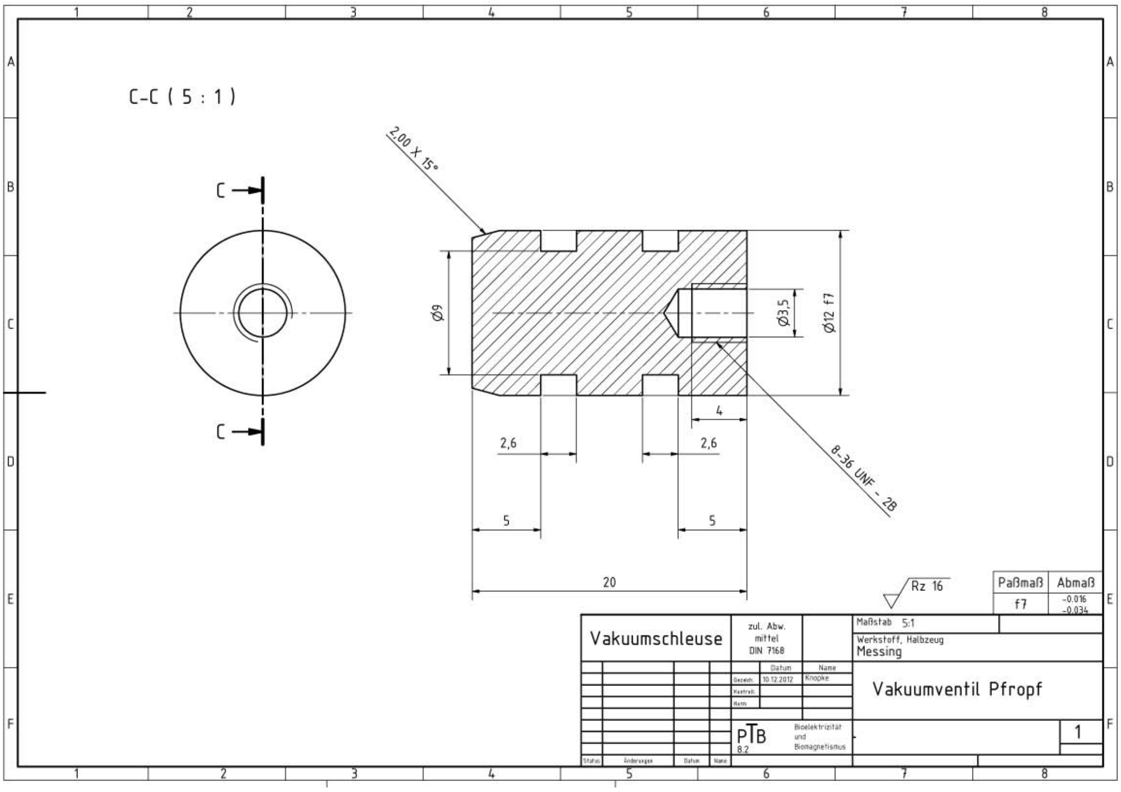
C-C (5 : 1)
C
C
2,00 X 15°
Ø9
Ø3,5
Ø12 f7
4
2,6
2,6
5
5
20
8-36 UNF - 2B
Rz 16
Paßmaß
Abmaß
f7
-0.016
-0.034
Vakuumschleuse
zul. Abw. mittel DIN 7168
Maßstab 5:1
Werkstoff, Halbzeug
Messing
Datum
Name
Gezeich.
10.12.2012
Knopke
Kontroll.
Norm
Vakuumventil Pfropf
PTB 8.2
Bioelektrizität und Biomagnetismus
1
Status
Änderungen
Datum
Name

Figure 9.11: Vacuum valve plug

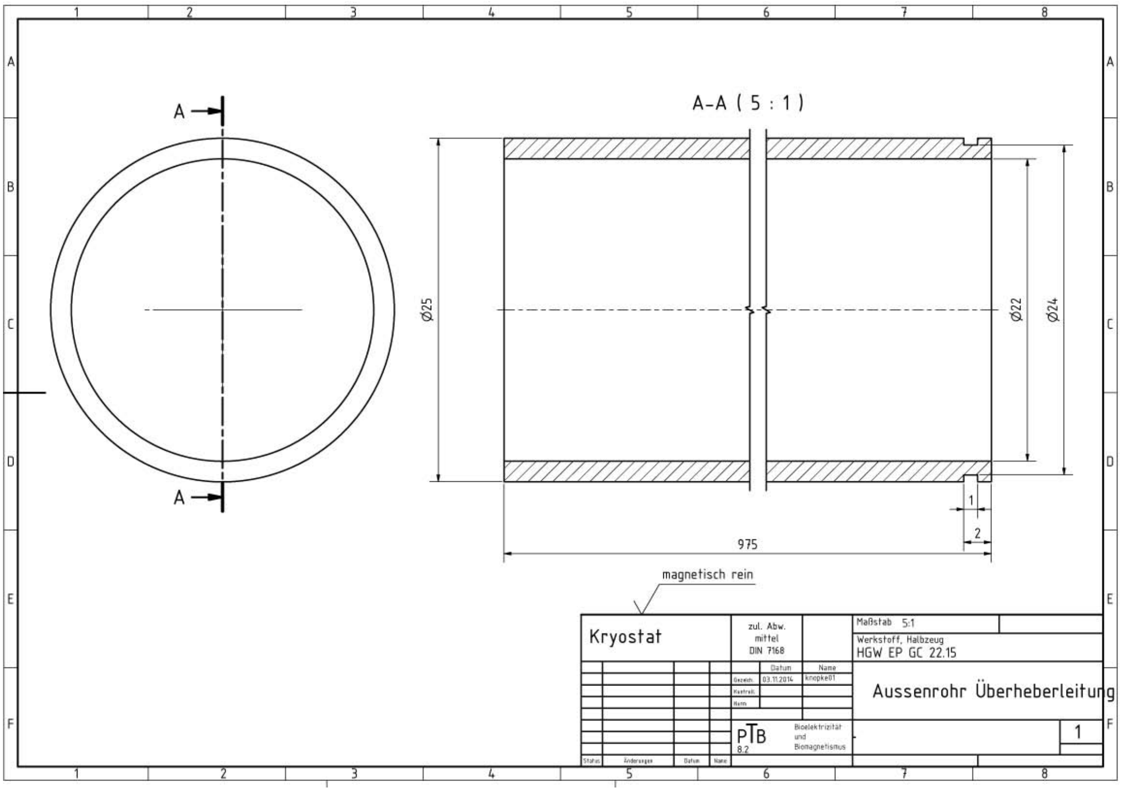
A
A
A-A (5 : 1)
Ø25
Ø22
Ø24
1
2
975
magnetisch rein
Kryostat
zul. Abw. mittel DIN 7168
Maßstab 5:1
Werkstoff, Halbzeug
HGW EP GC 22.15
Datum
Name
Gezeich.
03.11.2014
knopke01
Kontroll.
Norm
Aussenrohr Überheberleitung
PTB 8.2
Bioelektrizität und Biomagnetismus
1
Status
Änderungen
Datum
Name

Figure 9.12: Outer vaccum tube

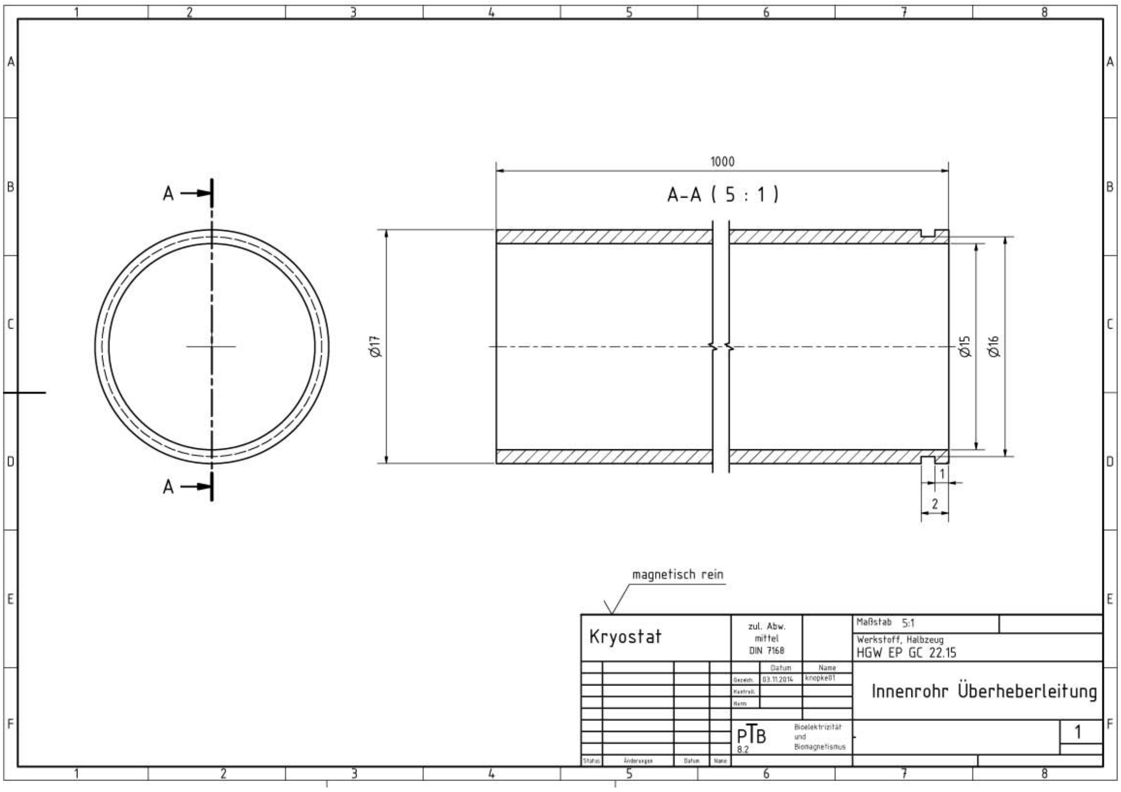
A
A
1000
A-A (5 : 1)
Ø17
Ø15
Ø16
1
2
magnetisch rein
Kryostat
zul. Abw.
mittel
DIN 7168
Maßstab 5:1
Werkstoff, Halbzeug
HGW EP GC 22.15
Datum
Name
Gezeich.
03.11.2014
knopke01
Kontroll.
Norm
Innenrohr Überheberleitung
PTB
8.2
Bioelektrizität
und
Biomagnetismus
1
Status
Änderungen
Datum
Name

Figure 9.13: Inner vaccum tube

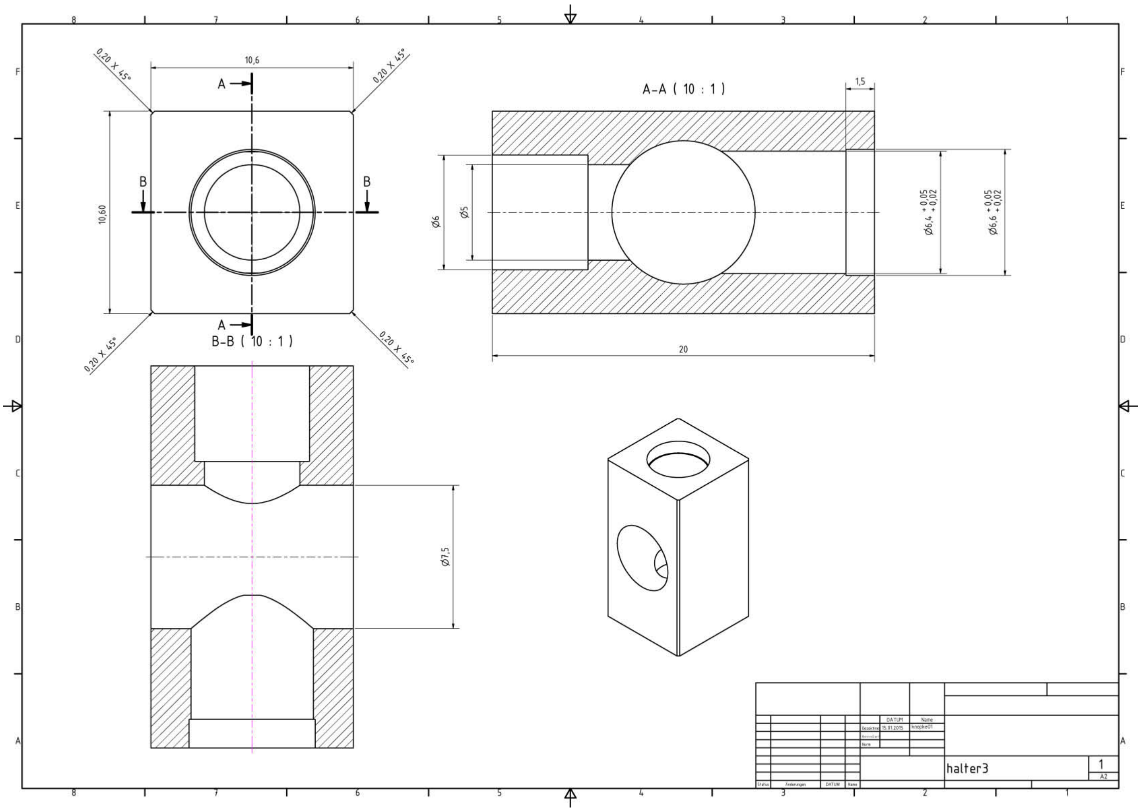
0,20 X 45°
10,6
0,20 X 45°
A
B
B
10,60
A
0,20 X 45°
0,20 X 45°
B-B (10 : 1)
A-A (10 : 1)
1,5
Ø6
Ø5
Ø6,4 +0,05 +0,02
Ø6,6 +0,05 +0,02
20
Ø7,5
DATUM
Name
Gezeichnet
15.01.2015
knopke01
Norm
halter3
1
A2
Status
Änderungen
DATUM
Name

Figure 9.14: Sample rod

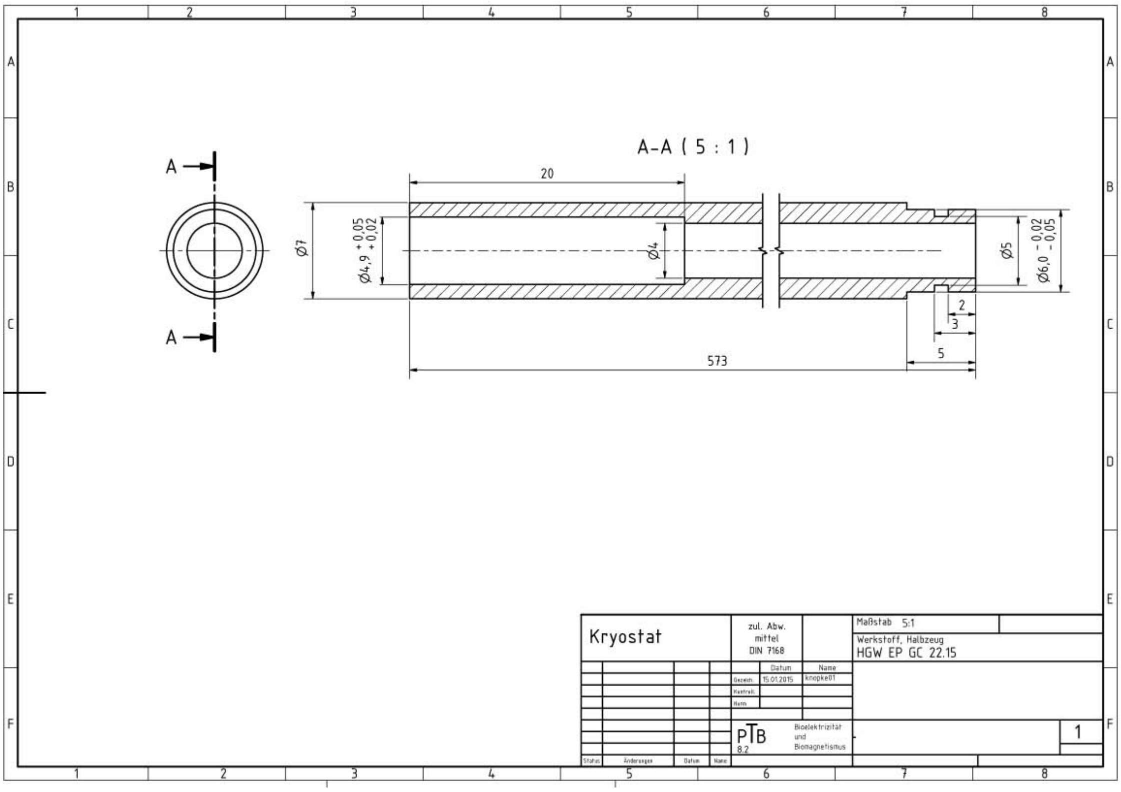
A-A (5 : 1)
A
A
20
Ø7
Ø4,9 +0,05 +0,02
Ø4
Ø5
Ø6,0 -0,02 -0,05
2
3
5
573
Kryostat
zul. Abw. mittel DIN 7168
Maßstab 5:1
Werkstoff, Halbzeug
HGW EP GC 22.15
Datum
Name
Gezeich.
15.01.2015
knopke01
Kontroll.
Norm
PTB 8.2
Bioelektrizität und Biomagnetismus
1
Status
Änderungen
Datum
Name

Figure 9.15: Sample holding

9.3.1 MPMS measurements from Chapter 6.4

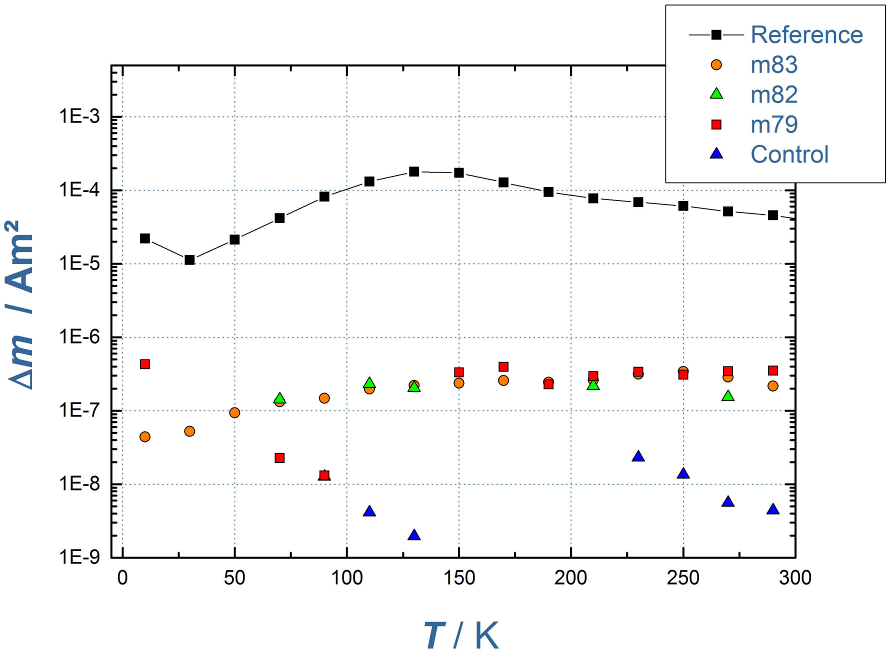

Figure 9.16: TMRX analyses of MNP samples presented in Chapter 6.4. The analyses were performed in the long time regime of the MPMS at B_{mag} =1 mT. The resulting TMRX spectra were not usable for quantification.

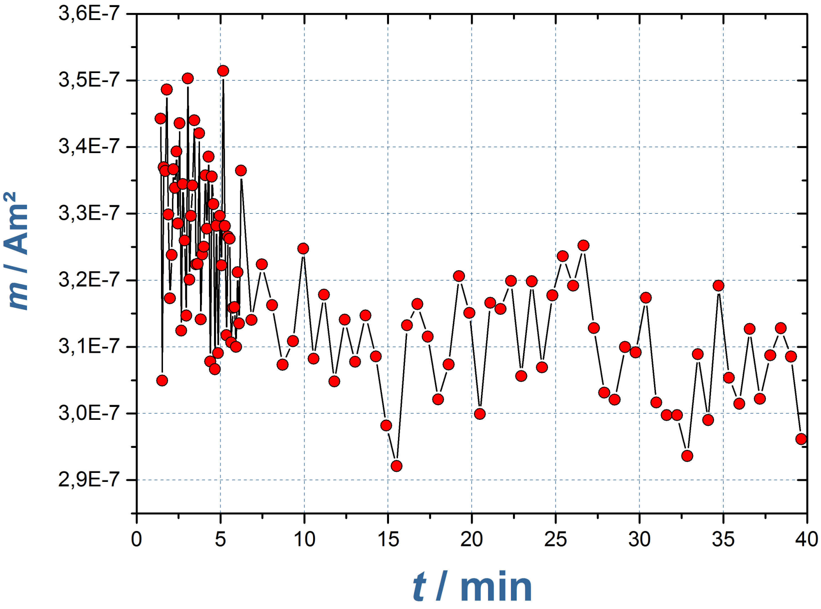

Figure 9.17: Relaxation data for the MNP samples (m82, T =290 K) presented in Chapter 6.4. The analyses were performed in the long time regime of the MPMS at B_{mag} =1 mT. Except for the reference sample, the signal to noise ratios in the relaxation curves were too low for interpretation.

9.3.2 Measurement and Fit Data from Chapter 5.3

Name	Mass $[mg]$	Iron per gram dry sample $[\frac{mg_{Fe}}{g_{sample}}]$	Total Iron $[mg_{Fe}]$	Relative Iron Amount
C6	46.7	0.16	0.0074	1
C5	44.1	0.79	0.0348	4.66
C4	42.6	3.98	0.169	22.69
C3	31.7	20.6	0.653	87.41
C2	50.8	45.5	2.3	307.0
C1	49.8	58.9	2.9	392.2
S	14.2	106	1.5	200.0

Table 9.1: Given parameters of the Endorem dilution series.

Name	d $[nm]$	$\sigma[-]$	Amplitude Factor	Estimated relative iron	Match $[\%]$
C6	8.25	0.25	2.72E-6	1	100
C5	8.25	0.27	1.19E-5	4.37	93
C4	8.50	0.27	5.80E-5	21.3	93
C3	8.75	0.27	2.28E-4	83.82	95
C2	9.75	0.27	5.46E-4	200.9	65
C1	9.75	0.30	5.92E-4	217.6	55
S	9.75	0.30	2.12E-4	77.94	39

Table 9.2: Fit parameters obtained by simulation without interaction energy. Iron amount estimated via peak comparison.

Name	d $[nm]$	$\sigma[-]$	D $[nm]$	Amplitude Factor	Estimated relative iron	Match $[\%]$
C6	8.00	0.283	60	0.01	1	100
C5	8.00	0.283	48	0.03	4.5	96
C4	8.00	0.283	38.9	0.14	23.5	103
C3	8.00	0.3	38.9	0.54	89.17	102
C2	8.00	0.31	25.3	1.49	248.33	80
C1	8.00	0.33	25.3	1.52	253.33	64
S	8.00	0.35	31.4	0.51	85.00	42

Table 9.3: Fit parameters obtained by simulation with approach A. Iron amount estimated comparison of the amplitude factor.

Name	d $[nm]$	$\sigma[-]$	D $[nm]$	Amplitude Factor	Estimated relative iron	Match $[\%]$
C6	8.00	0.266	45	0.0078	1	100
C5	8.00	0.266	43.28	0.035	4.49	96
C4	8.00	0.266	37.64	0.198	25.49	112
C3	8.00	0.266	32.7	0.929	119.1	136
C2	8.00	0.266	25.9	4.19	537.18	174
C1	8.00	0.266	22.57	6.03	773.08	197
S	8.00	0.266	22.5	2.24	287.18	143

Table 9.4: Fit parameters obtained by simulation with approach C. Iron amount estimated comparison of the amplitude factor.

Name	d $[nm]$	$\sigma[-]$	D $[nm]$	Amplitude Factor	Estimated relative iron	Match $[\%]$
C6	8.25	0.266	23.4	0.0078	1	100
C5	8.25	0.266	20.5	0.035	4.49	96
C4	8.25	0.266	15.78	0.198	25.49	112
C3	8.25	0.266	12.96	0.929	119.1	136
C2	8.25	0.266	9.33	4.19	537.18	174
C1	8.25	0.266	8.18	6.03	773.08	197
S	8.25	0.266	8.18	2.24	287.18	143

Table 9.5: Fit parameters obtained by simulation with approach D. Iron amount estimated comparison of the amplitude factor.

Bibliography

[1] Magnetic property measurementn systems: Mpms-xl options manual. *Quantum Design, San Diego*, 1999.

[2] R Ackermann, F Wiekhorst, A Beck, D Gutkelch, F Ruede, A Schnabel, U Steinhoff, D Drung, J Beyer, C Assmann, et al. Multichannel squid system with integrated magnetic shielding for magnetocardiography of mice. *Applied Superconductivity, IEEE Transactions on*, 17(2):827–830, 2007.

[3] Christoph Alexiou, Wolfgang Arnold, Roswitha J Klein, Fritz G Parak, Peter Hulin, Christian Bergemann, Wolfgang Erhardt, Stefan Wagenpfeil, and Andreas S Luebbe. Locoregional cancer treatment with magnetic drug targeting. *Cancer research*, 60(23):6641–6648, 2000.

[4] Christoph Alexiou, Roland Jurgons, Roswitha Schmid, Andrea Hilpert, Christian Bergemann, Fritz Parak, and Heinrich Iro. In vitro and in vivo investigations of targeted chemotherapy with magnetic nanoparticles. *Journal of Magnetism and Magnetic Materials*, 293(1):389–393, 2005.

[5] Daniel Baumgarten, Mario Liehr, Frank Wiekhorst, Uwe Steinhoff, Peter Münster, Peter Miethe, Lutz Trahms, and Jens Haueisen. Magnetic nanoparticle imaging by means of minimum norm estimates from remanence measurements. *Medical & biological engineering & computing*, 46(12):1177–1185, 2008.

[6] CP Bean and JD Livingston. Superparamagnetism. *Journal of Applied Physics*, 30(4):S120–S129, 1959.

[7] DV Berkov. Numerical calculation of the energy barrier distribution in disordered many-particle systems: the path integral method. *Journal of magnetism and magnetic materials*, 186(1):199–213, 1998.

[8] DV Berkov and NL Gorn. Susceptibility of the disordered system of fine magnetic particles: a langevin-dynamics study. *Journal of Physics: Condensed Matter*, 13(41):9369, 2001.

[9] J Bork, HD Hahlbohm, R Klein, and A Schnabel. The 8-layered magnetically shielded room of the ptb: Design and construction. In *Biomag2000, Proc. 12th Int. Conf. on Biomagnetism*, pages 970–73. Espoo, Finland, 2001.

[10] Christopher S Brazel. Magnetothermally-responsive nanomaterials: combining magnetic nanostructures and thermally-sensitive polymers for triggered drug release. *Pharmaceutical research*, 26(3):644–656, 2009.

[11] William Fuller Brown Jr. Thermal fluctuations of a single-domain particle. *Journal of Applied Physics*, 34(4):1319–1320, 1963.

[12] Robert F Butler and Subir K Banerjee. Theoretical single-domain grain size range in magnetite and titanomagnetite. *Journal of Geophysical Research*, 80(29):4049–4058, 1975.

[13] S Chakrabarti, SK Mandal, and S Chaudhuri. Cobalt doped γ-fe2o3 nanoparticles: synthesis and magnetic properties. *Nanotechnology*, 16(4):506, 2005.

[14] B Devika Chithrani, Arezou A Ghazani, and Warren CW Chan. Determining the size and shape dependence of gold nanoparticle uptake into mammalian cells. *Nano letters*, 6(4):662–668, 2006.

[15] WILLIAM THOMAS Coffey, DSF Crothers, JL Dormann, LJ Geoghegan, Yu P Kalmykov, JT Waldron, and AW Wickstead. Effect of an oblique magnetic field on the superparamagnetic relaxation time. *Physical Review B*, 52(22):15951, 1995.

[16] WILLIAM THOMAS Coffey, DSF Crothers, Yu P Kalmykov, ES Massawe, and JT Waldron. Exact analytic formula for the correlation time of a single-domain ferromagnetic particle. *Physical Review E*, 49(3):1869, 1994.

[17] Joan Connolly and Timothy G St Pierre. Proposed biosensors based on time-dependent properties of magnetic fluids. *Journal of Magnetism and Magnetic Materials*, 225(1):156–160, 2001.

[18] Sally J DeNardo, Gerald L DeNardo, Laird A Miers, Arutselvan Natarajan, Alan R Foreman, Cordula Gruettner, Grete N Adamson, and Robert Ivkov. Development of tumor targeting bioprobes (111in-chimeric l6 monoclonal antibody nanoparticles) for alternating magnetic field cancer therapy. *Clinical Cancer Research*, 11(19):7087s–7092s, 2005.

[19] J Dobson. Gene therapy progress and prospects: magnetic nanoparticle-based gene delivery. *Gene therapy*, 13(4):283–287, 2006.

[20] JL Dormann, D Fiorani, and E Tronc. On the models for interparticle interactions in nanoparticle assemblies: comparison with experimental results. *Journal of Magnetism and Magnetic Materials*, 202(1):251–267, 1999.

[21] S Dutz. Nanopartikel in der medizin. *Hamburg: Verlag Dr. Kovač*, 2008.

[22] D Eberbeck, S Hartwig, U Steinhoff, and L Trahms. Description of the magnetisation decay in ferrofluids with a narrow particle size distribution. *Magnetohydrodynamics*, 39:77–83, 2003.

[23] D Eberbeck, F Wiekhorst, S Wagner, and L Trahms. How the size distribution of magnetic nanoparticles determines their magnetic particle imaging performance. *Applied physics letters*, 98(18):182502, 2011.

[24] Dietmar Eberbeck and Heiko Ahlers. Glass like behavior of magnetization in frozen ferrofluids. *Journal of magnetism and magnetic materials*, 192(1):148–158, 1999.

[25] Dietmar Eberbeck and Lutz Trahms. Experimental investigation of dipolar interaction in suspensions of magnetic nanoparticles. *Journal of Magnetism and Magnetic Materials*, 323(10):1228–1232, 2011.

[26] Jun Ge, Evgenios Neofytou, Thomas J Cahill III, Ramin E Beygui, and Richard N Zare. Drug release from electric-field-responsive nanoparticles. *ACS nano*, 6(1):227–233, 2011.

[27] RK Gilchrist, Richard Medal, William D Shorey, Russell C Hanselman, John C Parrott, and C Bruce Taylor. Selective inductive heating of lymph nodes. *Annals of surgery*, 146(4):596, 1957.

[28] Bernhard Gleich and Jürgen Weizenecker. Tomographic imaging using the nonlinear response of magnetic particles. *Nature*, 435(7046):1214–1217, 2005.

[29] CG Granqvist and RA Buhrman. Ultrafine metal particles. *Journal of Applied Physics*, 47(5):2200–2219, 1976.

[30] Andrew D Grief and Giles Richardson. Mathematical modelling of magnetically targeted drug delivery. *Journal of Magnetism and Magnetic Materials*, 293(1):455–463, 2005.

[31] David Jeffrey Griffiths and Reed College. *Introduction to electrodynamics*, volume 3. prentice Hall Upper Saddle River, NJ, 1999.

[32] Mikkel Fougt Hansen and Steen Mørup. Models for the dynamics of interacting magnetic nanoparticles. *Journal of Magnetism and Magnetic Materials*, 184(3):L262–274, 1998.

[33] Stefan Hartwig. *Konzeption und Realisierung eines Messsystems für Grundlagenexperimente in der Niedrigfeld-Magnetresonanz*. PhD thesis, Ilmenau, Technische Universität Ilmenau, Diss., 2011, 2011.

[34] Sadek K Hilai, W Jost Michelsen, Jack Driller, and Edward Leonard. Magnetically guided devices for vascular exploration and treatment: Laboratory and clinical investigations 1. *Radiology*, 113(3):529–540, 1974.

[35] Nora Höfner. *Erweiterung eines Niedrigfeld NMR Messplatzes um eine eindimensionale Ortskodierung für die direkte Messung neuronaler Ströme*. PhD thesis, Berlin, Technische Universität Berlin, 2014, 2013.

[36] Alex Hubert and Rudolf Schäfer. *Magnetic domains: the analysis of magnetic microstructures*. Springer Science & Business Media, 1998.

[37] John David Jackson. *Klassische Elektrodynamik*. Walter de Gruyter, 2006.

[38] Petra E Jonsson. Superparamagnetism and spin glass dynamics of interacting magnetic nanoparticle systems. *Advances in Chemical Physics*, 128:191–248, 2004.

[39] T Jonsson, J Mattsson, C Djurberg, FA Khan, P Nordblad, and P Svedlindh. Aging in a magnetic particle system. *Physical review letters*, 75(22):4138, 1995.

[40] Andreas Jordan, P Wust, H Fähling, W John, A Hinz, and R Felix. Inductive heating of ferrimagnetic particles and magnetic fluids: physical evaluation of their potential for hyperthermia. *International Journal of Hyperthermia*, 25(7):499–511, 2009.

[41] Svenja Knappe, Tilmann H Sander, Olaf Kosch, Frank Wiekhorst, John Kitching, and Lutz Trahms. Cross-validation of microfabricated atomic magnetometers with superconducting quantum interference devices for biomagnetic applications. *Applied Physics Letters*, 97(13):133703, 2010.

[42] C Knopke, F Wiekhorst, D Eberbeck, S Wagner, and L Trahms. Analysis and quantification of aggregated nanoparticles by temperature dependent magnetorelaxometry. *BIOMEDICAL ENGINEERING-BIOMEDIZINISCHE TECHNIK*, 59:S654–S656, 2014.

[43] Christian Knopke, Frank Wiekhorst, Dietmar Eberbeck, Ines Gemeinhardt, Monika Ebert, Jörg Schnorr, Susanne Wagner, Matthias Taupitz, and Lutz Trahms. Quantification of magnetic nanoparticle uptake in cells by temperature dependent magnetorelaxometry. *Magnetics, IEEE Transactions on*, 49(1):421–424, 2013.

[44] T Koettig, P Weber, S Prass, and P Seidel. Design of a fibre reinforced plastic anticryostat for magnetorelaxometric measurements. *Proceedings of the ICEC*, 20, 2005.

[45] Jörg Kreuter, Renad N Alyautdin, Dimitri A Kharkevich, and Alexei A Ivanov. Passage of peptides through the blood-brain barrier with colloidal polymer particles (nanoparticles). *Brain research*, 674(1):171–174, 1995.

[46] J Lange, R Kötitz, A Haller, L Trahms, W Semmler, and W Weitschies. Magnetorelaxometry—a new binding specific detection method based on magnetic nanoparticles. *Journal of Magnetism and Magnetic Materials*, 252:381–383, 2002.

[47] Paul Langevin. Sur la théorie du mouvement brownien. *CR Acad. Sci. Paris*, 146(530-533), 1908.

[48] Sophie Laurent, Delphine Forge, Marc Port, Alain Roch, Caroline Robic, Luce Vander Elst, and Robert N Muller. Magnetic iron oxide nanoparticles: synthesis, stabilization, vectorization, physicochemical characterizations, and biological applications. *Chemical reviews*, 108(6):2064–2110, 2008.

[49] Wei Li, Sean Tutton, Anthony T Vu, Linda Pierchala, Belinda SY Li, Jerome M Lewis, Pottumarthi V Prasad, and Robert R Edelman. First-pass contrast-enhanced magnetic resonance angiography in humans using ferumoxytol, a novel ultrasmall superparamagnetic iron oxide (uspio)-based blood pool agent. *Journal of Magnetic Resonance Imaging*, 21(1):46–52, 2005.

[50] M Liebl, U Steinhoff, F Wiekhorst, J Haueisen, and L Trahms. Quantitative imaging of magnetic nanoparticles by magnetorelaxometry with multiple excitation coils. *Physics in medicine and biology*, 59(21):6607, 2014.

[51] Norbert Loewa, Frank Wiekhorst, Ines Gemeinhardt, Monika Ebert, Joerg Schnorr, Susanne Wagner, Matthias Taupitz, and Lutz Trahms. Cellular uptake of magnetic nanoparticles quantified by magnetic particle spectroscopy. *Magnetics, IEEE Transactions on*, 49(1):275–278, 2013.

[52] Antonio López, Lucía Gutiérrez, and Francisco José Lázaro. The role of dipolar interaction in the quantitative determination of particulate magnetic carriers in biological tissues. *Physics in medicine and biology*, 52(16):5043, 2007.

[53] Andreas S Lübbe, Christoph Alexiou, and Christian Bergemann. Clinical applications of magnetic drug targeting. *Journal of Surgical Research*, 95(2):200–206, 2001.

[54] Andreas Stephan Lübbe, Christian Bergemann, Winfried Huhnt, Thomas Fricke, Hanno Riess, Jeffery Walter Brock, and Dieter Huhn. Preclinical experiences with magnetic drug targeting: tolerance and efficacy. *Cancer research*, 56(20):4694–4701, 1996.

[55] Andreas Stephan Lübbe, Christian Bergemann, Hanno Riess, Folke Schriever, Peter Reichardt, Kurt Possinger, Michael Matthias, Bernd Dörken, Friedhelm Herrmann, Renate

Gürtler, et al. Clinical experiences with magnetic drug targeting: a phase i study with 4-epidoxorubicin in 14 patients with advanced solid tumors. *Cancer research*, 56(20):4686–4693, 1996.

[56] F Luchetti, B Canonico, M Della Felice, S Burattini, M Battistelli, S Papa, and E Falcieri. Hyperthermia triggers apoptosis and affects cell adhesiveness in human neuroblastoma cells. 2003.

[57] F Ludwig, S Mäuselein, E Heim, and M Schilling. Magnetorelaxometry of magnetic nanoparticles in magnetically unshielded environment utilizing a differential fluxgate arrangement. *Review of scientific instruments*, 76(10):106102, 2005.

[58] Frank Ludwig, Erik Heim, Sascha Mäuselein, Dietmar Eberbeck, and Meinhard Schilling. Magnetorelaxometry of magnetic nanoparticles with fluxgate magnetometers for the analysis of biological targets. *Journal of magnetism and magnetic materials*, 293(1):690–695, 2005.

[59] Klaus Maier-Hauff, Ronny Rothe, Regina Scholz, Uwe Gneveckow, Peter Wust, Burghard Thiesen, Annelie Feussner, Andreas von Deimling, Norbert Waldoefner, Roland Felix, et al. Intracranial thermotherapy using magnetic nanoparticles combined with external beam radiotherapy: results of a feasibility study on patients with glioblastoma multiforme. *Journal of neuro-oncology*, 81(1):53–60, 2007.

[60] Ph H Meyers, Fr Cronic, and Ch Nice Jr. Experimental approach in the use and magnetic control of metallic iron particles in the lymphatic and vascular system of dogs as a contrast and isotropic agent. *Am. J. Roentgenol., Radium Therapy Nucl. Med.*, 90, 1963.

[61] A Millan, A Urtizberea, NJO Silva, F Palacio, VS Amaral, E Snoeck, and V Serin. Surface effects in maghemite nanoparticles. *Journal of magnetism and magnetic materials*, 312(1):L5–L9, 2007.

[62] P Moroz, SK Jones, and BN Gray. Magnetically mediated hyperthermia: current status and future directions. *International Journal of Hyperthermia*, 18(4):267–284, 2002.

[63] Steen Mørup and Elisabeth Tronc. Superparamagnetic relaxation of weakly interacting particles. *Physical review letters*, 72(20):3278, 1994.

[64] Louis Néel. Théorie du traînage magnétique des ferromagnétiques en grains fins avec applications aux terres cuites. *Ann. géophys*, 5(2):99–136, 1949.

[65] Tobias Neuberger, Bernhard Schöpf, Heinrich Hofmann, Margarete Hofmann, and Brigitte Von Rechenberg. Superparamagnetic nanoparticles for biomedical applications: possibilities and limitations of a new drug delivery system. *Journal of Magnetism and Magnetic Materials*, 293(1):483–496, 2005.

[66] Robert C O'handley. *Modern magnetic materials: principles and applications*, volume 830622677. Wiley New York, 2000.

[67] Susana ICJ Palma, Marzia Marciello, Alexandra Carvalho, Sabino Veintemillas-Verdaguer, Maria del Puerto Morales, and Ana CA Roque. Effects of phase transfer ligands on monodisperse iron oxide magnetic nanoparticles. *Journal of colloid and interface science*, 437:147–155, 2015.

[68] Quentin A Pankhurst, J Connolly, SK Jones, and J Dobson. Applications of magnetic nanoparticles in biomedicine. *Journal of physics D: Applied physics*, 36(13):R167, 2003.

[69] D Parker, V Dupuis, F Ladieu, J-P Bouchaud, E Dubois, R Perzynski, and Eric Vincent. Spin-glass behavior in an interacting γ-fe 2 o 3 nanoparticle system. *Physical Review B*, 77(10):104428, 2008.

[70] Daniel P Perl and Paul F Good. Comparative techniques for determining cellular iron distribution in brain tissues. *Annals of neurology*, 32(S1):S76–S81, 1992.

[71] Ph Prené, E Tronc, J-P Jolivet, J Livage, R Cherkaoui, M Nogues, J-L Dormann, and D Fiorani. Magnetic properties of isolated γ-fe 2 o 3 particles. *Magnetics, IEEE Transactions on*, 29(6):2658–2660, 1993.

[72] Sharon K Pulfer and James M Gallo. Targeting magnetic microspheres to brain tumors. In *Scientific and clinical applications of magnetic carriers*, pages 445–455. Springer, 1997.

[73] Anna Radomski, Paul Jurasz, David Alonso-Escolano, Magdalena Drews, Maria Morandi, Tadeusz Malinski, and Marek W Radomski. Nanoparticle-induced platelet aggregation and vascular thrombosis. *British journal of pharmacology*, 146(6):882–893, 2005.

[74] NY Rapoport, DA Christensen, HD Fain, L Barrows, and Z Gao. Ultrasound-triggered drug targeting of tumors in vitro and in vivo. *Ultrasonics*, 42(1):943–950, 2004.

[75] E Romanus, T Koettig, S Prass, F Schmidl, J Heinrich, M Gopinadhan, DV Berkov, CA Helm, W Weitschies, P Weber, et al. Energy barrier distributions of maghemite nanoparticles. *Nanotechnology*, 18(11):115709, 2007.

[76] AN Rusetski and EK Ruuge. Magnetic fluid as a possible drug carrier for thrombosis treatment. *Journal of Magnetism and Magnetic Materials*, 85(1):299–302, 1990.

[77] EK Ruuge and AN Rusetski. Magnetic fluids as drug carriers: targeted transport of drugs by a magnetic field. *Journal of Magnetism and Magnetic Materials*, 122(1):335–339, 1993.

[78] LG Saywell and BB Cunningham. Determination of iron: colorimetric o-phenanthroline method. *Industrial & Engineering Chemistry Analytical Edition*, 9(2):67–69, 1937.

[79] Kenneth E Scarberry, Erin B Dickerson, John F McDonald, and Z John Zhang. Magnetic nanoparticle- peptide conjugates for in vitro and in vivo targeting and extraction of cancer cells. *Journal of the American Chemical Society*, 130(31):10258–10262, 2008.

[80] F Scherer, M Anton, U Schillinger, J Henke, C Bergemann, A Kruger, B Gansbacher, and C Plank. Magnetofection: enhancing and targeting gene delivery by magnetic force in vitro and in vivo. *Gene therapy*, 9(2):102–109, 2002.

[81] Charles Seeney, Joshua O Ojwang, Ronald D Weiss, and Jim Klostergaard. Magnetically vectored platforms for the targeted delivery of therapeutics to tumors: history and current status. *Nanomedicine*, 7(2):289–299, 2012.

[82] Andrew Senyei, Kenneth Widder, and George Czerlinski. Magnetic guidance of drug-carrying microspheres. *Journal of Applied Physics*, 49(6):3578–3583, 1978.

[83] HC Seton, JMS Hutchison, and DM Bussell. Liquid helium cryostat for squid-based mri receivers. *Cryogenics*, 45(5):348–355, 2005.

[84] HC Seton, JMS Hutchison, and DM Bussell. Liquid helium cryostat for squid-based mri receivers. *Cryogenics*, 45(5):348–355, 2005.

[85] S Shtrikman and EP Wohlfarth. The theory of the vogel-fulcher law of spin glasses. *Physics Letters A*, 85(8):467–470, 1981.

[86] Bruce S Spinowitz, Annamaria T Kausz, Jovanna Baptista, Sylvia D Noble, Renuka Sothinathan, Marializa V Bernardo, Louis Brenner, and Brian JG Pereira. Ferumoxytol for treating iron deficiency anemia in ckd. *Journal of the American Society of Nephrology*, 19(8):1599–1605, 2008.

[87] Papell Solomon Stephen. Low viscosity magnetic fluid obtained by the colloidal suspension of magnetic particles, November 2 1965. US Patent 3,215,572.

[88] E Thellier. Sur les propriétés de l'aimantation thermorémanente des terres cuites. *CR Hebd. Seances Acad. Sci*, 213:1019–1022, 1941.

[89] Burghard Thiesen and Andreas Jordan. Clinical applications of magnetic nanoparticles for hyperthermia. *International Journal of Hyperthermia*, 24(6):467–474, 2008.

[90] Andreas F Thünemann, Simone Rolf, Patrick Knappe, and Steffen Weidner. In situ analysis of a bimodal size distribution of superparamagnetic nanoparticles. *Analytical chemistry*, 81(1):296–301, 2008.

[91] Jill van der Zee. Heating the patient: a promising approach? *Annals of oncology*, 13(8):1173–1184, 2002.

[92] Martijn Visscher, Joost J Pouw, Joop van Baarlen, Joost M Klaase, and Bennie ten Haken. Quantitative analysis of superparamagnetic contrast agent in sentinel lymph nodes using ex vivo vibrating sample magnetometry. *Biomedical Engineering, IEEE Transactions on*, 60(9):2594–2602, 2013.

[93] Peter Wick, Antoine Malek, Pius Manser, Danielle Meili, Xenia Maeder-Althaus, Liliane Diener, Pierre-Andre Diener, Andreas Zisch, Harald F Krug, and Ursula von Mandach. Barrier capacity of human placenta for nanosized materials. *Environmental health perspectives*, 118(3):432, 2010.

[94] Kenneth J Widder, Andrew E Senyei, and David F Ranney. Magnetically responsive microspheres and other carriers for the biophysical targeting of antitumor agents. *Advances in Pharmacology*, 16:213–271, 1979.

[95] Kenneth J Widder, Andrew E Senyei, and Dante G Scarpelli. Magnetic microspheres: a model system for site specific drug delivery in vivo. *Experimental Biology and Medicine*, 158(2):141–146, 1978.

[96] F Wiekhorst, C Seliger, R Jurgons, U Steinhoff, D Eberbeck, L Trahms, and C Alexiou. Quantification of magnetic nanoparticles by magnetorelaxometry and comparison to histology after magnetic drug targeting. *Journal of nanoscience and nanotechnology*, 6(9-10):3222–3225, 2006.

[97] Frank Wiekhorst, Uwe Steinhoff, Dietmar Eberbeck, and Lutz Trahms. Magnetorelaxometry assisting biomedical applications of magnetic nanoparticles. *Pharmaceutical research*, 29(5):1189–1202, 2012.

[98] Mark W Wilson, Robert K Kerlan Jr, Nicholas A Fidelman, Alan P Venook, Jeanne M LaBerge, Joy Koda, and Roy L Gordon. Hepatocellular carcinoma: Regional therapy with a magnetic targeted carrier bound to doxorubicin in a dual mr imaging/conventional angiography suite—initial experience with four patients 1. *Radiology*, 230(1):287–293, 2004.

[99] EP Wohlfarth. The temperature dependence of the magnetic susceptibility of spin glasses. *Physics Letters A*, 70(5):489–491, 1979.

[100] Jens Wuerfel, Eva Tysiak, Timour Prozorovski, Maureen Smyth, Susanne Mueller, Joerg Schnorr, Matthias Taupitz, and Frauke Zipp. Mouse model mimics multiple sclerosis in the clinico-radiological paradox. *European Journal of Neuroscience*, 26(1):190–198, 2007.

[101] P Wust, B Hildebrandt, G Sreenivasa, B Rau, J Gellermann, H Riess, R Felix, and PM Schlag. Hyperthermia in combined treatment of cancer. *The lancet oncology*, 3(8):487–497, 2002.

[102] Anat Yanai, Urs O Häfeli, Andrew L Metcalfe, Peter Soema, Lois Addo, Cheryl Y Gregory-Evans, Kelvin Po, Xianghong Shan, Orson L Moritz, and Kevin Gregory-Evans. Focused magnetic stem cell targeting to the retina using superparamagnetic iron oxide nanoparticles. *Cell transplantation*, 21(6):1137–1148, 2012.

[103] Benjamin B Yellen, Zachary G Forbes, Derek S Halverson, Gregory Fridman, Kenneth A Barbee, Michael Chorny, Robert Levy, and Gary Friedman. Targeted drug delivery to magnetic implants for therapeutic applications. *Journal of magnetism and magnetic materials*, 293(1):647–654, 2005.

[104] Jian You, Guodong Zhang, and Chun Li. Exceptionally high payload of doxorubicin in hollow gold nanospheres for near-infrared light-triggered drug release. *ACS nano*, 4(2):1033–1041, 2010.

[105] J Zhang and RDK Misra. Magnetic drug-targeting carrier encapsulated with thermosensitive smart polymer: core–shell nanoparticle carrier and drug release response. *Acta Biomaterialia*, 3(6):838–850, 2007.

[106] Jinlong Zhang, C Boyd, and Weili Luo. Two mechanisms and a scaling relation for dynamics in ferrofluids. *Physical review letters*, 77(2):390, 1996.